Integrated Study of Teff Grain Characteristics in Positive Pressure Dilute-Phase Pneumatic Conveyor: Experimental, CFD-DPM, and Artificial Neural Network Approaches

Lemi Demissie Boset

A Ph.D. Dissertation Submitted to

The Department of Mechanical Engineering,

College of Mechanical, Chemical, and Material Engineering

Presented in Partial Fulfillment of the Requirement for the Degree of Doctor of Philosophy in Agricultural Machinery Engineering

School of Postgraduate Studies

Adama Science and Technology University

February, 2026

Adama, Ethiopia

Integrated Study of Teff Grain Characteristics in Positive Pressure Dilute-Phase Pneumatic Conveyor: Experimental, CFD-DPM, and Artificial Neural Network Approaches

Lemi Demissie Boset

Supervisors:

Zewdu Abdi Debele (PhD) (Associate Professor)

Amana Wako Koroso (PhD) (Associate Professor)

A Ph.D. Dissertation Submitted to

The Department of Mechanical Engineering

College of Mechanical, Chemical, and Material Engineering

Presented in Partial Fulfillment of the Requirement for the Degree of Doctor of Philosophy in Agricultural Machinery Engineering

School of Postgraduate Studies

Adama Science and Technology University

February, 2026

Adama, Ethiopia

ORIGINALITY DECLARATION

This form must be completed and signed for all works submitted to the University for Examination.

Name of student	Lemi Demissie Boset
Id. No.	PGR/24818/14
Department	Mechanical Engineering
College	College of Mechanical, Chemical and Materials Engineering
Course Title	Agricultural Machinery Engineering
Title of work/Dissertation	Integrated study of teff grain characteristics in positive-pressure dilute-phase pneumatic conveyor: experimental, CFD-DPM, and artificial neural network approaches
Date of submission	

DECLARATION

1. I understand what plagiarism is and I am aware of the university's policy in this regard.
2. I declare that this "Integrated study of teff grain characteristics in positive-pressure dilute-phase pneumatic conveyor: experimental, CFD-DPM, and artificial neural network approaches" research project is my original work and has not been submitted elsewhere for examination or award of a degree or publication. Wherever others' work or my own work has been utilized, it has been duly acknowledged and referenced in compliance with the university's requirements.
3. I have not sought or used the services of any professional agencies to produce this work.
4. I have not permitted, nor will I permit, anyone to plagiarize my work with the intention of presenting it as their own.
5. I am aware that making any false claims regarding this work will lead to disciplinary action in accordance with the university's Anti-Plagiarism Guidelines.

Signature: ________

Date:________

RECOMMENDATION

We, the advisors of this dissertation, hereby certify that we have read the revised version of the dissertation entitled “Integrated study of teff grain characteristics in positive-pressure dilute-phase pneumatic conveyor: experimental, CFD-DPM, and artificial neural network approaches” prepared under our guidance by Lemi Demissie Boset submitted in Partial Fulfillment of the Requirement for the Degree of Doctor of Philosophy in Agricultural Machinery Engineering. Therefore, we recommend the submission of a revised version of the dissertation to the department following the applicable procedures.

Dr. -Ing. Zewdu Abdi		09/06/2025
Major Supervisor	Signature	Date
Dr. Amana Wako		10/06/2025
Co-supervisor	Signature	Date

APPROVAL SHEET

We hereby certify that the recommendations and suggestions made by the board of examiners are appropriately incorporated into the final version of the dissertation entitled "Integrated study of teff grain characteristics in positive-pressure dilute-phase pneumatic conveyor: experimental, CFD-DPM, and artificial neural network approaches" by Lemi Demissie Boset.

Dr. -Ing. Zewdu Abdi Debele		07/01/2026
Major Supervisor	Signature	Date
Dr. Amana Wako Koroso		08/01/2026
Co-supervisor	Signature	Date

We, the undersigned members of the Board of Examiners of the dissertation open defense by Lemi Demissie Boset, have read and evaluated the dissertation entitled "Integrated study of teff grain characteristics in positive-pressure dilute-phase pneumatic conveyor: experimental, CFD-DPM, and artificial neural network approaches" and examined the candidate during open defense. This is, therefore, to certify that the dissertation is accepted for partial fulfillment of the requirement of the degree of Doctor of Philosophy in Agricultural Machinery Engineering.

Dr. Demelash Gindo Lemi		
Chairperson	Signature	Date
Dr. Dawit Gudeta Gunjo		
Internal Examiner	Signature	Date
Prof. Solomon Workneh Fanta		15/01/2026
External Examiner 1	Signature	Date
Dr. Solomon Abera		13/01/2026
External Examiner 2	Signature	Date

Final approval and acceptance of the dissertation is contingent upon submission of its final copy to the School of Postgraduate Studies (SPGS) through the Department Graduate Council (DGC) and College Graduate Committee (CGC).

Department Head	Signature	Date
College Dean	Signature	Date
School of Postgraduate Studies, Dean	Signature	Date

ACKNOWLEDGEMENTS

First and foremost, I would like to express my deepest gratitude to the Almighty God for granting me strength, patience, determination, and the ability to accomplish this challenging work.

I am profoundly grateful to my main supervisor, Dr. -Ing. Zewdu Abdi, for his invaluable guidance and unwavering support throughout my research journey, from the initial proposal preparation to the detailed research activities. My sincere appreciation also goes to my co-supervisor, Dr. Amana Wako, for his insightful advice, continuous encouragement, and consistent guidance from the beginning to the completion of my research, as well as his valuable support in research paper writing. I also extend my heartfelt gratitude to my doctoral committee members, Dr. Fikadu Lamessa, Dr. Ramesh Babu, and Prof. Kishor Kolhe, for their constructive feedback and guidance, which significantly contributed to the improvement of my dissertation through progress reports.

I extend my heartfelt thanks to the Debre Zeit Agricultural Research Center (DZARC) of the Ethiopian Institute of Agricultural Research (EIAR) for providing teff as the test material and to Dilla University for sponsoring my PhD study. I also acknowledge Adama Science and Technology University (ASTU) for its support, particularly for the head of Department of Mechanical Engineering for providing a laboratory for computer and prototype construction, for the head of Department of Chemical Engineering facilitating laboratory tests, for the head of Department of Materials Engineering for providing a precise electronic balance, and for the head of Department of Applied Biology for granting access to the Scanning Electron Microscope (SEM) in microbiology laboratory and for all departments Laboratory Assistants who guide me and conduct laboratory tests.

I am especially grateful to the faculty and staff of the School of Mechanical, Chemical, and Materials Engineering at ASTU, with special appreciation to Dr. Addisu Bekele and Dr. Siraj Kedir for their valuable feedback during the proposal development and progress report stages. My sincere thanks also go to all academic and administrative staff of ASTU for their encouragement and facilitation of my PhD program.

Furthermore, I would like to extend my deep appreciation to my friend, Dr. Bethlehem Teferi, for assisting me in acquiring a crucial measuring instrument, which marked a significant turning point in my dissertation progress. I am also thankful to my fellow PhD students, Mr. Biniam Zewdie and Mr. Yonas Mulutu, for their constructive feedback and suggestions throughout my research.

Last but certainly not least, I owe my deepest gratitude to my beloved wife, W/ro Zewdinesh Alemu, and the whole of my family for their unwavering patience, understanding, and support. Their encouragement, enthusiasm, and emotional support have provided me with the strength and motivation to persevere in my research, making an immeasurable difference in my academic journey and life.

TABLE OF CONTENTS

LIST OF TABLES

LIST OF FIGURES

LIST OF ACRONYMS

AI	Artificial intelligence
ANN	Artificial neural network
ANOVA	Analysis of variance
ASAE	American Society of Agricultural and Biological Engineers
ASTM	American Society for Testing and Materials
CFD	Computational fluid dynamics
CS	Cyclone separator
DDPM	Dense discrete phase model
DEM	Discrete element method
DL	Deep learning
DNN	Deep neural network
DPM	Discrete phase model
DZARC	Debre Zeit Agricultural Research Center
EIAR	Ethiopian Institute of Agricultural Research
HP	Horizontal pipe
MAE	Mean absolute error
MAPE	Mean absolute percentage error
MC	Moisture content
ML	Machine learning
MMPIC	Multi-moment particle in cell
PC	Pneumatic conveyor
PD	Pressure drop
MSE	Mean squared error
PVC	Polyvinyl chloride
RMSE	Root mean square error
RNG	Re-normalize group
SEM	Scanning electron microscopy
SSR	Sum of squares for regression
SP	Straight pipe
TFM	Two-fluid model
TSS	Total sum of squares
VP	Vertical pipe

LIST OF NOTATIONS

A	Projected area of the particle (m^2)
B	Pipe bend (constant)
C_d	Drag coefficient (Unitless)
d_p	Mean particle diameter (m)
D	Pipe diameter (m)
D_a	Arithmetic mean diameter (m)
D_d	Diameter of dust outlet (m)
D_e	Diameter of gas exit (m)
D_g	Geometric mean diameter (m)
f	Air friction factor (Unitless)
F_D	Drag force (N)
F_{int}	Force of interaction (N)
F_L	Lift force (N)
g	Gravitational acceleration (m/s^2)
H	Height inlet of cyclone (m)
K	Pressure drop coefficient (Unitless)
K_b	Coefficient of pressure drop due to bends (Unitless)
K_c	Coefficient of pressure drop due to cyclone separator (Unitless)
K_f	Coefficient of pressure drop due to feeder (Unitless)
K_{st}	Coefficient of pressure drop due to straight pipe (Unitless)
L	Pipe length (m)
L_b	Length of the body (m)
L_c	Length of the cone (m)
m	Mass (kg)
m_a	Air mass flow rate (kg/s)
M_g	Mass of particle (kg)
m_s	Solid mass flow rate (kg/s)
P	Power required (Watts)
P_{input}	Input power (Watts)
Q	Air flow rate (m^3/s)
r	Radius (m)
R_b	Bend radius (m)
Re	Reynolds number (Unitless)
S	Length of the vortex finder of cyclone (m)
SD	Standard deviation (Units as the original data)
T	Thickness (m)

t	Time (s)
v	Air velocity (m/s)
ν	Kinematic viscosity (m^2/s)
V_a	Volume of air (m^3)
v_{entry}	Inlet air velocity (m/s)
V_s	Volume of solid (m^3)
V_{sm}	Average superficial velocity (m/s)
V_{salt}	Saltation velocity (m/s)
V_t	Terminal velocity (m/s)
W	Inlet width of cyclone (m)
y^+	Wall function (Unitless)
∇	Gradient operator (Unitless)
L	Length (m)
ΔL	Change of length (m)
ΔP	Pressure drop (Pa)
ΔP_{accel}	Pressure drop due to particle acceleration (Pa)
ΔP_{air}	Pressure drop due to air (Pa)
Δp_{bends}	Pressure drop due to bends (Pa)
$\Delta p_{cyclone}$	Pressure drop due to cyclone separator (Pa)
Δp_{feeder}	Pressure drop due to the feeder (Pa)
Δp_{hor}	Pressure drop due to horizontal pipes (Pa)
ΔP_{lift}	Pressure drop due to lift (Pa)
ΔP_{solids}	Pressure drop due to solid (Pa)
ΔP_{st}	Pressure drop due to straight pipes (Pa)
ΔP_{total}	Total pressure drop (Pa)
Δp_{ver}	Pressure drop due to vertical pipes (Pa)
ρ	Density (kg/m^3)
ρ_a	Density of air (kg/m^3)
ρ_b	Powder bulk density (kg/m^3)
ρ_g	Density of gas (kg/m^3)
ρ_s	Density of solid (kg/m^3)
ρ_{sus}	Suspension density (kg/m^3)
ε	Voidage (Unitless)
ϕ	Sphericity (Unitless)
μ	Solid loading ratio (Unitless)
μ_d	Dynamic viscosity of air (kg/m.s)
Θ	Hopper half-angle (^{o})
η	Efficiency (Unitless)

∂	Partial (Unitless)
∂u	Velocity components in x direction (m/s)
∂v	Velocity components in y direction (m/s)
∂w	Velocity components in z direction (m/s)
ξ_a	Pressure drop coefficient due to air (Unitless)
ξ_c	Pressure drop coefficient for cyclone (Unitless)
ξ_s	Pressure drop coefficient due to solid (Unitless)

ABSTRACT

Teff is a gluten-free grain native to Ethiopia that is gaining global popularity due to its nutritional benefits. Despite its advantages, teff faces challenges in farming and handling because of its tiny grain size, weak stems, high lodging tendency, and reliance on traditional production and postharvest methods. These factors contribute to low yields, poor grain quality, and substantial losses during harvesting, handling, and processing. This study investigates the use of pneumatic conveying systems to improve teff grain handling, with a focus on pressure drop as a key system parameter. The research involved determining engineering properties, designing and constructing a laboratory-scale conveyor system, and analyzing pressure drops across critical components, including the feeder, horizontal and vertical pipes, 90° bends, and a cyclone separator. Laboratory experiments, CFD-DPM simulations, and artificial neural network modeling were employed to comprehensively study the system. Teff grain was found to have a mean particle diameter of 0.68-0.72 mm, particle density of 1120-1381 kg/m³, sphericity of 0.67-0.69, terminal velocity around 3.6 m/s, and an angle of repose between 20.2° and 23.8°. Compared to other cereal grains, teff's smaller particle size and lower terminal velocity significantly influence its pneumatic conveying characteristics. Fluidized bed tests revealed that teff behaves as a bubbly, free-flowing material, with pressure drops of 100-107 mbar/m and a minimum fluidization velocity of 0.56-0.575 m/s, indicating that dilute-phase pneumatic conveying is more suitable than dense-phase systems. Minimum conveying velocities ranged from 6.0-20.7 m/s, depending on solid loading ratios 0.3-5.0 and pipe diameters 50-110 mm, suggesting that teff requires relatively lower airflow rates for full particle suspension. However, it's very small particle size leads to higher pressure drops and non-uniform air velocity distribution in straight pipes. CFD-DPM simulations closely matched laboratory results, with R^2 values of 0.990-0.997. ANN models trained on both experimental and simulation data also performed excellently, predicting pressure drops with R^2 values of 0.971-0.981. Statistical validation demonstrated the reliability of these models, with MSE of 27-7984, RMSE of 5.2-89, MAE of 4.1-65, and MAPE of 6-25%, showing strong agreement with experimental results and reliable predictive capability. The findings emphasize that the design of pneumatic conveyors for teff must consider its small particle size, moderate density, and low terminal velocity, rendering dilute-phase conveying the most suitable option. It is essential to optimize airflow and pressure differentials to ensure a blockage-free and energy-efficient operation. In summary, the integration of experimental analysis, CFD-DPM simulations, and ANN modeling offers a comprehensive approach to understanding teff grain flow, thereby facilitating the design, development, and optimization of efficient pneumatic conveying systems for production, postharvest handling, and processing applications.

Keywords: Artificial neural network, Computational fluid dynamics, Experimental, Pneumatic conveying, Pressure drop, Teff grain

CHAPTER ONE

INTRODUCTION

1.1. Background of the study

Teff (Eragrostis tef (Zucc.) Trotter) is an essential cereal crop native to Ethiopia and is deeply a part of the nation's culture and traditions. The crop not only serves as a crop used in agriculture, a staple crop, but is also a country's symbol of pride. It is a really important crop for small farmers in Ethiopia, a staple food, and it has been a main source of food for thousands of years (Barretto et al., 2021).

Teff is the smallest grain in the world, having colors from ivory and reddish-brown to white, with a distinct taste. It is gluten-free and nutritionally rich, containing high levels of protein, fiber, iron, calcium, and essential amino acids, and it has gained global credit as a potential super food and a viable alternative in modern food products (Abebaw & Abera, 2020; Alfy et al., 2012; Tadele & Hibistu, 2022).

Teff is an annual warm-season grass that occurs in different agro-ecological conditions. It was cultivated optimally at high altitudes from 1,500 to 2,500 meters above sea level with rainfall from 450 to 550 mm annually and needs drained soils with a pH from 5.5 to 6.5. However, teff is highly robust, tolerating nutrient-poor soils, drought, and waterlogging. Its maturation period ranges from sixty to one hundred twenty days, depending on the variety and environmental situation. It is primarily rain-fed and can also be irrigated; this highlights its adaptability in various conditions (Adepoju et al., 2024; Alemu et al., 2024; Gadissa & Adem, 2025).

Teff is the basis of Ethiopia’s food security, feeding huge parts of the population. It is grown by over 6.5 million smallholder farmers and produces over 5.4 million metric tons annually. Ethiopia also produces 90% of the world’s teff, while its cultivation is expanding to Eritrea, Netherlands, South Africa, Kenya, U.S., Australia, and other regions due to its adaptability (Hein et al., 2025). It has the lowest yield of all the main cereal grains in Ethiopia, usually ranging from 17.56 to 18.82 quintals per hectare (Tiguh et al., 2024). To achieve higher teff yields, adopting row planting for optimal spacing, adjusting seeding rates, selecting improved varieties, and applying appropriate fertilizers are essential agronomic practices (Negash et al., 2017).

Teff takes a bigger portion of farmland in Ethiopia than other major grains like maize, wheat, sorghum, and barley. In the 2020/21 production year, it covered about 22.56% of all of Ethiopia's agricultural land (Tiguh et al., 2024).

In Ethiopian teff grain production varies in different regions of the country, including Oromia, Amhara, Tigray, Southern Nation and Nationalities Region, Benishangul-Gumuz, and others. As Oromia is high in terms of production, followed by Amhara and Tigray, productivity rates vary as agricultural practices are different, climatically variable, and resource-constrained. The regional distribution of teff highlights its importance in Ethiopian agriculture (Tadele & Hibistu, 2022).

In Ethiopia, teff provides 2/3 of the daily protein intake. It is the primary ingredient for injera, a sourdough flatbread, porridge, and alcoholic beverages t'ella, and arak'e. It has high mineral content and is suitable for fortified baby foods (Zeleke, 2015). Beyond human consumption, teff grass serves as nutritious fodder for livestock and is used in construction for the plastering of storage walls (Roseberg et al., 2018).

Recently, advancements in teff production have improved its yield and quality, with notable progress through cluster farming practices that enable smallholder farmers to pool resources, share knowledge, and achieve economies of scale. The introduction of mechanized solutions has reduced losses and labor intensity, while the adoption of improved agronomic practices, including optimized planting techniques, high-yield seed varieties, and precision fertilizer use, has further increased yields and grain quality (Endalew et al., 2024).

Research, infrastructure development, and farmer training must continue to stimulate productivity growth and development. The policies on production and price stabilization are required to meet the country's domestic needs and growing export demand; these measures must be carefully designed to avoid negatively affecting Ethiopian farmers' livelihoods. Effective policy implementation should balance market competitiveness with fair producer prices, ensuring that farmers remain motivated to sustain and improve teff production. In addition, work on high-tech agricultural innovations and sustainable practices for productivity improvement, market access, and quality enhancement to become competitive in exports is urgently required (Yigezu, 2021).

Pneumatic conveyors were a good alternative to handle dry fine bulk material like teff grain, using airflow in the pipeline to produce a gentle and efficient way of transporting bulk material. They were commonly used in a wide range of industries, such as agriculture, food processing, chemicals, pharmaceuticals, and others. When it came to handling agricultural products, pneumatic conveyors greatly minimized contamination and reduced labor for transporting. Their versatility was combined with economically efficient methods to transport bulk material (Chan et al., 2015; Mohapatra et al., 2019).

Pneumatic conveying systems were categorized into three main types based on their operating principles and phase density. Dilute-phase conveying operated with high velocity and low pressure, maintaining a low product-to-air ratio that kept materials suspended during continuous transport. In contrast, dense-phase systems functioned in batches using low velocity and high pressure with a high product-to-air ratio, making them suitable for fragile materials. Mixed-phase conveying served as an intermediate system that combined characteristics of both dilute and dense phases (Shijo & Behera, 2023).

Pneumatic conveying systems benefited in terms of flexibility to change or adapt to new materials and new processes, providing tremendous advantages, along with self-cleaning designs that minimized material losses. The enclosed nature of pneumatic conveyors enhanced safety by reducing operator risk and preventing environmental contamination. Additional benefits included low maintenance requirements due to few moving parts, weatherproof construction, and the ability to transport materials over long distances without degradation (Ghafori & Sharifi, 2018).

Beyond material transport, pneumatic conveyors effectively managed dust extraction while helping to regulate moisture and temperature levels during conveyance. The practical applications of pneumatic conveying technology extended across a wide range of agricultural and industrial processes, including seeding, harvesting, cleaning, drying, loading, unloading, feeding, blending, and packing (Deka & Bortha, 2024).

Mechanical conveyors were often inefficient for modern processing of fine dry bulk materials because they had rigid designs, occupied large spaces, and exposed materials to dust and contamination risks. These systems could also damage fragile products, particularly fine grains and powders, during handling and transfer. They required extra components for changes in direction or elevation, which increased complexity and maintenance demand. Frequent maintenance and limited flexibility further reduced their practical application in modern processing facilities. In addition, mechanical systems could generate dust emissions, causing material loss, environmental concerns, and inconsistent flow behavior. Therefore, selecting a conveyor system required consideration of the material characteristics, processing requirements, and available space to ensure efficient and reliable operation (Kay, 2012; Govindan, 2020; Tadic et al., 2024).

1.2. Justification

Teff has recently gained significant attention in the contemporary food industry due to its remarkable nutritional and health benefits, as well as its increasing global demand. Despite its high nutritional value, teff faces major agronomic and postharvest challenges arising from the crop's unique characteristics. Its small grain size, weak stems, high lodging tendency, and reliance on traditional production, handling, and processing methods all contribute to low productivity, high post-harvest losses, and suboptimal grain quality.

In Ethiopia, teff productivity is limited with average yields reported at 17.56-18.82 quintals ha^{-1} (Tiguh et al., 2024), far below the potential 3.5-4.0 t ha^{-1} achievable under improved cultivation practices (Negash et al., 2017). Post-harvest losses were also substantial, ranging from 16-30% during harvesting and handling (Minten et al., 2016), with an additional 2.2-3.3% lost along rural-urban supply chains (Gonite, 2018). These challenges collectively reduce efficiency in production and supply, limiting the economic and nutritional benefits of the grain.

Teff occupies 22.56% of Ethiopia's cultivated land (Tiguh et al., 2024) and supports over 6.5 million smallholder farmers (Hein et al., 2025). Improving post-harvest and handling technologies has significant potential to enhance food security, farmer livelihoods, and export competitiveness. Therefore, research and development of innovative production, handling, and processing technologies were critical to increasing yield, reducing losses, maintaining grain quality, and improving overall processing efficiency.

Currently, Ethiopia primarily produces teff for local consumption. Nevertheless, the country has a large capacity to scale into international demands. This can be achieved by increasing production, adopting advanced handling technologies, and developing industrial processing methods to create a variety of value-added products that meet global standards.

Such advancements would generate significant national income and unlock the potential of this valuable grain.

As one of the modern handling solutions, pneumatic conveying stands out by combining precision, efficiency, and sustainability. It offers effective approaches for the agriculture and food processing industries. Particularly for delicate or high-value bulk materials like teff grain, these systems streamline operations, reduce material losses, and maintain product quality, proving a vital role across a wide range of applications.

1.3. Statement of the problem

Teff is a gluten-free grain with highly regarded nutritional benefits and has recently attracted the attention of the modern food business (Zeleke, 2015). However, adequate information is still hindering its handling and processing activities because it is a relatively new raw material for modern industry (Sternberg & Sternberg, 2016). It is tiny and also called the smallest grain in the world, which makes it challenging to handle without loss (Barretto et al., 2021; Tadele & Hibistu, 2021; Tiguh et al., 2024).

Teff has unique physical properties that make it hard to handle mechanically. This limits the adoption of modern agricultural technologies and contributes to low yields and inconsistent grain quality. Farmers continue broadcasting teff seed by hand at 25-50 kg/ha, although research recommends only 3-5 kg/ha to improve efficiency and reduce waste (Dagnachew et al., 2020). During harvest and post-harvest operations, teff can lose 16-30% due to shattering, contamination, and lodging, which alone can cause losses of up to 30% (Minten et al., 2016). Post-harvest losses along rural-urban chains reach 2.2-3.3%, largely tied to storage and transportation challenges (Gonite, 2018).

Researchers have suggested using aerodynamic properties, especially terminal velocity, for teff cleaning, drying, and pneumatic transport (Shahbazi et al., 2014; Awgichew, 2019; Bako & Bardey, 2020). However, terminal velocity focuses on individual particles and does not represent actual pneumatic conveying conditions where particle concentration, pipe diameter, and solid loading ratio influence flow behavior, while minimum conveying velocity provides a more realistic design basis for pneumatic conveying of granular materials.

Handling agricultural bulk materials is challenging due to their natural variability, and studies employing numerical and machine-learning approaches remain limited

(Abdollahpour et al., 2020; Emam et al., 2021; H. Zhao et al., 2021; Li et al., 2024). Teff, in particular, has received very little engineering-focused research. Machines adapted from wheat, rice, or other cereals often perform poorly with teff because of its exceptionally small grain size and low terminal velocity. Most prior pneumatic conveying studies focus on cereals such as wheat, maize, rice, or others, leaving teff-specific handling largely unexplored.

A major problem in cereal grain pneumatic conveying research was the lack of integrated experimental, numerical, and machine learning approaches. Previous studies primarily relied on physical experiments and did not combine experimental, numerical, and AI-based modeling, which limited the accuracy of system design and optimization.

Therefore, the study applied an integrated approach combining experimental tests, numerical simulations, and AI-based modeling, which had not previously been used for teff grain. This approach generated new engineering property data, simulated teff-specific pneumatic flow behavior, and developed predictive machine-learning models. It provided both original scientific insights and practical guidance for designing efficient pneumatic conveying systems, ultimately supporting improved teff grain handling, reduced post-harvest losses, and enhanced processing.

1.4. Objectives

1.4.1. General objective

This study aims to model the characteristics of teff grains in a positive-pressure dilute-phase pneumatic conveying system using experimental analysis, CFD-DPM simulations, and ANN modeling.

1.4.2. Specific objectives

1. To determine the relevant engineering properties, design, and construct a positive-pressure dilute-phase pneumatic conveyor for teff grain;

2. To experimentally investigate and perform CFD-DPM simulation analysis of pressure drops in the feeder, horizontal pipes, vertical pipes, 90° bends, and cyclone separator of the positive-pressure dilute-phase pneumatic teff grain conveyor using piecewise and full system approaches; and

3. To predict pressure drops in the feeder, horizontal pipes, vertical pipes, 90° bends, and cyclone separator of the positive-pressure dilute-phase pneumatic teff grain conveyor using artificial neural network modeling approach.

1.5. Significance of the study

This research addressed critical gaps in the literature, knowledge, and methodology related to pneumatic conveying of teff grain by using an integrated approach that combined experimental investigation, cost-effective CFD-DPM simulations, and ANN modeling, which captured nonlinear relationships between system variables more effectively than traditional models for predicting the flow behavior of teff grain in pneumatic conveying systems.

No prior research specifically addressed the pneumatic conveying characteristics of teff grain. This study aimed to characterize these conveying behaviors, filling a critical gap in the literature. Previous research had predominantly focused on other cereal grains, such as wheat, maize, barley, and sorghum, leaving teff-specific pneumatic conveying behavior largely unexplored.

Previous studies often recommended using terminal velocity for teff handling, which could lead to a misunderstanding of pneumatic conveying principles. Terminal velocity applies only to single particles and does not account for particle concentration, bulk flow, or pipe geometry. In contrast, the minimum conveying velocity provides a more accurate representation of pneumatic conveying behavior by considering particle concentration, airflow rate, and pipe diameter. This study addressed this gap by determining the minimum conveying velocity of teff grain in a pneumatic conveyor.

Existing empirical and theoretical models were also limited by small datasets, high costs, and difficulty in representing the complex properties of agricultural particulate materials. A thorough review of current modeling efforts revealed a lack of studies integrating experimental data, numerical simulations, and machine-learning techniques. This research addressed that gap by developing an integrated experimental, CFD-DPM, and ANN approach capable of accurately predicting teff grain behavior in dilute-phase pneumatic conveying systems.

Beyond its scientific contributions, the findings offered practical benefits for engineers, researchers, and the food and grain processing industries. The results guided the optimization of pneumatic teff grain conveyors for diverse applications, including conveying, seed drilling, cleaning, drying, cooling, disinfestation, feeding, blending, and packing. The improved understanding of pressure drop, air velocity requirements, and grain-air interactions supported the design of more energy-efficient systems, reduced grain damage, and contributed to the development of future pneumatic handling technologies.

1.6. Scope of the study

This study investigated how teff grain flowed in a positive-pressure dilute-phase pneumatic conveyor. Laboratory tests, numerical simulations, and machine learning (ANN) modeling techniques were employed. First, a lab-scale pneumatic conveyor was constructed specifically for teff grain, with attention given to key components such as the feeder, horizontal and vertical pipes, 90° bends, and a cyclone separator. Each component was individually tested and analyzed to understand its behavior, and the results were then integrated to evaluate the performance of the complete system. This approach allowed for the assessment of airflow, pressure drop, particle transport, and overall system efficiency under realistic operating conditions.

The experiments were designed to measure inlet air velocity, material flow rate, and pressure drops across the system under various operating conditions. These measurements provided critical data for evaluating system performance and understanding the effects of airflow rate, material flow rate, pipe geometry, and system configuration. Moreover, the experimental results served as a benchmark for validating the CFD-DPM simulations and the ANN model, ensuring that both accurately reflected the behavior of the grain in pneumatic conveying.

CFD-DPM simulation was used to enhance the understanding of system behavior and to generate additional data for the ANN model. It provided a detailed analysis of pressure and air velocity distribution, particle concentration, and particle residence time without being limited by operating conditions. This made it a valuable tool for strengthening system insights and improving the prediction accuracy of the ANN model.

Combined data from experimental tests and CFD-DPM simulations were used to develop an ANN model for predicting pressure drops across the main components of the pneumatic conveying system, including the feeder, horizontal and vertical pipes, 90° bends, and cyclone separator, while the total system pressure drop was expressed as the sum of pressure drops across all major components. This integrated approach enabled the study to accurately capture the complex flow behavior of teff grain and improve prediction accuracy.

1.7. Limitations of the study

The study focused on positive-pressure dilute-phase pneumatic conveying systems, which were theoretically suitable for teff grain. Dense-phase pneumatic conveying, which uses higher material concentrations at lower air velocities, resulting in greater pressure drops and higher energy demands, was excluded. Dense-phase systems were typically preferred for fragile materials and were also expensive to study numerically due to their complexity and high computational requirements. Negative-pressure systems, often used for transporting dusty or hazardous materials, were also not included; these systems were subjected to high pressure drops, convey over short distances, and present more challenging material feed rate control.

This study did not examine the mechanical damage to teff grains caused by collisions with pipe walls during pneumatic conveying, which uses fast air to transport the grains. Previous research indicates that the mechanical damage rate for cereal grains is typically below 5%. The extent of mechanical damage depends on particle size, density, and impact energy. Because teff grains were smaller and lighter than other cereal grains, they experience less impact energy, which may result in lower damage. However, this assumption requires further experimental validation.

Pneumatic conveyors were not used solely for transporting dry, fine bulk materials but also for dust extraction and the integration of heaters and coolers, which were essential for moisture- and temperature-sensitive processes. Therefore, future research should focus on negative-pressure and dense-phase pneumatic conveyors, the effects of mechanical damage, dust extraction, and the incorporation of heaters and coolers. Addressing these areas would significantly enhance the versatility of pneumatic teff grain conveyors and improve their performance across a wider range of handling and processing operations.

1.8. Organization of the dissertation

This dissertation consisted of five chapters, each addressing specific aspects of the study. Chapter One presented the introduction, justification, problem statement, objectives, significance, scope, and limitations of the study. Chapter Two reviewed recent research on the pneumatic conveying characteristics of materials, technological advancements in the field, and identified research gaps. Chapter Three described the materials, experimental setup, and methods used for investigation, analysis, and model evaluation. Chapter Four discussed the data obtained from laboratory experiments, CFD-DPM simulations, and ANN model results. Finally, Chapter Five presented the main conclusions, practical recommendations for agricultural and industrial applications, and suggestions for future research.

CHAPTER TWO

LITERATURE REVIEW

2.1. Material properties relevant to pneumatic conveying

Pneumatic conveying behavior depends strongly on particle characteristics such as moisture content, bulk and true density, particle size and shape, porosity, friction, terminal velocity, and angle of repose. These properties determine air-particle interaction, minimum conveying velocity, flow stability, separation efficiency, and energy demand (Sabar et al. 2020).

Teff is distinct among cereal grains due to its fine size, which increases dustiness, segregation, and handling losses. Typical values reported for teff include moisture content 8-15%, thousand-grain weight 0.2-0.4 g, bulk density 806-840 kg/m³, true density 1090-1401 kg/m³, mean diameter 0.5-1.1 mm, sphericity 0.67-0.69, terminal velocity 3.08-3.96 m/s, and angle of repose 22-23° (Zewdu & Solomon, 2007b; Abebaw & Abera, 2020). These require careful design of a handling system to reduce losses, dust, and degradation.

Compared with teff, grains such as wheat, maize, sorghum, and barley generally exhibit larger particle diameters (2.5-8 mm), greater thousand-grain weights, wider moisture ranges, and higher terminal velocities (5-13 m/s), resulting in different conveying behavior and energy needs (Molenda & Stasiak, 2001; Guner, 2007; Tavakoli et al., 2009; Ghafori et al., 2011; Aremu et al., 2014; Markauskas et al., 2015; Gu, 2018; Tabir et al., 2019; Vasundhara et al., 2019; Sabar et al., 2020). Therefore, correlations and operating guidelines developed for larger grains were not directly applicable to teff grain.

Terminal velocity is a key aerodynamic parameter in pneumatic separation and conveying, as it defines the minimum airflow required to suspend particles and maintain efficient transport (Vasundhara et al., 2019; Semenov et al., 2022). It depends on particle characteristics such as size, shape, density, and moisture content, as well as air properties like density and viscosity. Terminal velocity reflects the airflow resistance experienced by particles under actual flow conditions and is calculated according to the method described by Zewdu (2007a). Measuring or calculating this parameter is crucial for designing blower specifications and determining the minimum conveying velocity in dilute-phase pneumatic systems. The terminal velocity of the particle was measured using Equations 2.1 to 2.3, as described by Zewdu (2007a).

$$M_g = \frac{1}{2} Cd \rho a A V_t^2 \tag{2.1}$$

$$V_t = \left(\frac{2M_g}{Cd \rho a A} \right)^{\frac{1}{2}} \tag{2.2}$$

$$Cd = \left(\frac{2M_g}{V_t^2 \rho a A} \right) \tag{2.3}$$

Terminal-velocity models describe the behavior of individual particles, whereas pneumatic conveying involves the movement of bulk material, where the interactions of a group of particles with the airflow become important. For this reason, parameters such as saltation velocity and solid loading were critical design considerations, which account for the combined effects of material flow rate, air flow rate, and pipe diameter on conveying performance (Khoshtaghaza & Mehdizadeh, 2006; Sabar et al., 2020). Incorporating these parameters ensures that the system is designed to prevent particle settling, reduce pipeline blockages, and optimize energy efficiency in the transport of bulk materials.

Overall, precise measurement and interpretation of cereal grain physical and aerodynamic properties were crucial for pneumatic conveying system design parameters such as terminal velocity and saltation velocity, which guided the design of PC for cereal grains (Shahbazi et al., 2014; Awgichew, 2019; Bako & Bardey, 2020).

The numerical study used Rocky DEM to track each particle's motion using Newton's second law, accounting for forces such as gravity, contact interactions, and fluid drag, and updating particle positions and velocities over time to simulate realistic trajectories and behavior. In this context, terminal velocity is determined as the steady-state velocity that a particle reaches while falling through the fluid domain, typically observed during post-processing or through trajectory analysis. This approach allows the simulation of particle-air interactions and the assessment of aerodynamic properties critical for pneumatic conveying design. Where $\vec{v}$ = Instantaneous velocity of the particle calculated as Equation 2.4, $\vec{F}_g$ = gravitational force, $\vec{F}_d$ = drag force from the fluid, and $\vec{F}_c$ = contact forces from collisions (Emam et al., 2021).

$$m\frac{d\vec{v}}{dt} = \vec{F}_g + \vec{F}_d + \vec{F}_c \tag{2.4}$$

In a CFD-DEM setup, terminal velocity is determined when the net vertical acceleration becomes zero: If only gravity and drag were considered:

$$\vec{F}_g + \vec{F}_d + \vec{F}_c = 0 \tag{2.5}$$

2.2. Theoretical background of designing pneumatic conveying systems

Pneumatic conveying is a method of transporting bulk materials such as grains, powders, and granules used in various industries, particularly in agriculture and food products. In pneumatic conveying, materials were moved through pipes using air or other gases. The design of pneumatic conveying systems requires an understanding of fluid dynamics, particle mechanics, and material properties. In practical application, there were two modes of conveying dilute-phase suspension flow and dense-phase non-suspension flow, which have their advantages and disadvantages (Behery et al., 2017; Wheeldon et al., 2022). A typical low-pressure pneumatic conveyor system is illustrated in Figure 2.1.

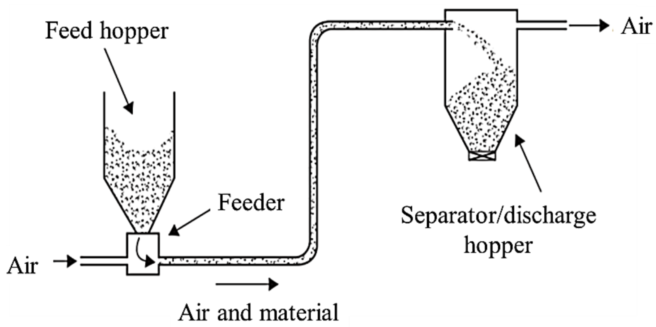

Figure 2.1. Typical low-pressure pneumatic conveyor (Bodkhe et al., 2015)

Airflow should be optimized and selected to reduce the pressure drop in pneumatic conveying systems. Pressure drop depends on pipeline size and layout, conveying velocity, material flow rate, and particle-wall friction. Empirical models and Computational fluid dynamics can be used to predict the pressure drop in pneumatic conveying systems. Conveying velocity should be taken into account; low air velocity may cause blockages by settling particles, and high air velocity leads to high energy consumption and more pipeline wear or material damage. Attention should be paid to selecting appropriate blowers, pipelines, and cyclone separators according to the material characteristics and system pressure drop (Kuang et al., 2020).

2.2.1. Flow regimes in pneumatic conveyor

The gas-solid multiphase flow model is important in understanding the behavior of materials in pneumatic conveying systems. In Figure 2.2, it can be seen that there were six flow regimes (a-f). As the gas velocity increases, the flow regime changes from slug to dispersed flow. The arrangement and movement of particles can cause a pressure drop, which can be understood to have an efficient pneumatic conveying system for material handling (Suppan et al., 2021).

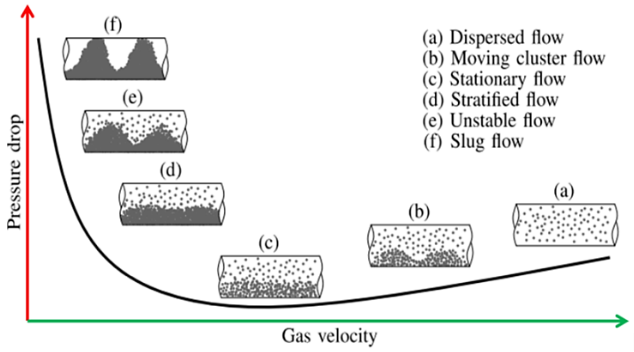

Figure 2.2. Flow regimes in pneumatic conveying (Suppan et al., 2021)

2.2.2. Some guidelines for designing pneumatic conveyors

Positive-pressure pneumatic conveyors were used when long-distance conveying is required; the material to be handled is diverse, including dense, heavy, and abrasive materials, and when distribution to multiple outlets from one source is needed. It is present in lower-pressure drops; therefore, it is more energy efficient, cheaper to operate, and requires less maintenance (Abe et al., 2023).

On the other hand, negative pressure or vacuum pneumatic conveyors were suitable for short-distance conveying, handling dusty and fragile material, or when collecting material from multiple sources to one terminal. It is frequently used in applications where dust control and gentle handling were needed, such as in food and pharmaceutical products, but it suffers from higher pressure drops, higher maintenance, and is less energy efficient at long distances. The choice of phase of conveying depends on the material properties, conveying distance, and the system needed (Ozlu & Guner, 2022).

A pneumatic conveyor could be divided into three main sections: the feeding section that includes the feeder through which the material enters the system; the pipeline section that includes horizontal, vertical, and bend parts; and the separation section that includes the cyclone separator through which the material is separated from the airflow (Abe et al., 2023).

In pneumatic conveyors, measuring pressure drop at least 2-3 meters of pipeline length should be there to get a considerable pressure drop under minimum conditions (Shijo &

Behera, 2021a). In pneumatic systems, there were 90° bends; the bend radius to pipe bore diameter ratio should be at least 6 (Shijo & Behera, 2021). The solid loading ratio for dilute-phase pneumatic conveying ranges between 1 and 15, in practice usually between 2 and 5 (Yang et al., 2024). Inlet air velocity for PC varies between 10 m/s to 30 m/s for the dilute phase and 3 m/s to 8 m/s for the dense phase (Barrozo et al., 2010).

In dilute-phase pneumatic conveyors, saltation velocity is an important parameter to be considered for the successful operation of the system. Prediction of saltation velocity is very important for the design and operation of dilute-phase pneumatic conveying systems. The systems should be operated at the desired flow rate without particle deposition (Gomes & Mesquita, 2014).

2.2.3. Gas fluidization characteristics

Dense-phase conveying operates at low velocity and high pressure, suitable for cohesive powders Geldart A, minimizing abrasion. Dilute-phase systems were ideal for free-flowing particles Geldart B/D, but consume more energy. Key parameters include minimum fluidization velocity $U_{mf,}$ and pressure drop through the bed (Kaur et al., 2017). The minimum fluidization velocity and maximum bed pressure drop were evaluated using laboratory tests and the Carman-Kozeny equation as follows:

$$\frac{\Delta P}{L}\cdot\frac{D_p}{\rho(V_{sm})^2}\cdot\frac{\varepsilon^2}{1-\varepsilon}=150\frac{1-\varepsilon}{R\varepsilon}+1.75 \tag{2.6}$$

Minimum fluidized velocity is calculated for a particle mean diameter of 0.70 mm, an original bed height of 0.3 m, and a bed diameter of 0.05 m.

$$V_{sm}=\frac{Q\times10^{-3}}{A} \tag{2.7}$$

CFD simulations using ANSYS Fluent with the Euler-Euler model and Syamlal-O'Brien drag model have captured fluidized bed behavior accurately, showing bed expansion at high gas velocities and fluctuating pressure drops at low velocities (Ajouri et al., 2022). Moisture content influences airflow resistance; denser fill increases pressure drop. The Ergun equation predicts trends within 7-8% error, guiding system optimization (Zewdu & Siraj, 2021).

2.2.4. Solid loading ratio

The solids loading ratio (μ) or phase density is a useful parameter to help observe the flow rate. It is the ratio of the mass flow rate (m_s) of the material being conveyed, divided by the mass flow rate (m_a) of the air being used to convey the material. The recommended maximum solids loading ratio for dilute-phase pneumatic conveyors is 1 to 15 percent (Ebrahimi et al., 2014). It is calculated as Equation 2.8:

$$\mu = \frac{m_s}{m_a} \tag{2.8}$$

2.2.5. Rotary feeder

The design of the rotary feeder focuses on selecting an appropriate rotation speed to ensure an accurate and consistent material flow rate. This helps minimize air leakage and reduce energy consumption, improving both the reliability and efficiency of the pneumatic conveying system (Gomes et al., 2021). The material flow rate from the hopper to the pneumatic conveyor through the rotary feeder can be calculated using the methods and equations provided, as shown in Equation 2.9. The pressure drop caused by the rotary feeder is calculated using Equation 2.10 and *B* is outlet diameter of the hopper.

$$m_s = \frac{B^2 \rho_b \sin(\theta)}{2[1 - g\sin(\theta)]} \tag{2.9}$$

$$\Delta P = k\frac{\rho v^2}{2} \tag{2.10}$$

2.2.6. Minimum conveying velocity

Minimum conveying or saltation velocity is the speed at which particles remain suspended. This prevents deposition and blockages, ensuring continuous operation. Equation 2.11 is Rizk's equation used to estimate minimum conveying velocity (Rakhimov et al., 2023).

$$\mu = \left(\frac{1}{10^{1440 d_p + 1.96}}\right)\left(\frac{V_{salt}}{\sqrt{gD}}\right)^{1100 d_p + 2.5} \tag{2.11}$$

2.2.7. Pressure drop in pneumatic conveying system

In a pneumatic conveying system, the total pressure drop, expressed in Equation 2.12, is the sum of losses from particle acceleration, lifting solids vertically, bends and elbows, air friction along the pipe, and friction between particles and pipe walls (Datta & Ratnayaka, 2003), and is expressed as follows:

$$\Delta P_{total} = \Delta P_{accel} + \Delta P_{lift} + \Delta P_{bends} + \Delta P_{air} + \Delta P_{solids} \tag{2.12}$$

Superficial gas velocity is typically $1.5V_{salt}$, and the air friction factor (f) is calculated from Reynolds number (Re) is:

$$\mathrm{Re} = \frac{\rho_a v D}{\mu_d} \tag{2.13}$$

Bend and solid friction factors were applied using empirical correlations (Sharma & Mallick, 2019). Froude numbers and particle terminal velocities were used for multiphase flow characterization, ensuring accurate pressure drop predictions.

2.2.8. Pressure Drop in cyclone separator

The size of a cyclone made for best performance will depend on its real use, that is, on the type of solid material to be removed and the removal quality needed. Pressure drop across the cyclone separator is calculated by Equation 2.14.

$$\Delta P_{cyclone} = \xi_c \frac{1}{2} \rho_a v^2 \tag{2.14}$$

$$\xi_c = \xi_g \times \xi_s \tag{2.15}$$

ξ_g is the effect of cyclone geometry and ξ_s solid loading on cyclone pressure drop. ξ_s is approximately constant, equal to 0.5 over a solid loading range of up to 20 kg of solid/kg of air.

2.3. Empirical models for pressure drop in pneumatic conveyors

Accurate prediction of pressure drop is essential for efficient pneumatic conveying, especially for different materials. Traditional scale-up models worked for similar systems but lacked adaptability for modern designs. Piece-wise modeling of feeders, straight pipes, bends, and cyclone separators allows more precise predictions, as pressure drop is mainly correlated with air velocity. The Divided Mills scale-up technique in Equation 2.16 is limited to pipeline size but provides a full-system estimate: where, m_{s1} and m_{s2} = solid mass flow rate (kg/s), D_1 and D_2 = pipe diameter (m), and L_1 (m) and L_2 (m) were adjusted lengths to account for bends and pipe components (Datta & Ratnayaka, 2003).

$$m_{s2} = m_{s1} \frac{L_1}{L_2} \left(\frac{D_2}{D_1} \right)^{2.8} \tag{2.16}$$

For single-phase air flow, Darcy's equation is widely used:

$$\Delta P = 4 \frac{f \rho_a v^2 L}{2D} \tag{2.17}$$

In gas-solid flow, the total pressure drop in Equation 2.18 is separated into air-only and solids contributions: *f* is the air friction factor, and K is the pressure drop coefficient (Bradley & Reed, 1990; Lee et al., 2004).

$$\Delta p_{total} = \Delta p_{air} + \Delta p_{solids} \tag{2.18}$$

Discrete calculation of pressure drop considers feeders, straight pipes, bends, cyclones, and valves separately. Pressure drop for straight pipes is calculated as Equation 2.19: where K_{st} is the straight-pipe coefficient, v_{entry} is gas velocity at the inlet, ΔL is pipe length, D is pipe diameter, and ρ_{sus} is suspension density (Pan & Wypych, 1992; Shamlou, 1988).

$$\Delta p_{st} = \frac{1}{2} K_{st} \rho_{sus} v_{entry}^2 \frac{\Delta L}{D} \tag{2.19}$$

Pressure drop for bends calculates as Equation 2.20, K_b is the bend pressure drop coefficient. The coefficient K_b is a function of $(v_{entry})^2$ and is largely independent of pipe size (Datta & Ratnayaka, 2003).

$$\Delta p_{bends} = \frac{1}{2} K_b \rho_{sus} v_{entry}^2 \tag{2.20}$$

2.4. Total pressure drop

Total pressure drop is the sum of pressure drops for components: feeder, straight pipes, bends, and cyclone separator. These form basic parts of the system, where each element adds some unique value toward the overall pressure drop that will eventually affect the efficiency and performance of the system. Contributions such as these towards pressure drop must be clearly understood to enable optimum design and operation of pneumatic conveying systems (Shijo & Behera, 2021b). The total pressure drop is calculated using the following Equations 2.21 and 2.22:

$$\Delta P_{total} = \Delta p_{feeder} + \Delta p_{hor} + \Delta p_{ver} + \Delta p_{bend} + \Delta p_{cyclone} \tag{2.21}$$

$$\Delta P_{total} = \frac{1}{2} K_f \rho_g v_{entry}^2 + \frac{1}{2} K_{st} \rho_{sus} v_{entry}^2 \frac{\Delta L}{D} + \frac{1}{2} K_b \rho_{sus} v_{entry}^2 + \frac{1}{2} K_c \rho_g v_{entry}^2 \tag{2.22}$$

Friction losses in horizontal pipes depend on the diameter, velocity of material through the pipe, and length of the pipe; vertical pipes will lose frictional resistance but will also be subjected to gravity effects, which will further enhance the overall pressure drop. These were the energy considerations that were needed to convey materials successfully within the system (Freitas et al., 2019). Suspension density (ρ_{sus}) is calculated as Equation 2.23.

$$\rho_{sus} = \frac{m_a + m_s}{V_a + V_s} \tag{2.23}$$

Bends in the system create additional pressure losses due to sudden changes in flow direction and the resulting turbulence. The cyclone separator also adds resistance, influenced by airflow characteristics and separation efficiency. Together, these components enable a comprehensive evaluation of the system's overall pressure drop, performance, and energy consumption (Dutta et al., 2016; Fu et al., 2021).

2.5. Power Requirement

Power requirements in a pneumatic conveyor depend on the flow regime, material properties, and system design. The flow regime, whether dilute-phase or dense-phase, is the main factor, with dilute-phase conveying requiring higher power due to suspended particles and increased pressure drop. Material properties such as particle size, shape, density, and moisture content, along with particle-wall interactions, also influence power demand. Proper system design and flow management can improve efficiency and reduce energy consumption (Sharma & Mallick, 2021; Kilickan & Guner, 2010).

The power required for pneumatic conveying is calculated as the product of the airflow rate and the system pressure drop. The actual blower power, adjusted for blower efficiency, is determined using Equations 2.24 and 2.25 as follows:

$$P = Q \cdot \Delta P_{total} \tag{2.24}$$

$$P_{input} = \frac{Q \cdot \Delta P}{\eta_{blower}} \tag{2.25}$$

2.6. Recent Advances in research on pneumatic conveying characteristics of materials

Traditional models were limited when dealing with complexities such as pressure drop and flow regimes. Recent improvements brought about by machine learning extensions, namely artificial neural networks, have accomplished much better prediction accuracy characterized by low errors. In combination with computational fluid dynamics, hybrid modeling further supports the design of more optimal and sustainable systems. The present work underlines major machine learning, CFD, and hybrid model developments pertinent to applications for real-time monitoring, erosion prediction, and energy efficiency (Ghode et al., 2017).

Recent studies have increasingly applied machine learning methodologies for the modeling of pneumatic conveyors, specifically artificial neural networks and Random Forests. ANNs in the predictions of pressure drop, flow regimes, and particle behavior with very high accuracy and low computational cost. For example, ANNs have successfully been applied to dense phase conveying with error margins achieved within ±10% (Kaur et al., 2017).

Developments in CFD have enabled more accurate modeling of gas-solid flows in pneumatic conveying. Improved turbulence models and particle tracking schemes were available for dense and dilute-phase flows. Coupled CFD and DEM can also improve the knowledge of the particle-particle interactions and particle wall interactions, and help to predict wear erosion and flow instabilities (Xu & Scholar, 2023).

Due to their ability to enhance prediction accuracy and lower computational expenses, hybrid models comprising elements of both machine learning and CFD were increasingly attracting attention. Machine learning optimizes the parameters of CFD or predicts the boundary conditions in this type of coupled model. Researchers have successfully applied hybrid models to optimize the design of pneumatic conveying systems, yielding notable increases in efficiency and performance (Liu et al., 2024).

Digital twin and IoT in pneumatic conveying system monitoring and control. A digital twin is a virtual copy of a physical process, where sensor data from a system is used in a prediction model to optimize the system or predict future failures. IoT sensors and machine learning algorithms enable smart monitoring of machines and their operation in a pneumatic conveying system, thus contributing to energy efficiency and minimizing downtime and maintenance expenses (Daraba et al., 2024).

Numerous studies have been conducted to improve the modeling of dense phase conveying, which is a highly heterogeneous flow. Significant improvements have been made in the prediction of pressure drops and flow stability with dense phase conveying through advances such as machine learning and CFD. Erosion and wear prediction models have also been developed to aid material specification and design in the mining process (Abe et al., 2023).

Researchers were dedicated to pneumatic conveying systems optimized in terms of energy consumption and environmental impact. The use of machine learning models to reduce power consumption and emissions is being explored, while CFD simulations assist in the design of a more efficient conveying system (Gomes et al., 2021).

2.7. CFD models for pneumatic conveying systems

Computational Fluid Dynamics has proven to be an invaluable tool for investigating and optimizing pneumatic conveying systems, offering enhanced insight into the complex interactions between gas and solid phases. Pneumatic conveying is widely used in many industries, from agriculture to food packaging, for the transportation of bulk materials through pipes by air or other gases (Agnol et al., 2020).

The coupled equations for the gas and solid phases can be written as: the continuity equation represents the principle of mass conservation. In a fluid flow system, the mass of fluid entering a control volume must be equal to the mass of fluid leaving it, for no accumulation or depletion to occur. Continuity equation for a single-phase flow for a fluid only for a steady state, incompressible fluid (Ambrosio & Crippa, 2014). The continuity equation in differential form is:

$$\frac{\partial \rho}{\partial t} + \nabla\left(\rho \vec{V}\right) = 0 \tag{2.26}$$

In incompressible flow (like low-speed air flows in many dilute-phase applications), density (ρ) remains constant, simplifying the continuity equation to:

$$\nabla \cdot \vec{V} = 0 \tag{2.27}$$

In Cartesian coordinates:

$$\frac{\partial u}{\partial x} + \frac{\partial v}{\partial y} + \frac{\partial w}{\partial z} = 0 \tag{2.28}$$

Continuity for two-phase flow for gas-solid flow in a two-phase system (like air and particles), we account for both phases: Carrier phase (air): governed by continuity for compressible/incompressible flow. Discrete phase (particles): mass conservation depends on particle concentration and velocity relative to the fluid (Fu et al., 2021). The continuity equations for each phase can be written as:

$$\frac{\partial\left(\alpha_g \rho_g\right)}{\partial t} + \nabla \cdot \left(\alpha_g \rho_g \vec{V}_g\right) = 0 \tag{2.29}$$

$$\frac{\partial\left(\alpha_s \rho_s\right)}{\partial t} + \nabla \cdot \left(\alpha_s \rho_s \vec{V}_s\right) = 0 \tag{2.30}$$

In pneumatic conveying, volume fraction α is small for the solids dilute phase, the particles are far apart, and most of the space is occupied by air. The momentum equation is just Newton's second law of motion applied to flow. The rate of change of momentum of a fluid particle is equal to the sum of the forces acting on it. The momentum equation for a single-phase flow of an incompressible, Newtonian fluid, the Navier-Stokes equation, is:

$$\rho\left(\frac{\partial \vec{V}}{\partial t} + V \cdot \nabla \vec{V}\right) = -\nabla p + \mu \nabla^2 \vec{V} + \rho \vec{g} \tag{2.31}$$

$$\rho_g = \left(\frac{\partial \vec{V}_g}{\partial t} + \vec{V}_g \cdot \nabla \vec{V}_g\right) = -\nabla p + \mu_g \nabla^2 \vec{V}_g + \rho_g g + \vec{F}_{\text{int}} \tag{2.32}$$

$$\rho_g = \left(\frac{\partial \vec{V}_s}{\partial t} + \vec{V}_s \cdot \nabla \vec{V}_s \right) = \rho_s g + \vec{F}_{\text{int}} \tag{2.33}$$

$\vec{F}_{\text{int}}$ is represents the drag force exerted by the gas on the particles, a key factor in pneumatic conveying, as it impacts the velocity and trajectory of particles.

CFD provides comprehensive insight into particle-fluid interactions and is essential for modeling and simulating pneumatic conveying systems. The choice of modeling methodology and coupling strategy depends on the complexity of the system and available computational resources (Dou et al., 2023). CFD models generally adopt two main approaches depending on flow conditions. The CFD-DPM (Eulerian-Lagrangian) model is suitable for dilute systems, where particles are dispersed, and collisions are minimal, whereas CFD-DEM is effective for predicting particle aggregation and collisions. Dense Discrete Phase Models (DDPM) and Two-Fluid Models (TFM) perform well in medium- to dense-phase flows, while hybrid models were applied to complex systems. These models improve system design by predicting particle movement and solving practical issues like wear and separation in applications including grain handling and mining (Singh et al., 2023; Remy et al., 2009; Hashemisohi et al., 2019; Verma & Padding, 2020; Roberts et al., 2022; Erken et al., 2024).

CFD-DPM simplifies collision management for low concentrations of solids and is straightforward to implement, though it loses accuracy in dense-phase flows. CFD-DEM combines Eulerian gas modeling with Lagrangian particle dynamics to accurately simulate collisions and particle clustering, but it demands higher computational resources and is challenging for larger systems. DDPM uses an Eulerian approach for gas and a continuum method for solids to balance accuracy and efficiency, performing well in moderate transitional flows but failing in fully dense or very dilute regimes (Agnol et al., 2020; Yang et al., 2020; Cao et al., 2022).

TFM model couples the Eulerian approach with kinetic theory to handle dense-phase collisions but cannot follow individual particles, limiting its accuracy in dilute flows. Euler-Lagrange hybrid models combine both methods to capture complex transitional flows, as seen in food and pharmaceutical applications, though it require precise configuration and parameter tuning. The MMPIC model applies Eulerian methods for gas and statistical parcels for solids, showing strength in dense-phase mining applications but limited precision in detailed particle interactions (Verma & Padding, 2020; Roberts et al., 2022; Erken et al., 2024).

Generally, Euler-Lagrangian approaches track individual particles in a continuous fluid and were ideal for low-density flows, while Euler-Euler methods treat both phases as continuous, performing best for dense flows and large-scale system behavior. Coupling strategies, such as two-way, four-way, and six-way interactions, determine how particle-fluid and particle-particle interactions are handled. CFD-DPM is suitable for dilute flows, CFD-DEM for dense collisions, and DDPM provides a hybrid solution for intermediate conditions.

The DEM-CFD coupling allows the simulation of particle-fluid systems by managing particle interactions at the computational cell level without high computational costs (Lenaerts et al., 2013; Erken et al., 2024). This method enables detailed studies of particle motion, collisions, and heat transfer, including non-spherical and cohesive particles, as well as particle-wall interactions (Guzman et al., 2020). Traditional continuum approaches, in contrast, use particle tracking without solving complex interaction equations, maintaining computational efficiency even when particle size distribution or concentration changes (Remy et al., 2009).

Erken et al. (2025) examined coarse-grained CFD-DEM strategies for horizontal plug-flow pneumatic conveying. It was compared scaling methods for contact and drag forces and identified settings that preserve flow accuracy while reducing computation time. The findings help improve reliability and efficiency in dense-phase conveying simulations and highlight the importance of model-scaling decisions.

Particle-fluid interactions were dominated by drag forces in dilute-phase flows, with other forces such as pressure gradients, virtual mass, and lift often being negligible. Drag correlations, such as those proposed by Schiller & Naumann (1933), Dalla (1948), and Haider & Levenspiel (1989), were used to compute forces on both spherical and non-spherical particles, taking into account particle sphericity and Reynolds number effects (Zhou et al., 2019; Emam et al., 2021). CFD simulations employ Euler-Euler or Euler-Lagrange frameworks to predict particle movement and system behavior accurately (Lia et al., 2016).

CFD-DPM is effective for dilute-phase flows with solid volume fractions below 10%, ensuring air dominates the flow and particles are sparsely distributed. The model accurately predicts particle trajectories and distributions, with simulations converging based on scaled residuals (Agnol et al., 2020; Yang et al., 2020; Cao et al., 2022).

In high-speed pneumatic systems, Reynolds numbers were generally above 2300, indicating turbulence, which must be accounted for in momentum and pressure predictions (Huang et al., 2021). Turbulence models such as standard k-ε, RNG k-ε, k-ω SST, LES, and DES improve accuracy. The standard k-ε model was efficient for basic dilute-phase flows (Dutta, 2019), while RNG k-ε enhances predictions in swirling or transitional flows (Singh, Gill, et al., 2023). The k-ω SST model captures near-wall effects and bends effectively (Chebra et al., 2024), LES resolves unsteady complex flows with high accuracy (Fredriksson, 1999), and DES provides a balance between precision and computational efficiency (Singh et al., 2023).

CFD methods allow for detailed analysis and optimization of pneumatic conveying systems. The selection of an appropriate model and turbulence method depends on particle concentration, flow density, and computational resources. Accurate simulation of particle-fluid interactions and turbulence is critical for designing efficient, reliable, and high-performance pneumatic conveying systems (Dutta, 2019; Dou et al., 2023; Singh et al., 2023; Erken et al., 2024).

Dikty (2025) experimentally investigated pressure behavior in pneumatic conveying systems handling fine bulk solids. The study measured pressure fluctuations under different gas velocities and solids loading and applied signal-analysis methods to link fluctuation patterns with flow regime transitions. This work provides strong experimental insight into unsteady flow characteristics and supports validation frameworks for numerical pneumatic-conveying models.

2.8. ANN prediction model

Traditional modeling approaches struggle to accurately predict pneumatic conveying system performance due to the complex properties of bulk materials. Machine learning (ML) addresses this by analyzing large datasets to uncover patterns that improve prediction accuracy, enabling real-time system optimization and control (Shijo & Behera, 2023). Recent studies have demonstrated that ML enhances understanding of pneumatic conveying features, including pressure drop, material velocity, and flow stability. Techniques such as artificial neural networks (ANN), support vector machines, and decision trees have successfully modeled systems that conventional methods cannot handle, accommodating variations in material properties, flow conditions, and system configurations (Vinuesa et al., 2023).

ANN models, for instance, employ different training algorithms such as Levenberg-Marquardt, Scaled Conjugate Gradient, and Bayesian Regularization to optimize prediction performance. These algorithms adjust network weights and biases through iterative training, using activation functions to generate outputs. Levenberg-Marquardt is preferred for larger datasets due to its balance of speed and accuracy, while Bayesian Regularization enhances generalization by reducing overfitting, and Scaled Conjugate Gradient provides computational efficiency (Alizadehdakhel et al., 2009; Lashkar et al., 2012).

ML applications improve pneumatic conveying system design and operation by predicting performance, minimizing energy consumption, and optimizing material handling efficiency (Shijo & Behera, 2021b). Predicting pressure drops in both dilute- and dense-phase flows is a growing trend, as ML can capture complex interactions among particles, fluid, and pipe surfaces, offering more reliable results than conventional approaches (Shadloo et al., 2020; Shijo & Behera, 2023). Studies have applied ANN models to dense-phase pneumatic conveying, showing deviations as low as 10%, and demonstrating improved accuracy in larger datasets when using Levenberg-Marquardt (Shijo & Behera, 2021).

ML has also been applied beyond simple prediction. For instance, Lagrangian-based CFD studies of cyclone separators paired with neural networks improved the prediction accuracy of separation efficiency by 32.5% compared to conventional surrogate models (Park & Go, 2020). Random Forest regression has been used in oil and gas systems to predict particle erosion with high precision, simplifying complex modeling tasks (Zahedi et al., 2018). Other studies applying ANN to multiphase vertical flows and cyclone separator design have confirmed the superiority of ML in predicting pressure drops and optimizing system performance (Osman et al., 2005; Elsayed & Lacor, 2012).

Machine learning has significantly enhanced the design, operation, and optimization of pneumatic conveying systems. By accurately predicting pressure drops, improving cyclone separator efficiency, and modeling particle erosion, ML provides a practical, high-precision alternative to conventional approaches, especially for dense-phase and complex flow systems (Shadloo et al., 2020; Shijo & Behera, 2023).

2.9. Significance of hybrid CFD-ANN approach

The experimental results were employed to verify the CFD simulations for interrupted plate fins, which confirmed the precision of the modeling. CFD simulations generated enough relevant data that made additional experiments unnecessary for ANN model training. The hybrid CFD-ANN approach generated superior results than traditional methods because ANN models successfully predicted heat transfer together with flow characteristics with high accuracy. The ANN approach validated by CFD produced superior predictive abilities regarding system performance than traditional methods (Beigzadeh et al., 2016).

The model uses a multi-fidelity Deep Neural Network structure to combine low- and high-fidelity data for its loss function calculation. The transonic flow simulation of the ONERA M6 wing demonstrates that the surface pressure distribution is predicted with high accuracy by this model because it uses both high- and low-fidelity data while surpassing predictions based solely on either type of data (Kou & Zhang, 2022).

The application of ANN with CFD-generated data for the Electronic Continuously Variable Transmission system machine learning training yields superior outcomes than relying solely on experimental information. Imaging reconstruction through CFD-ANN methods achieved better accuracy at quicker speeds compared to reconstruction based only on experimental data, which struggled with noise interference. Combining simulated data with experimental knowledge produced the best outcome because it enabled the attainment of superior results (Montilla et al., 2024).

Using both experimental results along with CFD-generated data for training the 12-9-5-2 feed-forward ANN architecture leads to superior accuracy for predicting heat transfer and flow resistance in fin-and-tube heat exchangers. The implementation of experimental combined with CFD-generated data improves the model's generalization capability to enhance its effectiveness and versatility in heat exchanger performance insights (Tang et al., 2016).

Wan et al. (2025) developed Trajectory Flow Net, a deep-learning model combining Lagrangian particle data and Eulerian flow fields for efficient trajectory prediction.

Validated using numerical and experimental flow data, the approach offered accurate particle-motion forecasting at lower computational cost. Although not exclusive to pneumatic conveying, it demonstrates the value of hybrid physics-ML methods in particle-flow environments.

2.10. Application of pneumatic conveying system in bulk material handling

Pneumatic conveying systems operate as multiphase flow systems that transport materials through gas-solid mixtures. The process relies on a high-velocity air stream that carries solid particles such as grains and powders. The core behavior of pneumatic conveying arises from the interaction between the gas and solid particles, allowing efficient bulk material transport over short to moderate distances in a wide range of industries, including agriculture, processing, and manufacturing.

As demonstrated in Figure 1.3, which illustrates various applications of pneumatic grain conveyors, including (a) pneumatic seeder of Zubrilina et al. (2017), (b) pneumatic chickpea harvester of Helali et al. (2023), (c) pneumatic grain cleaner of Fernando & Hanna (2005), (d) pneumatic dryer of Chan et al. (2015), (e) pneumatic grain loader of El-kholy & Kamel (2021), and (f) wheat milling plant of Brothers Flour and Biscuit Factory in Adama, Ethiopia (2025). Row planting of teff can increase yields by 29.2 to 39.3% compared to traditional broadcasting (Chekole et al., 2019).

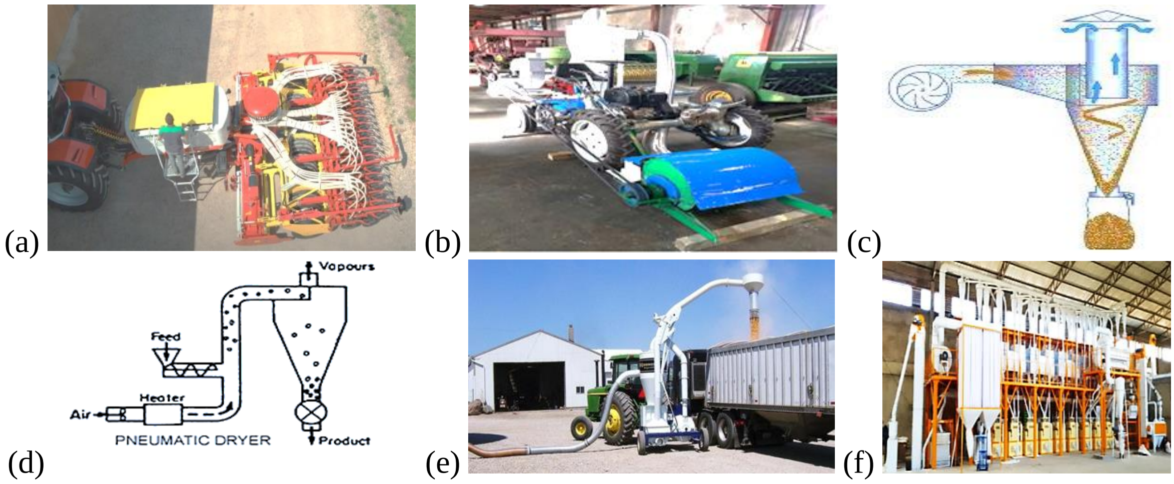

Figure 2.3. Application of pneumatic grain conveyor in grain handling processes

Using pneumatic conveyors, grains receive gentle handling, which results in mechanical damage rates below 5% for wheat and barley. The delicate treatment of grains during transport is essential for preserving their market value as well as their quality (Gu, 2018). According to Guner (2007) breakage rate for some agricultural seeds, such as wheat, barley, sunflower, and lentil, showed an increase in air velocity from 12.70 to 32.52 m/s. Mechanical damage varied from 0.39%, 1.46%, 4.14%, and 8.26% to 0.96%, 3.60%, 10.17%, and 20.27%, respectively.

During pneumatic conveying operations, pulses show heightened vulnerability to mechanical harm. Reported damage levels range between 15% and 30% and depend on factors including pulse type and conveying velocities. The probability of damage increases when materials move at increasing speeds because of the elevated risk of both impact and abrasive contact (Kiliçkan & Güner, 2010).

The handling of bulk agricultural materials, including grain processing and pneumatic conveying systems faces severe danger from grain dust explosions. Specific conditions, including ignition sources with adequate dust concentration along with oxygen availability, can trigger highly combustible grain dust to ignite. Pneumatic conveying systems that move grains through air-based transportation create an elevated risk of dust accumulation (Alauddin et al., 2024).

Dust extraction systems play a critical role in minimizing the likelihood of grain dust explosions that could occur in these installations. The installation of cyclone separators, together with bag house filters and dust collectors, provides an effective method to eliminate airborne dust particles from the conveyor system. The combination of regular maintenance with proper connection sealing and controlled airflow velocity helps to minimize dust generation and accumulation. The implementation of safety measures, including explosion venting along with flame arrestors and continuous dust level monitoring, leads to a significant decrease in explosion risks during pneumatic conveying operations (Furlong et al., 2024).

The agricultural machine known as a pneumatic seeder utilizes air pressure to deliver seeds evenly across agricultural fields. Precision agriculture relies on this equipment because it achieves precise seed positioning and proper seed distribution alongside effective seed usage (Liu et al., 2024).

A machine designed for harvesting jojoba seeds works efficiently by utilizing a drive system, together with adjustable controls and a collection bin. The pneumatic grain dryer functions through heated air and airflow to achieve uniform grain drying with its moisture sensors and adjustable settings for different grain types. The method reduces damage and maximizes energy savings while providing a quicker alternative to standard drying methods (Sarkis & Energia, 2025).

The virtual coffee bean model simulates key physical properties such as shape, size, density, and moisture content. The roasting system includes heating and cooling units and an air-circulation setup to control temperature and airflow for proper roasting. DEM sensors capture temperature, pressure, and bean-environment interactions, while the CFD model visualizes airflow inside the roaster to ensure even heat distribution and uniform roasting (Hlosta et al., 2019).

Wheat flour millers use appropriate pneumatic conveyors to move wheat and flour efficiently through their production stages. The system automatically moves materials between production stages to maintain high levels of sanitation and safety while decreasing contamination risks and enhancing operational efficiency throughout the milling process (Paber et al., 2016).

Particle-particle and particle-wall collisions in DEM were treated using a soft-spheres approach. In contrast, a hard-sphere modeling of particle-wall interactions was realized in DPM. DEM was more accurate and physically correct for simulating bulk material behavior, especially when particle-particle interactions were important(Singh et al., 2023). DEM's ability to capture the complex behavior of particles, such as deformation, breakage, and fragmentation, makes it an attractive choice for studying the transport of polyethylene pellets in pneumatic conveyors (Lenaerts et al., 2013).

DPM's simplicity and efficiency make it an attractive choice for studying PC, especially when dealing with large-scale systems or when a high degree of accuracy is not required (Jorhal et al., 2021). The study provided a method for the rapid optimization design of the pneumatic conveying system of the hybrid rice pollen collection unit, and the results could provide a reference for the optimization design of the pneumatic conveying system of the hybrid rice pollen collection unit (Xiao et al., 2019).

Gas-solid flow systems require pneumatic conveying systems as an essential component. The research on particles larger than 5 mm remains limited, even though the scientific investigation has extensively covered particles smaller than 5 mm. The simulation results of horizontal coal particle transport using Euler-Lagrange and DPM methods demonstrated accurate trajectory predictions, which confirmed the practicality of the approach. Through multifactor simulations, scientists analyzed particle dimensions together with flow speed, solid-gas concentration, and pipe size to identify wall abrasion effects, which would improve large-particle system design (Yang et al., 2020).

A DEM and DPM model was implemented to simulate polyethylene pellet horizontal pneumatic transport through numerical analysis. Two versions of FLUENT DPM were tested against each other: the standard built-in version and a customized version that included hard-sphere particle interactions. The DEM analysis demonstrated close agreement with airflow patterns, whereas DPM simulations achieved satisfactory results under conditions of dilute flows (< 0.1). Changes in flow patterns occurred through the addition of particle interactions to DPM, which led to decreased formation of non-physical suspended clouds. The DPM model demonstrated numerical divergence when particle volume fractions exceeded 0.101 (Mezhericher et al., 2011).

According to Atzeni et al. (2021) discrete phase model (DPM) was used to investigate complex particle dynamics in human respiratory investigations while analyzing sedentary breathing patterns. The method enables researchers to study airflow behavior along with particle distribution and deposition patterns inside the respiratory passage by considering multiple variables, including airway structure, breathing frequency, and particle dimensions. Through DPM integration, researchers obtain knowledge on the lung behavior of aerosols and pollutants, and medical aerosols, which benefits the creation of drug delivery devices, inhalation treatments, and environmental air quality monitoring systems.

2.11. Summary

Teff grain has been widely recognized for its unique characteristics compared to other cereal grains, primarily due to its extremely small particle size. Different studies have highlighted that the fine nature of teff complicates handling, storage, and transportation, often resulting in significant postharvest losses. Despite its increasing global importance, research on optimized handling technologies for teff remains limited, indicating a critical gap in postharvest management. Therefore, it is important to develop tailored handling methods that can substantially enhance production efficiency, postharvest management, and improve industrial applications of teff grain.

Several researchers have focused on the role of aerodynamic properties, particularly terminal velocity, in the design of postharvest handling systems for cereal grains. Terminal velocity provides an estimate of the air velocity required to suspend a particle in a fluid, which is fundamental for pneumatic transport, cleaning, and drying operations. However, terminal velocity calculations typically consider single, isolated particles and do not account for particle-particle interactions in concentrated flows. Consequently, while terminal velocity provides initial guidance, it is insufficient for accurately predicting the flow behavior of particle-laden flows in pneumatic conveyors.

In the design of pneumatic conveying systems, numerical and experimental studies have emphasized the importance of minimum conveying velocity, also known as saltation velocity. Unlike terminal velocity, saltation velocity accounts for key factors such as particle concentration, solid loading ratio, particle size and density, pipe diameter, and flow conditions. Studies show that using saltation velocity provides a more realistic estimate of the air velocity needed to initiate and maintain particle transport, ensuring reliable and efficient operation of pneumatic conveying systems under varying conditions.

Theoretical modeling of bulk agricultural materials presents additional challenges. Agricultural grains often exhibit irregular shapes, variable sizes, and heterogeneous properties, making analytical solutions difficult to apply. Several studies emphasize that accurately determining material-specific parameters, such as the solid friction coefficient, is critical for predicting particle-particle and particle-wall interactions. The uncertainties associated with these parameters limit the reliability and practical applicability of purely theoretical approaches for pneumatic conveying systems.

Empirical modeling based on laboratory experiments has historically been used to predict the behavior of pneumatic conveyors. However, recent literature highlights several limitations of empirical approaches, including restricted data availability, high experimental costs, labor-intensive procedures, and limited flexibility for different operating scenarios. These constraints reduce the generalizability and predictive capability of empirical models, limiting their application in full-scale industrial systems.

Numerical simulation, particularly CFD-DPM, has emerged as a reliable and cost-effective method for studying dispersed particle flows in dilute-phase pneumatic conveying. Recent numerical studies have shown that the standard k-ε turbulence model effectively captures basic dilute-phase flow behavior in straight pipes, while the RNG k-ε model improves prediction accuracy in swirling, transitional, or cyclone separator flows. CFD-DPM provides detailed visualization of velocity fields, particle trajectories, and pressure distributions, offering insights that were often difficult or costly to obtain through experiments alone.

Artificial Intelligence-based models, particularly those employing Artificial Neural Networks, have been increasingly applied in recent studies for predicting key parameters in pneumatic conveying systems. Literature indicates that AI-based models achieve higher accuracy, adaptability, and computational efficiency than traditional empirical or theoretical methods, making them suitable for complex particle-fluid systems under varying operational conditions.

Recent studies collectively highlight that integrating experimental data, numerical simulations, and AI-based modeling offers a powerful hybrid approach for understanding and optimizing pneumatic conveying systems. This methodology allows researchers to capture complex fluid-particle interactions while providing robust, high-accuracy predictions. Such integrated approaches enable the development of scalable, cost-effective solutions, minimizing losses and improving overall postharvest efficiency.

CHAPTER THREE

MATERIALS AND METHODS

3.1. Description of the study area

The study was conducted at Adama Science and Technology University, using laboratories from the Mechanical, Chemical, Materials Engineering, and Applied Biology departments. The university is located in Adama City at 8.54°N 39.27°E at an elevation of 1712 meters, 99 km southeast of Addis Ababa in the East Showa Zone of Oromia. Adama lies within the Main Ethiopian Rift and Awash River Watershed, with elevations ranging from 1489 to 1976 meters and terrain characterized by flatlands bordered by plateaus and mountains (Leta et al., 2024).

3.2. Materials

3.2.1. Teff grain

Eight varieties of teff grain were selected for this study based on distinct characteristics such as varieties, color, and year of release. These varieties include Boset (DZ-Cr-409), Kora (DZ-Cr-438RIL133B), Dagim (DZ-Cr-438RIL91A), Felagot (DZ-Cr-442RIL77C), Bora (DZ-Cr-453RIL120B), Ebba (DZ-Cr-458RIL18), Bishoftu (DZ-Cr-497 RIL133), and Boni (DZ-Cr-498RIL37) as shown in Figure 3.1. Samples were sourced from DZARC under EIAR’s national teff improvement program. To ensure consistency, samples were sorted and stored at room temperature before testing.

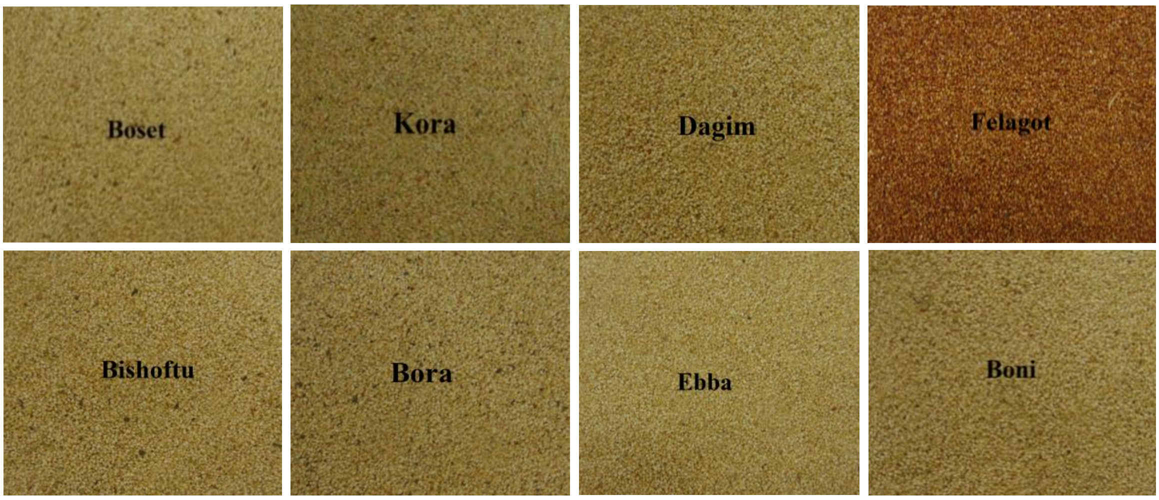

Figure 3.1. Different varieties of teff grain

3.2.2. Measuring instruments and apparatus used for laboratory tests

These included a laboratory oven for moisture content measurements, an electronic balance for accurate mass measurements, and scanning electron microscopy for particle size and sphericity measurements. A CEL-MKII fluidized bed test apparatus is used to determine gas fluidization characteristics of the teff grain, which is critical for the selection of the phase of pneumatic conveying. Air velocity and pressure drop recording sensors, such as digital anemometers and manometers, were installed to monitor air velocity and pressure variations within the system, and a manometer was linked to the pipeline through hoses and connectors. All those instruments and apparatus collectively enabled a detailed investigation of the characteristics of teff grain in a positive-pressure dilute-phase pneumatic teff grain conveying system.

3.2.3. Electronic balance

Electronic balance scales ranged from 0 to 3 kg with an accuracy of 0.1 g, and scales ranging from 0 to 250g with an accuracy of 0.01mg were used for weighing grain samples. This instrument provides accurate grain mass measurements, which were crucial for determining grain mass, moisture content, and densities.

3.2.4. Laboratory oven

A laboratory oven is used to measure moisture content at a controlled temperature, typically between 100°C and 105°C. The procedure involves weighing each sample before and after drying for a specified period according to ASAE Standard S352.3 (ASAE, 1994). The weight loss, calculated as the difference between the initial and final mass of teff grain and the moisture content, is expressed as a percentage of the original mass.

3.2.5. Sieve shaker

A sieve shaker (mechanical) was used to determine the particle size distribution of the teff grain through sieve analysis, featuring a set of five test sieves, each with a diameter of 200 mm with mesh sizes of 2 mm, 1 mm, 710 µm, 500 µm, and 355 µm.

3.2.6. Scanning electron microscopy

SEM was employed to examine the physical and structural characteristics of teff grain. Operating at magnifications ranging from X10 to X500,000 and accelerating voltages between 1 kV and 30 kV, the SEM provided high-resolution images that enabled precise analysis of grain size distribution and shape. The teff varieties analyzed for this characterization were Felagot (DZ-Cr-442RIL77C), Bishoftu (DZ-Cr-497RIL133), and Boni (DZ-Cr-498RIL37), which were selected according to their distinct characteristics, such as variety, color, and year of release. SEM analysis was conducted in the Microbiology Laboratory, Department of Applied Biology, School of Applied Science at Adama Science and Technology University.

3.2.7. Angle of repose tester

The angle of repose of teff grain was measured using a specialized instrument known as an angle of repose tester, also referred to as a repose angle measuring device. This device assesses the maximum angle at which the teff grain can be heaped without slumping, providing valuable information about its flowability and cohesion. The measurement involves allowing the grain to form a cone-shaped pile, and the angle between the slope of the pile and the horizontal base was recorded as the angle of repose (Abebaw & Abera, 2020). The laboratory test was conducted at the Chemical Engineering Department Laboratory of Adama Science and Technology University.

3.2.8. CEL-MKII fluidized bed test apparatus

The Armfield CEL-MKII fluidized bed test apparatus was used to investigate gas fluidization characteristics of teff grain, with a particular focus on determining the minimum fluidization velocity and pressure drop through the bed. This versatile apparatus was designed to analyze fluid-particle interactions. The teff grain varieties used in this study, Felagot (DZ-Cr-442RIL77C) and Boset (DZ-Cr-409) were selected depending on their distinct size and color. The experimental work was conducted at the Chemical Engineering Department Laboratory of Adama Science and Technology University.

3.2.9. Air velocity measurement sensor

The GM-816 professional digital anemometer was used to measure air velocity at the inlet of pneumatic conveying systems. This instrument accurately gauged air velocity with a resolution of 0.1 m/s. It could measure air velocity up to 30 m/s, with an accuracy margin of ±5%. It facilitated effective material transport and maximized energy efficiency.

3.2.10. Pressure measurement sensor

A Man-45 professional digital manometer was used to track pressure difference in the system with an impressive measurement accuracy of 0.01 kPa. This instrument was compatible with both single and dual-pipe differential pressure setups. In contrast to conventional mechanical manometers, it provided enhanced precision, suitability, and portability. It came equipped with a sizable, illuminated dual LCD screen, a zeroing feature, the choice to turn off auto power-off, offset correction capabilities, and data compensation functions, all designed to enhance measurement accuracy.

3.2.11. Hose and Connector

Hoses and connectors were used to create a link between the manometer and the system. The hoses and connectors with an 8mm inner diameter facilitated a stable connection, minimizing the risk of leaks and ensuring reliable data collection for pressure drop measurements across different sections of the system.

3.2.12. Statistical analysis tools

Statistical analysis was performed utilizing IBM SPSS Statistics 22 and Microsoft Excel version 10. This software enables statistical analysis, including descriptive statistics, ANOVA, significance testing, and regression analysis. It was an aid to deriving meaningful insights for results from findings.

3.2.13. Computational tools

Computational simulations were conducted using Rocky DEM to model the terminal velocity of cereal grains. ANSYS 2024R1 and ANSYS 17.2 were employed for 3D modeling, mesh generation, and system simulation. ANSYS Fluent facilitated detailed analysis of air velocity distribution, particle concentration, and pressure variations across different sections of the system, providing deeper insights into its operational characteristics.

3.2.14. Data processing and visualization tool

OriginPro 2024b was used for curve fitting and graph creation. It has advanced features that help to present the findings clearly and effectively, allowing for a visual representation of results and supporting the interpretation of the data.

3.2.15. ANN modeling tool

MATLAB 2019Ra with neural network toolbox (nntool) was employed to develop the predictive model for pressure drop. This software facilitated the design, training, validation, testing, and simulation of neural network-based prediction models, ensuring reliable predictions based on combined experimental and CFD-DPM simulation results.

3.3. Methods for determination of engineering property and design of system

Collected teff grain samples were cleaned, sorted, and properly stored to preserve quality and moisture content. These samples were used for laboratory experiments to determine physical, frictional, and aerodynamic properties using appropriate instruments and computational tools. Tests included moisture content, particle size distribution, bulk density, angle of repose, frictional properties, as well as aerodynamic behavior such as terminal velocity, gas fluidization characteristics, and minimum conveying velocity. Each measurement was performed in replicates to ensure accuracy and reproducibility.

3.3.1. Moisture content

The moisture content of teff grains was determined using the oven-drying method following ASAE Standard S352.3 (ASAE, 1994) and the procedure described by Abewa et al. (2019). Approximately 10 g of the grain sample was weighed and placed in a hot-air oven at 105 °C for 24 hours. After drying, the samples were cooled in a covered container to room temperature and reweighed. Moisture content was calculated as the percentage weight loss. Each measurement was performed in triplicate, and the average value was reported.

3.3.2. Particle mean diameter

The dimensions of each teff grain length, width, and thickness in (mm) were measured using a scanning electron microscope (SEM). The SEM produced a 2D image, which allowed length and width to be determined directly, while the thickness was estimated based on the results of Abera (2020) and Awgichew (2019). From these measurements, the geometric and arithmetic mean diameters of the grains were calculated following the approach described by Klavins et al. (2016). All measurements were performed in triplicate to ensure accuracy and reproducibility.

3.3.3. Particle size distribution

The particle size distribution of teff grains was determined by sieve analysis using a set of five test sieves with a diameter of 200 mm and mesh sizes of 2 mm, 1 mm, 710 µm, 500 µm, and 355 µm. The procedure was carried out following the guidelines provided in ASTM D6913. All measurements were performed in triplicate to ensure accuracy and reproducibility.

3.3.4. Mass and density

The bulk density of teff grains was determined by filling a 250 ml graduated cylinder with a known mass of grain without compacting the sample. The mass was measured using a digital balance, and the volume was read directly from the cylinder. True density was measured using the liquid displacement method with toluene as the displacement liquid; a known mass of grains was carefully submerged in a graduated cylinder containing toluene, and the displaced liquid volume was recorded. Porosity and voidage were then calculated from the measured bulk and true densities using standard methods. All measurements were performed in replicates to ensure accuracy and reproducibility (Tsegaye and Abera, 2020).

3.3.5. Frictional property

The frictional property of teff grains was expressed by the angle of repose, which indicates how the material flows and feeds from the feeder hopper into the pneumatic conveying system. The angle of repose was measured using a specialized instrument called an angle of repose tester, which determines the maximum angle at which the teff grain can be heaped without slumping, providing information about its flowability and cohesion. The measurement involved allowing the grains to form a cone-shaped pile, and the angle between the slope of the pile and the horizontal base was recorded as the angle of repose (Abebaw & Abera, 2020; Sonawane et al., 2022). All measurements were performed in replicates to ensure accuracy and reproducibility.

3.3.6. Terminal velocity

The aerodynamic properties of teff grains, including drag coefficient, drag force, and terminal velocity, significantly influence airflow interaction, affecting blower air flow rate, transport velocity, and separator efficiency in pneumatic conveying systems. Terminal velocity occurs when gravitational and drag forces are balanced and depends on grain mass, size, shape, and air density, reflecting airflow resistance under flow conditions. Terminal velocity was calculated according to Equation 2.2 (Zewdu, 2007a).

3.3.7. Gas fluidization characteristics of teff grain

The pneumatic conveying and drying of bulk materials depend largely on bulk properties that govern material-air interactions, such as fluidization, air retention, and permeability. Fluidization tests were conducted to assess the behavior and suitability of teff grains in a dense-phase pneumatic conveyor. Laboratory experiments were performed to determine the minimum fluidization velocity and the maximum bed pressure drop, with calculations supported by the Carman-Kozeny equation. The minimum fluidization velocity was calculated for a particle mean diameter of 0.70 mm, an initial bed height of 0.3 m, and a bed diameter of 0.05 m according to Equation 2.6. Each measurement was performed in replicates to ensure accuracy and reproducibility.

3.3.8. Design of positive-pressure dilute-phase pneumatic conveying system

The design of a positive-pressure dilute-phase pneumatic conveying system involves several critical steps to ensure efficient and reliable transport of teff grains. First, appropriate pipe diameter and blower capacities were selected based on the material properties and required conveying rate. The feeder and cyclone separator were designed to match the flow characteristics of the grains, minimizing blockages and material losses. The minimum conveying velocity was determined to ensure particles remain suspended in the airflow, preventing settling within the pipeline. In addition, construction guidelines were established to provide practical specifications for the system layout, including pipe routing, joints, and supports, to maintain structural integrity and operational safety. Each design step was guided by both theoretical calculations and empirical data from laboratory tests on teff grain properties, ensuring the system could be reliably scaled and implemented.

3.3.9. Pipe selection

According to Wang et al. (2023), standard pipe sizes for pneumatic conveyors typically range from 40 mm to 200 mm in diameter. For this study, the selected pipes included a 50 mm rigid PVC pipe with an outer diameter of 50 mm, an inner diameter of 46 mm, a wall thickness of 2 mm, and a working pressure of 5.89 bar, colored grey. Additionally, a 75 mm rigid PVC pipe with an outer diameter of 75 mm, inner diameter of 71 mm, wall thickness of 2 mm, and a working pressure of 5.89 bar, also colored grey, was used for the experimental investigation of pressure drop through a section of the system components, as shown in Figure 3.4.

3.3.10. Blower selection

The selection of a blower for the positive-pressure dilute-phase pneumatic conveying system was based on the minimum conveying air velocity and the selected pipe diameter. In dilute-phase pneumatic conveyors, the minimum conveying air velocity typically ranges between 10 m/s and 30 m/s, ensuring that particles remain effectively suspended in the airflow, creating a lean flow suitable for long-distance conveying (Barrozo et al., 2010). For this study, a centrifugal blower (CZT-4 model) was selected. The blower specifications were as follows: operating voltage 380 V, rotation speed 2800 r/min, airflow rate 19 m³/min, wind pressure 1080 Pa, current 1.75 A, and power consumption 1100 W, as shown in Figure 3.4. These parameters were chosen to provide sufficient air velocity and pressure to maintain the required dilute-phase transport of teff grains while matching the pipe diameter and conveying distance.

3.3.11. Design of rotary feeder

A rotary feeder was commonly employed in a dilute-phase positive-pressure pneumatic conveyor to maintain a continuous material flow. The flow rate of bulk material from a hopper depends on several factors, including the hopper discharge rate, outlet diameter, material bulk density, internal friction, wall friction, and hopper inclination (Gandia et al., 2022). The flow rate of teff grains from the hopper to the pneumatic conveyor through the rotary feeder can be determined using the methods and equations provided, as shown in Equation 2.9 and Figure 2.10.

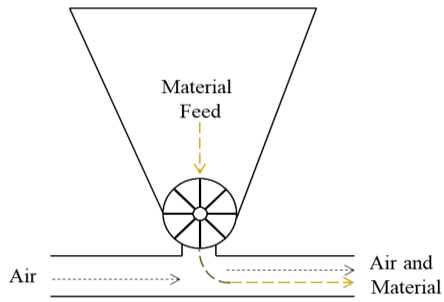

Figure 3.2. Rotary feeder

3.3.12. Cyclone separator

The Lapple model was commonly used due to its simplicity in design and construction. It efficiently determines separator dimensions and performance, taking into account factors such as particle size and air velocity to ensure effective material separation and optimization of system performance.

The cyclone used in this study was a non-commercial unit specifically fabricated for laboratory testing. Industrial-grade cyclones were typically made from durable materials such as stainless steel or coated carbon steel to ensure abrasion and corrosion resistance. However, for this study, the cyclone was constructed from high-density polyethylene a hard plastic material manufactured in the departmental workshop. The primary reasons for selecting plastic were cost efficiency, ease of fabrication, and suitability for small-scale laboratory applications. The calculations based on the Lapple model was presented in Table 3.1, and the corresponding separator design was illustrated in Figure 3.3.

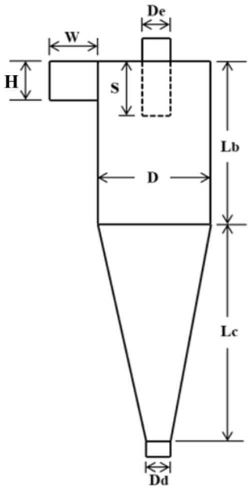

Figure 3.3. Cyclone separator

Table 3.1. Lapple model cyclone separator dimensions

Cyclone separator dimensions(mm)				
	Dimensions	Ratio	For inlet width (W)	
			D = 46mm	D = 71mm
Diameter of cyclone body (barrel)	D	4W	184	284
Length of the body	L_b	2D	368	568
Length of the cone	L_c	2D	368	568
Height of the inlet	H	D/2	92	142
Diameter of gas Exit	D_e	D/2	92	142
Diameter of the dust outlet	D_d	D/4	46	71
Length of the vortex finder	S	0.625D	115	178
Total length of the cyclone	L_b+L_c	4D	736	960

3.3.13. Minimum conveying velocity

Minimum conveying velocity, also known as the saltation velocity was the velocity at which particles begin to transition from a suspended state to a settling state, where it was intermittently lifted and then fall back into the flow. It was calculated using the particle mean diameter, solid loading ratio, and pipe diameter, based on the Rizk equation as shown in Equation 2.11.

The conveying velocity was set at 1.5 times the saltation velocity to maintain particle suspension and efficient transport (Xu et al., 2023). The maximum solid loading ratio in a pneumatic conveying system was the ratio of material to air mass flow rates was typically up to 15:1 for effective transport and stable flow, 2:1 to 5:1 was commonly used (Guzman et al., 2020).

3.4. Methods for investigation of pressure drop in the system

The pressure drop in the positive-pressure dilute-phase pneumatic conveying system was investigated using both experimental measurements and CFD-DPM simulations. In the experimental setup, pressure sensors were installed at key points along the pipeline to record the pressure drop under varying air velocities and material flow rates. Measurements were repeated in replicates to ensure accuracy and reproducibility. The experimental procedures followed established testing protocols to maintain consistency and reliability.

For the CFD-DPM simulations, the system geometry, boundary conditions, and material properties were defined based on the physical setup. Air was modeled as a continuous phase, and teff grains were modeled as discrete particles. The simulations provided detailed insights into flow patterns, particle trajectories, and local pressure variations, complementing the experimental data. Both approaches were used together to validate results and ensure that the measured pressure drops accurately reflected the real system.

3.4.1. Experimental design

A full factorial design was used to investigate the effects of air velocity, material flow rate, pipe diameter, and pipe length on the pressure drop of a pneumatic teff grain conveyor. Six Air velocities (12-28 m/s), twelve flow rates (0.009-0.28kg/s), selected flow rates of 0.009, 0.03, 0.044, 0.067, 0.08, and 0.1 kg/s were chosen to represent this practical operating range. Teff seeding typically requires 25-50 kg per hectare, corresponding to the lower flow range (0.009-0.044 kg/s), while small-scale local teff milling machines operate between 3-5 quintals per hour (0.083-0.139 kg/s), aligning with the upper range. These values were fixed to capture realistic field and processing conditions suitable for both experimental investigation and CFD-DPM simulation.

Three pipe diameters (46mm, 71mm, 102 mm) and five pipe lengths (2m, 3m, 4m, 5m, and 6m) were tested in various combinations through both laboratory experiments and CFD-DPM simulations. This design is expected to produce 3,150 data records, with 36.76% from experiments and 63.24% from CFD-DPM simulations, including bend layouts and factorial design for the cyclone separator. The summary of the factorial design for collected data across feeders, straight pipes, and bends was shown in Table 3.2.

Table 3.2. Summarized factorial design

Independent variables					
D [46mm], L[2m, 4m, 6m]		D [71mm], L[2m, 3m, 4m, 5m,6m]		D[102mm], L[2m,3m, 4m,5m, 6m]	
m_s(kg/s)	v(m/s)	m_s(kg/s)	v(m/s)	m_s(kg/s)	v(m/s)
0.009	12, 16, 18, 22, 25,28	0.009	12, 16, 18, 22, 25,28	0.009	12, 16, 18, 22, 25,28
0.03	12, 16, 18, 22, 25,28	0.03	12, 16, 18, 22, 25,28	0.03	12, 16, 18, 22, 25,28
0.044	12, 16, 18, 22, 25,28	0.044	12, 16, 18, 22, 25,28	0.044	12, 16, 18, 22, 25,28
0.067	18, 22, 25,28	0.067	12, 16, 18, 22, 25,28	0.067	12, 16, 18, 22, 25,28
0.084	22, 25,28	0.084	12, 16, 18, 22, 25,28	0.084	12, 16, 18, 22, 25,28
0.1	25,28	0.1	12, 16, 18, 22, 25,28	0.1	12, 16, 18, 22, 25,28
		0.13	18,22,25, 28	0.13	12, 16, 18, 22, 25,28
		0.16	18,22,25, 28	0.16	12, 16, 18, 22, 25,28
		0.19	22, 25, 28	0.19	12, 16, 18, 22, 25,28
		0.22	25, 28	0.22	12, 16, 18, 22, 25,28
		0.25	28	0.25	16,18,22,25,28
				0.28	16,18,22,25,28

Laboratory test (grey) | CFD-DPM Simulation (blue)

3.4.2. Sample preparation

Three teff grain varieties, Felagot (DZ-Cr-442 RIL77C), Bishoftu (DZ-Cr-497 RIL133), and Boni (DZ-Cr-498 RIL37) were selected for laboratory testing based on their mean grain diameters, representing small, medium, and large sizes, respectively. Felagot, d_p = 0.67 mm; Boni, d_p = 0.70; and Bishoftu, d_p =0.72 mm. The samples were sourced from DZARC and stored at room temperature without any additional drying or wetting to maintain consistency in their physical properties, and selected varieties were mixed to incorporate the variability between varieties.

In pneumatic conveying, controlling relative humidity was essential to prevent material clumping, blockages, and quality degradation, particularly for moisture-sensitive grains. In this study, relative humidity was not actively controlled, and experiments were conducted under ambient laboratory conditions, which represent typical handling environments.

3.4.3. Experimental setup

Selected pipe size and blower, designed rotary feeder, and cyclone separator were manufactured and constructed. Installed the blower connected to the power source. The blower outlet was connected to the feeder inlet, the feeder outlet was connected to pipelines, and the cyclone separator was installed at the end of the pipeline to separate air and teff grain. As shown in Figure 3.4 (a), CZT-4 Blower; Figure 3.4 (b) 50 mm and 75 mm pipelines, Figure 3.4 (c) 90° bend, and Figure 3.4 (d) cyclone separator with 150 mm, 180 mm, and 200 mm cyclone separators. The system was configured in a closed-loop setup to facilitate multiple measurements with the optimum amount of teff grain.

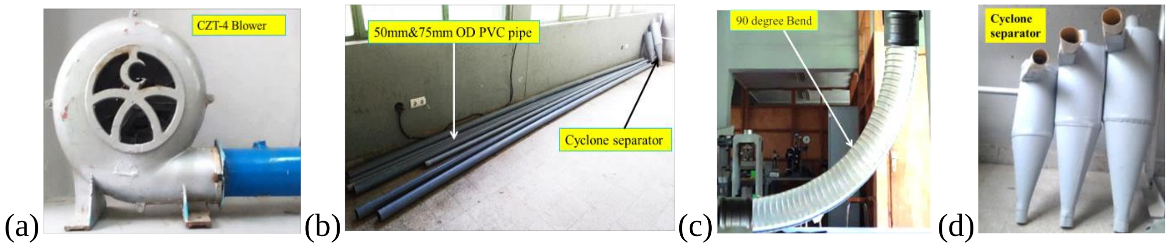

Figure 3.4. Major components in the system

Pressure drop data were recorded using an MA-45 digital manometer connected via hoses and connectors to measure at points P_1 (point one) and P_2 (point two). The pressure drop was calculated as the difference in pressure between these two points.

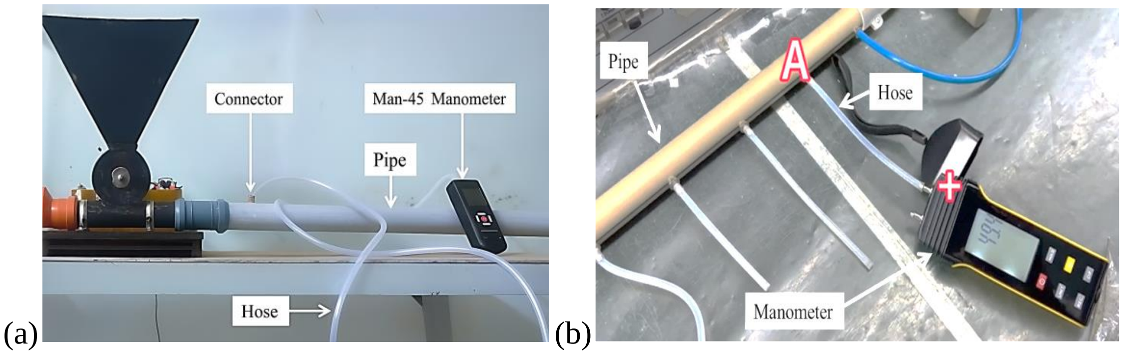

Figure 3.5. Set-up for pressure drop measurement

Figure 3.5 shows the setup for pressure drop measurement: (a) Man-45 digital manometer installation procedure and (b) digital manometer installation procedure (Holdpeak et al., 2023).

To ensure continuous and precise feeding of the system, the feeding mechanism was designed to maintain a steady and controlled material supply. It incorporated a DC motor speed controller operating within a voltage range of 5V to 28V, enabling precise speed adjustments. Additionally, a gear motor with a rated voltage of 24V DC and a rated speed of 120 RPM drove the feeding mechanism, allowing for effective regulation of the material flow rate. The construction and assembly of the feeding system were illustrated in Figure 3.6.

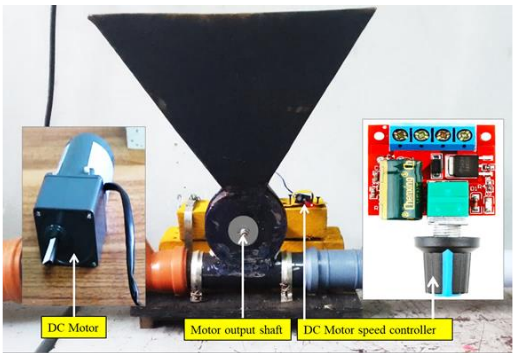

Figure 3.6. Feeding system

3.4.4. Flow rate measurement

Air velocity at the system inlet was recorded using a GM-816 professional digital anemometer. The device captured the airflow velocity with precision, providing essential data for analyzing the pneumatic conveying system performance as illustrated in Figure 3.7.

(a) 

(b) 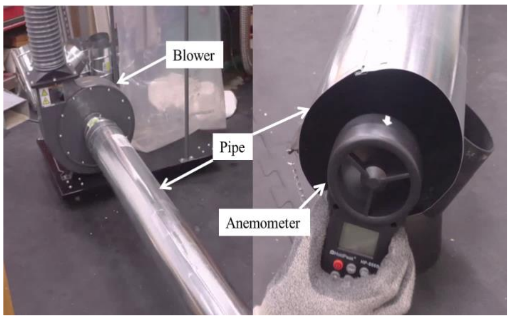

Figure 3.7. Inlet air velocity measuring setup

Figure 3.7 shows the inlet air velocity measuring setup (a), the Inlet air velocity measurement setup using GM-816 digital anemometer (b), measuring airflow rate, air velocity, and installation procedure (Glenn & Frazee, 2021).

3.4.5. Experimental setup for feeder

The pressure drop across the feeder in a pneumatic conveying system was a critical parameter that influences the overall efficiency and performance of the system. In this context, the feeder introduces teff grain into the conveying line, and its design, operating conditions, and interaction with airflow play a significant role in determining the pressure drops.

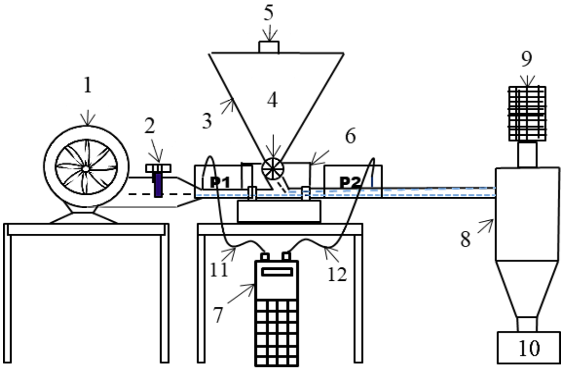

Figure 3.8. Experimental setup for measurement of pressure drop due to feeder

An experimental setup was developed, consisting of the following components: (1) a blower, (2) a valve to control the airflow, (3) a hopper to store teff grain, (4) a rotary feeder to feed the grain, (5) a material inlet, (6) a speed controller to adjust the flow rate, (7) a digital manometer to measure the pressure drop across the feeder, (8) a cyclone separator to separate the grain, (9) an air filter to filter the air, (10) a collector to collect the material, and (11 and 12) flexible hoses to connect the system to a manometer for pressure measurements. This setup enables the analysis of feeder-induced pressure losses, as shown in Figure 3.8.

3.4.6. Experimental setup for cyclone separator

In a positive-pressure dilute-phase pneumatic conveying system, the cyclone separator uses swirling air to separate teff grain from the air stream, with denser particles falling to the bottom and clean air exiting the top. This process causes a pressure drop, measured using a Man-45 digital manometer at the cyclone's inlet and outlet, indicating energy losses from airflow resistance and particle separation.

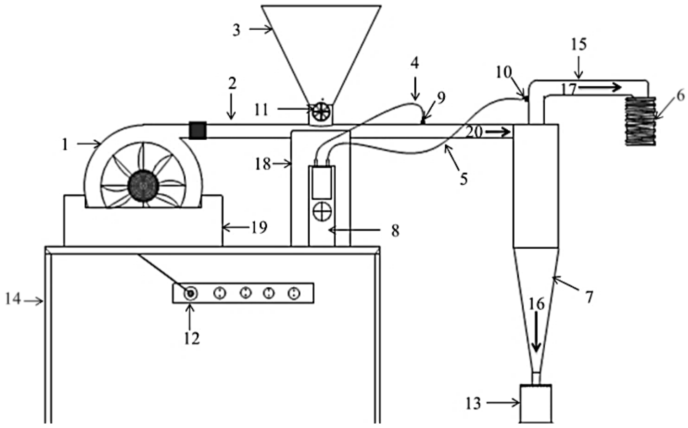

Figure 3.9. Experimental setup for measurement of pressure drop due to CS

In the positive-pressure dilute-phase pneumatic conveying system, the setup consists of the following components: (1) a blower to initiate airflow, (2) pipes to transport a mixture of air and teff grain, (3) a hopper to store the grain, (4) and (5) hoses, (9) and (10) connector to connect measuring instrument to pipe, (6) a dust collector to capture fine particles, (16) grain collector, (7) a cyclone separator that uses swirling air to separate particles, (8) a digital manometer to measure pressure loss at the inlet and outlet, (11) a rotary feeder to control material feed, (12) a power source to drive the system, (13) a container to collect teff grains, (15) an outlet pipe for air discharge, and (17) clean air. The setup is supported by structural elements (14), (18), and (19), which ensure system stability and precise pressure measurements. This arrangement provides insights into energy losses and separation efficiency, as highlighted in Figure 3.9.

3.4.7. Experimental setup for horizontal pipe

Measuring the pressure drop across the horizontal pipeline in a pneumatic conveying system for teff grain was key to understanding system performance. A Man-45 digital manometer was used to record pressure drop between a 2m pipe length, a source of data for numerical validation, modeling, and performance evaluation.

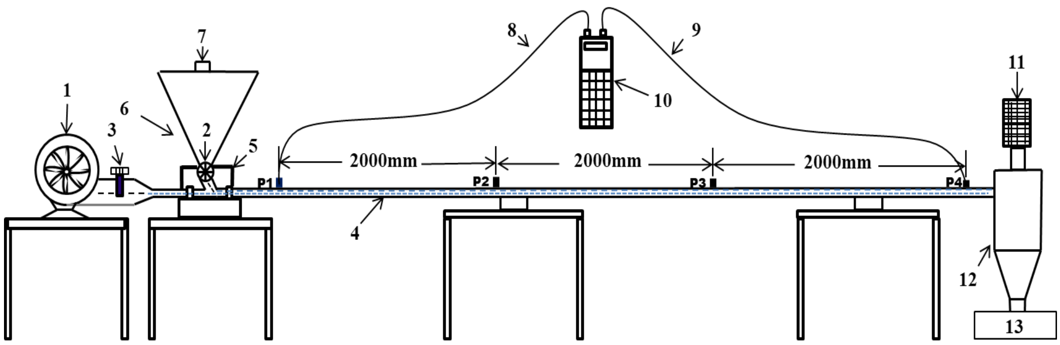

Figure 3.10. Experimental setup for measurement of pressure drop due to HP

Pressure drop across the horizontal pipeline was crucial for evaluating the performance and efficiency of a pneumatic conveying system for teff grain. The system includes the following components: (1) a blower, (2) a rotary feeder, (3) an airflow control valve, (4) a pipeline, (5) a material flow control device, (6) hopper, (7) material inlet, (8) and (9) hoses connected to (10) a Man-45 manometer to measure the pressure drop across pipeline section, (11) an air filter to clean the air, (12) a cyclone separator to separate the grain, and (13) a material collector to collect the separate air and teff grain. Pressure measurement points (P1, P2, P3, and P4) were used to determine the pressure drop, as shown in Figure 3.10.

3.4.8. Experimental setup for vertical pipe and 90^{o} bends

In a positive-pressure dilute-phase pneumatic conveying system, the pressure drop in the vertical pipeline results from airflow resistance and gravity, as additional force was needed to lift the grain. A Man-45 digital manometer was installed at various points to measure pressure variation. Pressure loss was a key to system performance and design optimization. Bends in the pipeline introduce further resistance, causing turbulence and particle collisions, which increase the pressure drop. To quantify this, a Man-45 manometer measured the pressure drop at the bend's inlet and outlet, with the difference indicating energy loss.

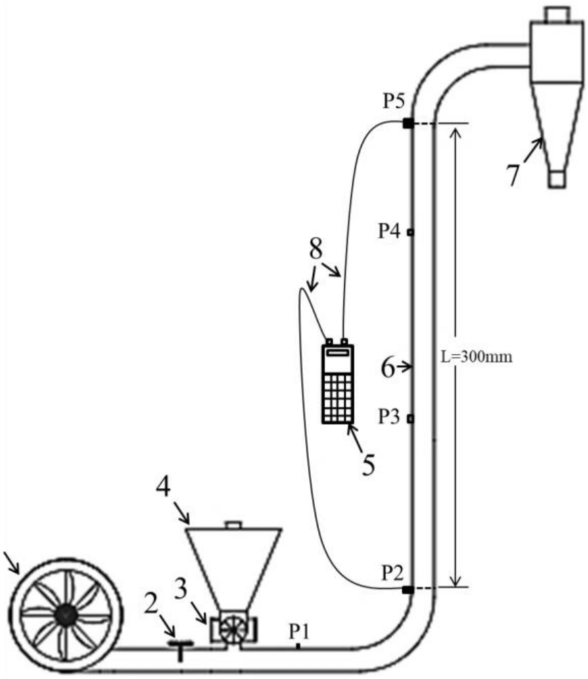

Figure 3.11. Set up for measurement of pressure drop due to VP and bends

In a positive-pressure dilute-phase pneumatic conveying system, pressure drops in vertical pipelines and bends were key to evaluating performance. The system includes (1) a blower for airflow, regulated by (2) an airflow control valve, and (4) a hopper for grain introduction, with flow controlled by (3) a material flow controller or rotary feeder. Vertical pipelines require extra pressure to lift grains, increasing the pressure drop, measured by (5) a digital manometer between various vertical points: P2, P3, P4, and P5. Bends, especially 90° elbows, add resistance due to turbulence and collisions, with pressure drops measured between inlet and outlet points: P1, P2. (6) A vertical pipe, (7) a cyclone separator, and (8) flexible hoses were also part of the system, as illustrated in Figure 3.11.

3.4.9. Experimental setup for full system

To evaluate the overall performance of the pneumatic conveying system, it was essential to determine the total pipeline length and corresponding pressure losses across all major components. This includes the straight sections and the equivalent lengths of bends, which directly affect system design and energy efficiency. A detailed illustration of the complete laboratory set-up used for the experimental investigation was shown in APPENDIX A.

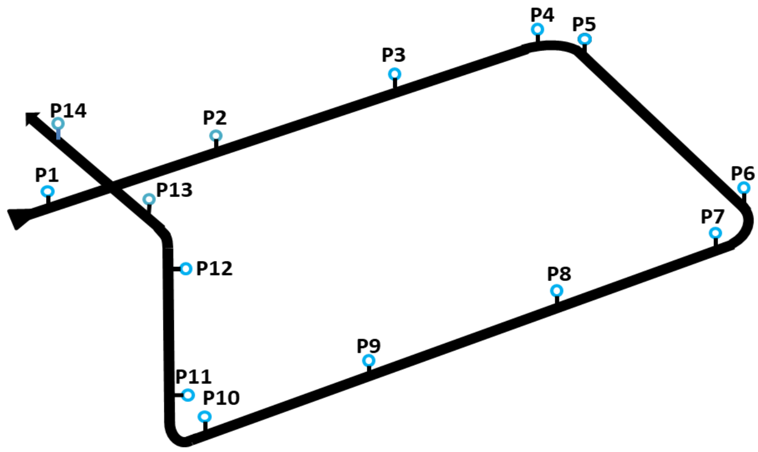

Figure 3.12. The profile of pneumatic teff grain conveying system

The total pipeline length in the pneumatic conveying system was calculated by summing the horizontal pipeline, 18 m, the vertical pipeline, 3 m, and the equivalent lengths of four 90° bends, 1.73 m or 2.67 m. This gives total lengths of 22.73 m (18 + 3 + 1.73) and 23.67 m (18 + 3 + 2.67). The system configuration includes pipe lengths; L of 22.73 m and 23.67 m, internal bores; D of 46 mm and 71 mm, and four 90° bends with an R/D ratio of 6. Pressure transducers at (P1-P14) monitor pressure variation, with total pressure accounting for drops across key components like the feeder, straight pipes, bends, and cyclone separator, as shown in Figure 3.12.

3.4.10. Pressure drop measuring procedure

The experimental procedure was designed to evaluate pressure drops across key components of a positive-pressure, dilute-phase pneumatic conveying system transporting teff grain. The components under investigation included the feeder, horizontal pipe, vertical pipe, 90° bends, and cyclone separator.

Step 1: Assemble the pneumatic conveying system, integrating the blower, rotary feeder, pipes, bends, and separator. Step 2: Calibrate the airflow and material transport conditions. Step 3: Adjust air velocity at the blower outlet using the airflow control valve. Step 4:

Introduce teff grain using a rotary feeder. Step 5: Measure pressure drops across a section of the system using a MAN-45 digital manometer and repeat measurements with three replications. Step 6: Add pressure drops across all sections to determine the total pressure drop in the full system.

3.4.11. Energy requirement calculations

The power loss (Watts) in the pneumatic conveying system was calculated as the product of the total pressure drop (ΔP) in the system and the air mass flow rate (Q, m^3/s), as shown in Equation 2.24. The energy required for pneumatic conveying accounts for the pressure drop across the system as well as blower losses, multiplied by the air flow rate (Q), which reflects inefficiencies in blower performance. The efficiency of the blower (η) was a key factor in determining the actual energy input required, with typical values ranging from 50% to 85% depending on blower type and operating conditions. The actual power needed P_{input} to drive the blower and ensure efficient material transport can be estimated using Equation 2.25.

3.4.12. CFD-DPM Simulation

CFD-DPM simulation was a crucial tool used to model the behavior of the teff grain (discrete phase) and air (fluid phase) in the pneumatic conveying system, providing a detailed analysis of how both phases interact within the system. It helps evaluate key factors such as velocity distribution, pressure drop, and particle concentration across various system components.

CFD-DPM offers valuable insights into the behavior of teff grain as it moves through the system, including how it interacts with airflow and pipe walls. It serves as a complementary tool to experimental methods, allowing for deeper analysis of complex flow patterns and particle dynamics that may be difficult to capture in physical experiments.

3.4.13. Simulation setup

CFD simulation: utilized to model the flow behavior of teff grain within the pneumatic conveyor system, allowing for detailed visualization and analysis of the interactions between the gas phase and solid particles. This method offers valuable insights into the influence of key parameters such as pressure drop and particle velocity distribution on the overall efficiency and performance of the conveying process.

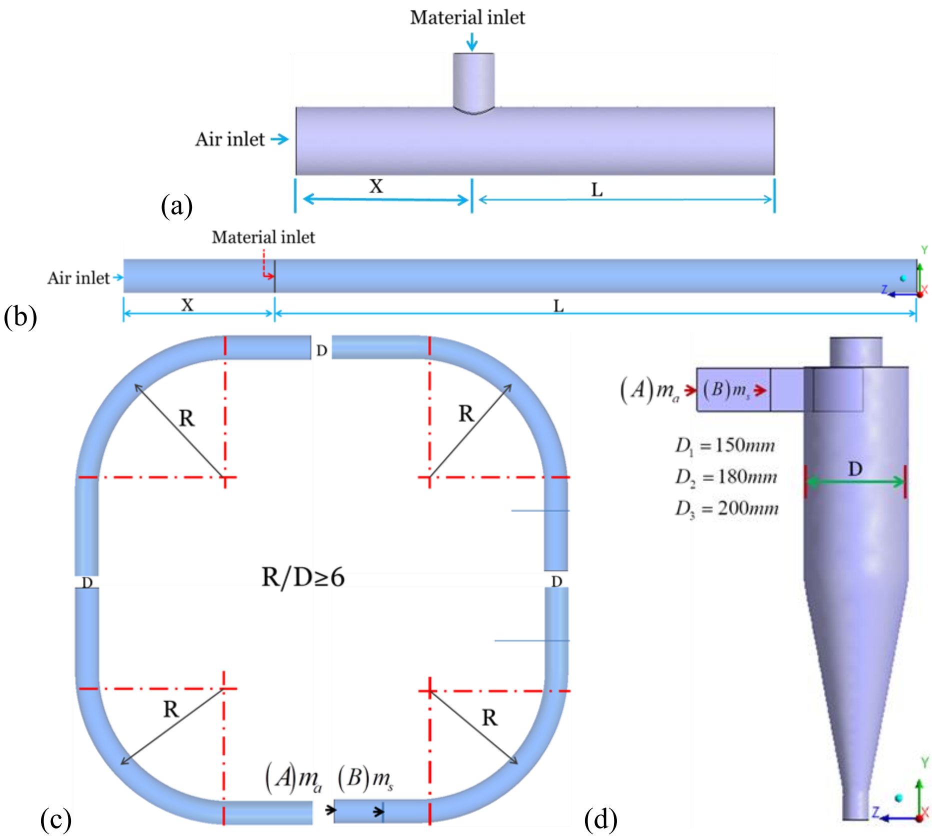

Figure 3.13. CFD-DPM simulation setup

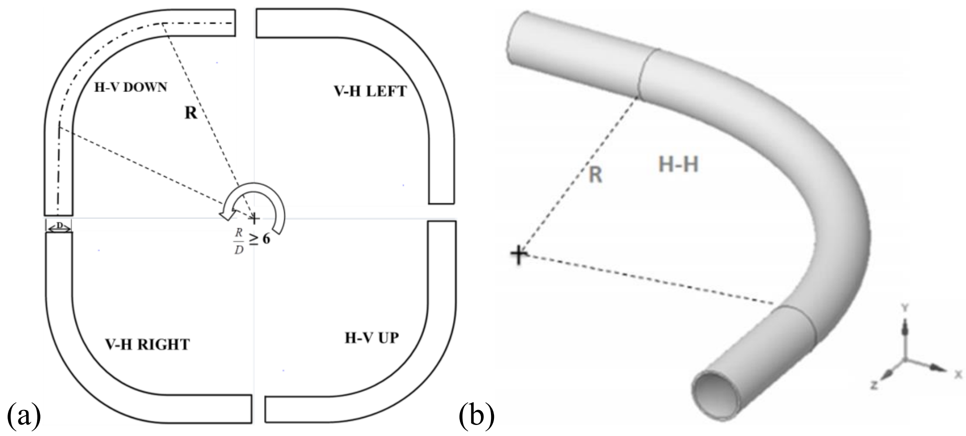

Figure 3.14. Geometry of different bend layouts

As shown in Figure 3.14, was CFD-DPM simulation set-up for (a)feeder (b) straight pipe, X= distance between the air inlet and material inlet, or L = pipe length (c) bends, R = bend radius (d) cyclone separator A (m_a) air inlet and B (m_s) material inlet and Figure 3.14 (a) H = horizontal, V = vertical, UP, DOWN, RIGHT and LEFT were indicated a connection between straight pipes when the direction of flow was counter-clockwise and Figure 3.14 (b) indicate bend join horizontal and horizontal pipelines.

CFD-DPM simulation setup includes material properties, air properties, pipe size and geometry, boundary conditions, operating conditions, solution method, run calculation, convergence criteria, report generation, and post-processing using CFD-Post**.**

Geometry modeling: the geometry of the pneumatic conveying system was developed using ANSYS SpaceClaim 2024R1. The modeled components include a feeder, horizontal and vertical pipes, 90° bends, and a cyclone separator. A hexahedral mesh was applied to the horizontal and vertical pipes, while a tetrahedral mesh was used for the feeder, bends, and cyclone separator. The pipe diameters used in the system were 46 mm, 71 mm, and 102mm, with corresponding pipe lengths of 2 m, 3 m, 4 m, 5 m, and 6 m. Cyclone separator diameters were varied to 150 mm, 180 mm, and 200 mm. The bend radius to pipe diameter ratio (R/D) was maintained at 6.

Particle properties: the teff grain was used as the solid phase material. The particle size distribution was modeled using the Rosin-Rammler function with a mean diameter of 70×10^{4} m, ranging from 68×10^{4} m to 72×10^{4} m. A non-spherical particle model was adopted, with sphericity values of 0.67 to 0.69. The true density of teff grain ranged from 1120 kg/m^3 to 1381 kg/m^3. Simulations were conducted across a wide range of mass flow rates from 0.009 kg/s to 0.28 kg/s.

Fluid properties: air was the carrier fluid in the system. It was characterized by a density of 1.225 kg/m^3 and a viscosity of 1.7894×10^{5} kg/m·s. Air inlet velocities considered in the simulation were 12 m/s, 16 m/s, 18 m/s, 22 m/s, 25 m/s, and 28 m/s.

Mesh generation: for CFD-DPM simulations, the mesh size was selected to be within 4 to 10 times the mean particle diameter, which resulted in mesh sizes ranging from 2.72 mm to 6.8 mm.

Operating conditions: the gravitational acceleration was set to -9.81m/s^2 along the y-axis, consistent with physical orientation in the simulation.

Discrete Phase Model: A two-way coupling approach was employed, allowing interaction between solid particles and the continuous fluid flow. In CFD-DPM simulation, turbulence model used: standard k-ε model was applied to the horizontal and vertical pipes, while the k-ε RNG model was used for the feeder, bends, and cyclone separator, ensuring accurate turbulence representation across varying geometries.

Boundary conditions: two separate inlets were defined: one for continuous airflow and another for solid material injection. Air was introduced through Inlet 1 with velocities ranging from 12m/s to 28m/s along the Z-axis. Inlet 2 was used for teff grain injection at the specified mass flow rates from 0.009 kg/s to 0.28 kg/s. The outlet surface allowed for the escape of both air and solid particles, with the outlet pressure set to 0 Pa. The wall boundary condition was set as solid (reflective) with a no-slip condition.

Solution method: the simple (semi-implicit method for pressure equations) algorithm was employed for pressure-velocity coupling. Discretization schemes included second-order accuracy for pressure, momentum, turbulence kinetic energy, turbulence dissipation rate, and discrete phase equations.

Run calculation: simulations were run for 500 to 1000 iterations. Both the reporting interval and profile update interval were set to 1 for detailed monitoring of the solution.

Convergence criteria: The convergence criteria for residuals were set as follows: continuity $< 1 \times 10^{-3}$, velocities $< 1 \times 10^{-6}$, and turbulence quantities $< 1 \times 10^{-6}$.

Report file: post-processing involved extracting and reporting area-weighted average values for key parameters, including static pressure, air velocity, turbulence kinetic energy, particle residence time, and particle mass concentration.

CFD-Post: the results from ANSYS Fluent were further analyzed in CFD-Post, with detailed output including pressure and velocity distributions, particle mass concentration, and particle residence time.

3.4.14. Verification and validation of CFD-DPM simulations

CFD-DPM simulation validation was essential for ensuring the accuracy and reliability of results and was achieved through methods like grid dependence, sensitivity analysis, wall function considerations, and convergence testing. Grid dependence assesses the impact of mesh resolution on results, ensuring sufficient grid refinement. Sensitivity analysis evaluates how input parameter variations affect outcomes, confirming model reliability under varying conditions.

Wall functions help model near-wall flow dynamics, crucial in high-speed flows where fine grid resolution may not capture boundary layer behavior. Finally, convergence testing ensures the solution stabilizes by monitoring scaled residuals, confirming that further iterations will yield negligible changes, and validating the simulation's accuracy. These methods collectively ensure the robustness of CFD-DPM simulations for pneumatic conveying systems.

3.4.15. Grid dependence of CFD-DPM

Grid dependence in DPM refers to how simulation results, such as particle trajectories and flow interactions, vary with grid size and resolution. Coarse grids may lead to inaccuracies, while finer grids improve accuracy but increase computational cost. For reliable results, the mesh size should ideally be 4 to 10 times the particle mean diameter to accurately capture particle-fluid interactions. A grid independence study, involving progressively finer grids until results stabilize, ensures accuracy and eliminates numerical artifacts. Balancing grid resolution with computational efficiency was crucial for dependable DPM simulations (Z. Zhao et al., 2024).

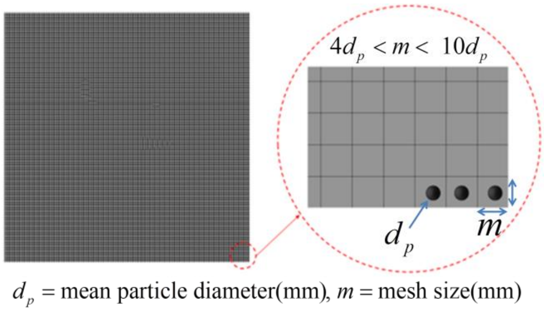

Figure 3.15. Grid size independence for discrete phase model

3.4.16. Sensitivity analysis

Sensitivity analysis was carried out on several parameters, such as mesh size, pipeline layout, gas properties, conveying material characteristics, and boundary conditions. This analysis's goals were to verify the CFD-DPM simulation and investigate how small adjustments to these variables affected the teff grain's pneumatic conveying properties. The results show that small modifications in the independent variables can cause noticeable alterations in the pneumatic conveying system's behavior, especially when it comes to determining pressure drop. The findings demonstrate that the pressure drop was extremely sensitive to changes in the parameters and that any modification to the input variables significantly affects the simulation's results.

3.4.17. Wall function

Wall functions serve as a key criterion for validating CFD-DPM simulations; it was specifically calibrated to approximate the log-law region, which corresponds to $30 < y+ < 300$. Ensuring that y+ values fall within this range was essential for accurate modeling of near-wall turbulence in CFD-DPM simulations (Salim & Cheah, 2009).

3.4.18. Convergence criteria

In CFD-DPM simulations, convergence was determined by the behavior of scaled residuals, which represent the balance between sources and sink terms in the governing equations. As the simulation progresses, residuals decrease, and when it was reach values close to zero (typically < 1E-5 to 1E-6), the solution was considered converged. This indicates that further iterations would yield negligible changes, ensuring stable and reliable results. Monitoring residuals was essential for verifying solution accuracy and avoiding issues like instability or inadequate convergence (Singh et al., 2023).

3.4.19. Comparative analysis of CFD-DPM simulation and experimental results

A comparative analysis between CFD-PM and experimental results can be performed for each pneumatic conveying system component, including the feeder, pipes, bends, and cyclone separator, using metrics like (r) Correlation Coefficient, R^2 (Coefficient of Determination), MAE (Mean Absolute Error), MSE (Mean Squared Error), RMSE (Root Mean Square Error), Relative MAE, Relative MSE, Relative RMSE, and MAPE (Mean Absolute Percentage Error). r and R^2 indicate model fit, MSE, MAE, and RMSE quantify error magnitude, MAPE assesses percentage errors, and Relative MSE, Relative MAE, and Relative RMSE evaluate overall model accuracy relative to the mean (baseline). All metrics provide a comprehensive comparison of model accuracy and reliability for system components.

3.5. Methods for artificial neural network model

ANNs was powerful machine learning tools within the field of artificial intelligence (AI), capable of modeling complex, nonlinear relationships in large datasets. Inspired by the structure and function of the human brain, ANNs mimic the way the human mind processes information through layers of interconnected neurons that learn patterns from experience. This makes them particularly well-suited for capturing intricate variable interactions and adaptive learning in engineering systems.

In this study, ANNs were employed to model and predict pressure drop in a positive-pressure dilute-phase pneumatic conveying system for teff grain. Pressure drop was a critical performance parameter influenced by multiple interacting factors such as air velocity, pipe geometry, grain characteristics, and material flow rate. Traditional regression methods often struggle to accurately represent such nonlinear behavior, whereas ANNs offer greater accuracy and flexibility.

MATLAB R2019a, utilizing its nntool, was used to design, train, and validate the ANN models. The developed network learned from both experimental and CFD-DPM simulation data to predict pressure drop across a range of operating conditions. This modeling approach supports the optimization of system efficiency, enhances predictive reliability, and reduces the need for extensive physical experimentation in pneumatic conveying design.

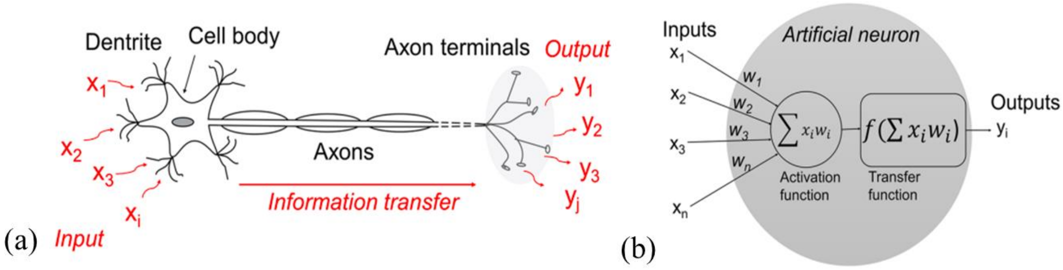

Figure 3.16. Representation of neuron (a) human neuron and (b) single artificial neuron (Atzeni et al., 2021)

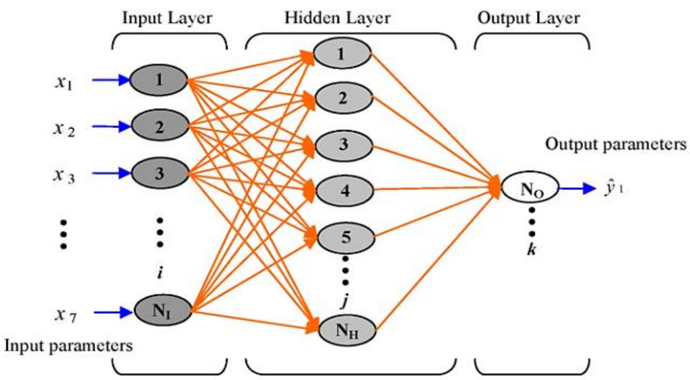

Figure 3.17. Architecture of feed-forward ANN model with a single hidden layer (Zhao & Su, 2010)

3.5.1. Data preparation

The ANN model was developed using data from laboratory tests and CFD-DPM simulations, each offering unique insights into the pneumatic conveying system. These datasets were combined, prepared, and structured for training, validation, and testing. Laboratory tests, limited by factors like scale and cost, complement the detailed insights from CFD-DPM simulations, which provide a comprehensive view of airflow and particle behavior. A regression analysis quantifies the relationship between the two datasets, using metrics like R^2, MAE, and RMSE to evaluate model fit. After handling outliers, the combined data was structured for the ANN model, offering a robust predictive model for pressure drop in key system components such as the feeder, pipes, bends, and cyclone separator. The combined input and independent variables were detailed in Table 3.3. A detailed description of a significant level of the independent variable on the dependent variable was illustrated in APPENDIX C.

Table 3.3. Summary of independent and dependent variables

Component	Independent variables	Dependent variable
Feeder	v (m/s), m_s (kg/s), D (m)	ΔP (Pa)
Horizontal Pipe	v (m/s), m_s (kg/s), D (m), L (m)	ΔP (Pa)
Vertical Pipe	v (m/s), m_s (kg/s), D (m), L (m)	ΔP (Pa)
Bends	v (m/s), m_s (kg/s), D (m)	ΔP (Pa)
Cyclone Separator	v (m/s), m_s (kg/s), D (m)	ΔP (Pa)

3.5.2. Determining number of neurons

In an ANN model, it is crucial to have a larger dataset to mitigate overfitting, particularly in complex models. The 50 times weight rule, based on empirical analyses of synthetic and real data, emphasizes the complexity of the data-generating process. On the other hand, the 10 times rule, a more widely referenced guideline in the ANN community, suggests using at least ten times the number of weights (Alwosheel et al., 2018).

According to Alwosheel et al. (2018), for an ANN with 3 inputs, 10 hidden neurons, and 1 output, the total parameters (weights + biases) were 51, requiring a minimum of 510 data points. For 4 inputs, the total becomes 61, needing at least 610 data points; based on the rule that data size should be 10× the number of parameters.

During training, the ANN iteratively adjusts weights using backpropagation and gradient descent to minimize prediction error, updating weights based on the error gradient until acceptable accuracy was achieved (Leema et al., 2020; He, 2021).

3.5.3. Data splitting strategy

A common 70/15/15 split for training, validation, and testing in MATLAB offers a balanced approach for learning, monitoring, and unbiased evaluation. MATLAB's default of 10 hidden neurons provides a good starting point, helping avoid overfitting or underfitting.

3.5.4. ANN training algorithm

Training an ANN in MATLAB involves splitting data into training, validation, and test sets and then defining the network architecture. For a feed-forward network, the hidden layer uses 10 neurons with a tan-sig activation function, while the output layer uses a linear activation function for regression. The Levenberg-Marquardt algorithm was chosen for its fast convergence and accuracy, especially for medium-sized datasets, outperforming alternatives like Bayesian regularization and scaled conjugate gradient.

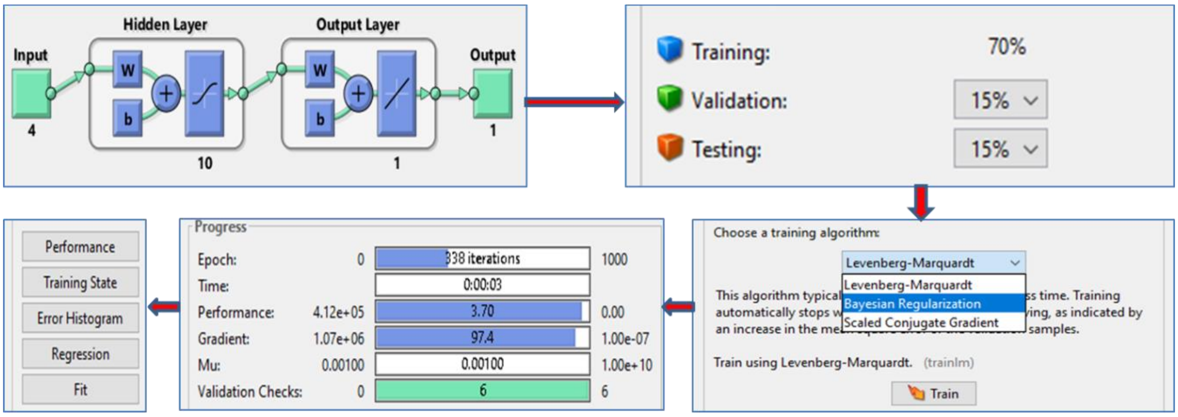

Figure 3.18. ANN training process diagram MATLAB 2019Ra

3.5.5. K-Fold cross-validation

To perform K-Fold cross-validation for the ANN model, split the dataset into K equally-sized folds. In each iteration, use K-1 folds for training and the remaining fold for testing. This process was repeated K times, with each fold serving as the validation set once. Common values for K were 5 or 10, depending on the dataset size. After completing all iterations, average the performance metrics to estimate the model's ability to generalize. K-fold cross-validation reduces bias, mitigates overfitting, and provides a robust performance estimate. It was used to optimize the number of neurons and the data splitting size, ensuring effective model tuning, particularly for datasets like teff grain in pneumatic conveying systems.

3.5.6. ANN model performance evaluation metrics

To evaluate the performance of an ANN model, regression evaluation metrics were used to assess model accuracy. Key metrics were classified into four categories (Correlation Goodness-of-fit, Error magnitude, and percentage error): Correlation: r (pearson correlation coefficient), which measures the strength and direction of the linear relationship between actual and predicted values. Goodness-of-fit: R^2 (coefficient of determination) indicates how well the model captures variance in the observed data. Error magnitude: MAE (mean absolute error), MSE (mean squared error), and RMSE (root mean squared error) measure the absolute size of prediction errors. Lower values indicate better performance.

Error relative to mean: Relative MSE, Relative RMSE, Relative MAE Normalizes error magnitude by dividing it by the mean of actual values. Percentage error: MAPE (mean absolute percentage error) measures average absolute error as a percentage of actual values, useful for interpretability. Expression and guidelines for all metrics were summarized in Table 3.4. Together, these metrics provide a comprehensive comparison of model accuracy and reliability across system components to overcome overfitting or underfitting of the model.

Table 3.4. ANN performance evaluation metrics

Metrics	Description	Formula	Interpretation
r	Describes the strength and direction of the relationship between two variables	$r = \frac{\Sigma(x_i - \hat{x})(y_i - \hat{y})}{\sqrt{\Sigma(x_i - \hat{x})^2 \Sigma(y_i - \hat{y}\ )^2}}$	Values close to ±1 indicate a strong relationship, and near 0 weak or no relationship (Akoglu, 2018).
R^2	Measures how well independent variables explain the variation in the dependent	$R^2 = 1 - \frac{SSR}{TSS}$	Ranges from 0 to 1: values > 0.9 indicate excellent fit, 0.7 - 0.9 good, 0.5 - 0.7 fair, 0.3-0.5 weak, < 0.3 poor fit (Hange et al., 2020).

Metrics	Description	Formula	Interpretation
	variable		
MAE	Measures the average magnitude of errors without considering direction	$MAE = \frac{1}{n}\sum_{i=1}^{n} \lvert y_i - \hat{y}_i \rvert$	MAE < 10 indicates very high accuracy, 10-20 suggests high accuracy, 50-100 indicates moderate accuracy, and 200+ signals high inaccuracy (Jierula et al., 2021).
MSE	Measures the average squared difference between predicted and actual values	$MSE = \frac{1}{n}\sum_{i=1}^{n} (y_i - \hat{y}_i)^2$	Lower values indicate better accuracy. Values between 100- 4000 are low, 4000-10,000 moderate, > 40,000 high error (Jierula et al., 2021).
RMSE	The square root of MSE provides a more interpretable measure in the same units as the dependent variable.	$RMSE = \sqrt{\frac{1}{n}\sum_{i=1}^{n} (y_i - \hat{y}_i)^2}$	Lower values indicate better accuracy. Values 10 - 50 are low, 50 - 100 moderate, and> 200 high error (Uyeh et al., 2022).
Relative MAE	Measures the model's performance relative to a baseline model (mean of actual values).	$\text{Relative } MAE = \frac{MAE}{\bar{y}}$	Values < 1 indicate better performance than the baseline, 1 indicates equal, and >1 indicates worse performance (Chicco et al., 2021).

Metrics	Description	Formula	Interpretation
Relative MSE	Measures the model's performance relative to a baseline by comparing MSE values	$\text{Relative } MSE = \frac{MSE}{\bar{y}}$	Values < 0.04 indicate low error, 0.05 - 0.1 moderate, > 0.1 significant errors (Chicco et al., 2021).
Relative RMSE	Compares the RMSE of the model to the baseline model	$\text{Relative } RMSE = \frac{RMSE}{\bar{y}}$	Values < 0.6 indicate low error, 0.6-1.0 moderate, and > 1.0 high error (Chicco et al., 2021).
MAPE	Measures accuracy by calculating the average of absolute percentage errors	$MAPE = \frac{1}{n}\sum_{i=1}^{n}\left\lvert\frac{y_i - \hat{y}_i}{y_i}\right\rvert \times 100$	MAPE < 10% indicates excellent accuracy, 10% ≤ MAPE < 20% is good, 20% ≤MAPE < 50% is acceptable, and MAPE≥ 50% signals poor performance needing improvement (Jierula et al., 2021).

This evaluation was essential for rigorously assessing the performance of the ANN model, as it captures various dimensions of prediction quality, including accuracy, consistency, and error behavior. By examining how well the model learns from data and generalizes to new inputs, the evaluation provides a clear understanding of its reliability and effectiveness. It also helps identify potential areas for improvement, ensuring the model was both robust and applicable in practical scenarios. Overall, this process strengthens the validity of the model and supports its use in real-world applications.

3.5.7. Simulation of ANN models in MATLAB Simulink

To simulate the artificial neural network model in MATLAB Simulink, the trained network, developed using MATLAB's neural network toolbox, was first exported into the Simulink environment. This conversion transforms the ANN into a modular, functional block that can be seamlessly integrated into larger system-level models. The ANN block processes input data relevant to the pneumatic conveying system, typically including key operational and physical parameters such as air velocity (m/s), material flow rate (kg/s), pipe diameter (m), cyclone separator diameter (m), and pipe length (m). By feeding these variables into the ANN block, Simulink facilitates the prediction of pressure drop (Pa) across various components of the system, as illustrated in Figure 3.19. (a) Neural network diagram, (b) Data input interface, and (c) Simulink block diagram for simulation.

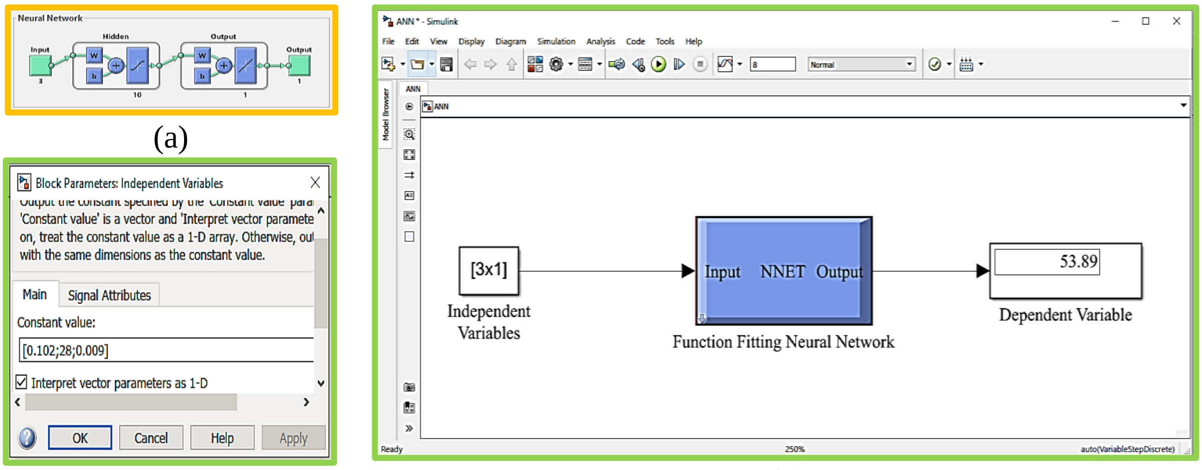

(b) (c)

Figure 3.19. Simulation of ANN models in MATLAB Simulink

This integration enables users to observe how variations in system conditions influence pressure drop behavior without the need for labor-intensive experimental trials or computationally expensive numerical simulations. Such flexibility was crucial for conducting parameter sensitivity analyses, optimizing system performance, and enhancing the overall accuracy and responsiveness of the predictive model.

CHAPTER FOUR

RESULTS AND DISCUSSIONS

4.1. Results and discussions on determination of engineering properties of teff grain

4.1.1. Physical properties of teff grain

The physical properties of teff grain were analyzed using scanning electron microscopy SEM, with representative images presented at X30, X60, and X270 magnifications in Figure 4.1 (a-c). Precise dimensional measurements revealed significant variation in grain size, with lengths ranging from 539 µm to 1.1 mm and intermediate measurements of 621 µm, 681 µm, 733 µm, 864 µm, 936 µm, and 1 mm. Angular measurements further demonstrated substantial variation, ranging from 13° to 76°. This considerable diversity in physical characteristics has important implications for pneumatic conveying systems. The variation in grain dimensions and shapes directly affects aerodynamic behavior, influencing critical parameters such as drag coefficients, suspension velocity, and particle-wall friction. These factors collectively contribute to the overall pressure drop in positive-pressure dilute-phase pneumatic conveying systems, highlighting the importance of accounting for natural grain variability in system design and optimization.

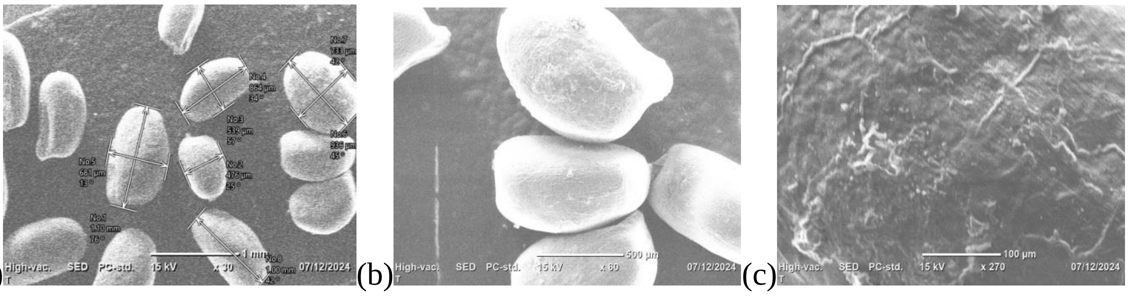

(a) (b) (c)

Figure 4.1. SEM image of teff grain (a) X30, (b) X60, and (c) X270

In addition to dimensional analysis, an electronic balance was used to measure teff-grain thousand-grain mass with a precision of 0.01 mg. Reliable measurements were essential for understanding the mass variations among the grain varieties, as illustrated in Table 4.1.

Table 4.1. Size and thousand-grain mass of teff grain

Teff variety	Moisture content(%)	Width (mm)	Thickness (mm)	Length (mm)	Thousand grain mass(g)
Felagot	8.431-10.1	0.54±0.07	0.51±0.08	0.89±0.08	251.82±0.05
Bishoftu	10.61-10.8	0.60±0.14	0.54±0.08	0.94±0.15	287.39±0.03

Teff variety	Moisture content(%)	Width (mm)	Thickness (mm)	Length (mm)	Thousand grain mass(g)
Boni	9.592-11.6	0.59±0.09	0.53±0.03	0.92±0.15	283.42±0.04

After the determination of dimensions, geometric mean diameter (D_g) and arithmetic mean diameter (D_a) were calculated according to Zewdu & Solomon (2007b). Calculating average D_g and D_a for each variety was determined by measuring 20 individual grains represented in Figure 4.2, with a total of 60 grains analyzed. Across all varieties, the average geometric mean diameter (D_g) was 0.68 mm, with a standard deviation of 0.067 units, while the average arithmetic mean diameter (D_a) was 0.72 mm with a standard deviation of 0.089 mm.

The slight difference between D_g and D_a may suggest non-spherical grain shapes, and the noticeable standard deviations indicate a fair degree of variability in grain size within and between varieties. The primary goal was likely to identify differences in grain size within and between varieties. Both size and thousand-grain mass were within the range of prior research that supports this finding (Abebaw & Abera, 2020; Sadik et al., 2013).

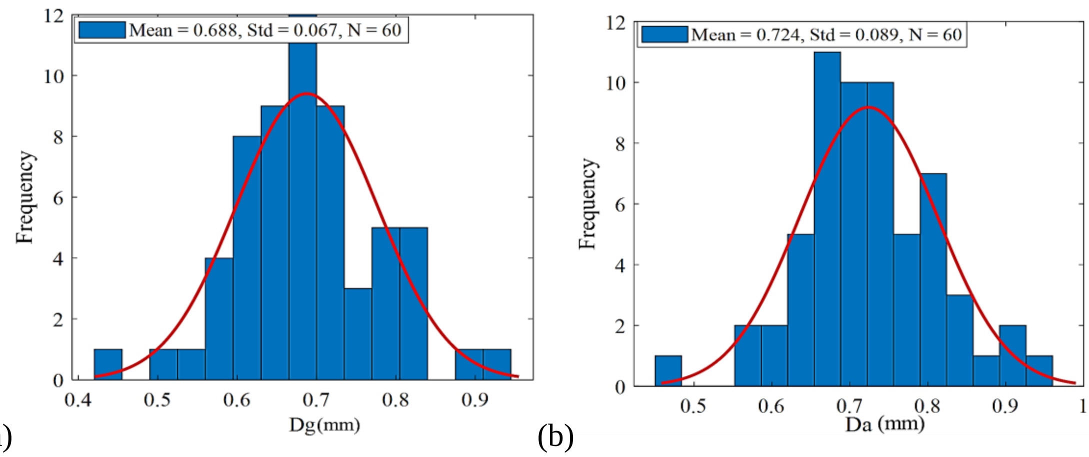

(a) (b)

Figure 4.2. Particle mean diameter

Densities of teff grain, including bulk density and particle density, were critical factors in determining the characteristics of the pneumatic conveying system presented. Additionally, porosity and voidage derived from bulk density and true density were also included, as shown in Table 4.2. The result of measured densities of teff grain was within the range of previous findings (Zewdu & Solomon, 2007b; Abebaw & Abera, 2020).

Particle size distribution was essential for pneumatic conveyor design and accurate CFD-DPM simulations. Teff grain size was measured using sieve analysis with five 200 mm sieves (2 mm, 1 mm, 710 μm, 500 μm, 355 μm) following ASTM D6913. The resulting size distribution was shown in Table 4.3.

Table 4.2. Measured physical properties of selected teff varieties

Teff Variety	Moisture content (%)	Bulk Density (kg/m^3)	True Density (kg/m^3)	Voidage (-)	Porosity (%)
Boset	10.12-10.49	779.93-855.23	1081.5-1357.04	0.31-0.35	23.59-25.85
Kora	8.974-11.76	803.47-952.73	1180.0-1410.85	0.61-0.75	37.90-42.90
Dagim	10.36-11.91	788.89-859.38	989.23-1320.77	0.34-0.72	25.39-42.05
Felagot	8.431-10.1	782.02-825.07	996.19-1396.80	0.38-0.61	27.38-37.78
Bora	10.56-12.54	788.81-842.40	1129.6-1414.62	0.44-0.79	30.52-44.18
Ebba	7.823-10.75	777.92-943.10	1035.7-1272.45	0.49-0.69	33.15-40.91
Bishoftu	10.61-10.8	783.87-846.00	1175.0-1373.60	0.52-0.59	34.12-37.14
Boni	9.592-11.6	774.72-843.19	993.85-1384.00	0.27-0.39	21.44-28.29

Table 4.3. Particle size distribution of selected teff varieties

Mesh Size (μm)	Particle size distribution (%)							
	Bora	Boset	Kora	Felagot	Boni	Dagim	Ebba	Bishoftu
710-1000	54.96	64.3	57.7	3.36	63.89	67.17	62.83	66.41
355-710	45.04	35.7	42.2	96.64	36.11	32.83	37.17	33.59

The particle size distribution of teff grains, as shown in Table 4.3, indicates that the majority of the grains fall within the 355 μm-1000 μm range across all varieties. Notably, no teff grains were found in the 1 mm-2 mm range. For most varieties, a significant proportion of the grains, over 50% were in the 710 μm-1000 μm range, except for Felagot, which has a distinctly lower percentage, 3.36%, in this size category. Instead, 96.64% of Felagot grains fall in the 355 μm-710 μm range, making it the finest among the varieties analyzed.

Other varieties, Bora, Boset, Kora, Boni, Dagim, Ebba, and Bishoftu, show a more balanced size distribution, with 32.83%-45.04% of grains in the 355-710 μm range. The absence of particles below 355 μm indicates that teff grains were generally larger than this threshold, influencing pneumatic conveying efficiency, pressure drop, and airflow demand. The results for particle size distributions were validated against research that supports this finding (Sadik et al., 2013).

Table 4.4. Angle of repose of selected teff varieties

Teff varieties	Moisture content(%)	Angle of repose(°)				
		Measurement3	Measurement2	Measurement1	Average	SD
Bishoftu	10.5-11.3	22.4	22.5	23.8	22.9	0.78
Boni	9.62-11.4	20.2	21.6	23.4	21.73	1.60

Teff varieties	Moisture content(%)	Angle of repose(°)				
		Measurement3	Measurement2	Measurement1	Average	SD
Felagot	8.85-10.8	21.5	22.8	23.5	22.6	1.02

Table 4.4 presents the angle of repose for three teff varieties, Bishoftu (DZ-Cr-497RIL133), Boni (DZ-Cr-498RIL37), and Felagot (DZ-Cr-442RIL77C), with values ranging from 20.2° to 23.8° across all measurements. The finding aligns with this research that supports this finding (Abebaw & Abera, 2020). This range indicates that teff grain can be classified as a very free-flowing bulk material, based on standard flowability classifications. The low angles of repose suggest that teff grain exhibits excellent flow behavior, which was advantageous in bulk handling systems. Consequently, no bulk flow issues were expected in the design of the feeder hopper for the pneumatic conveyor system, and this data serves as a reliable reference for ensuring smooth material discharge and flow during operation.

4.1.2. Aerodynamic property of teff grain

Terminal velocities of teff and major cereals were estimated using ANSYS Fluent coupled with Rocky DEM and validated against published experimental data from previous finding terminal velocities of cereal grains range from 3.08-3.96 m/s for teff, 6.81-6.86 m/s for wheat, 10.6-11.4 m/s for maize, 9.10-9.79 m/s for sorghum, and 6.8-8.53 m/s for barley (Song & Litchfield, 1991; Guner, 2007; Zewdu, 2007a).

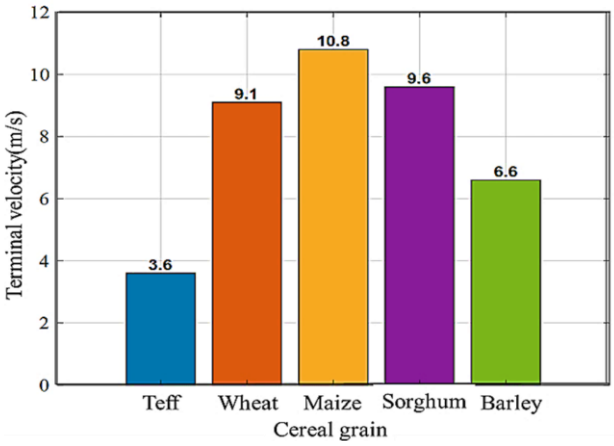

Figure 4.3. Terminal velocity of cereal grain using ANSYS Rocky DEM-CFD simulation

Figure 4.3 illustrates simulated results of terminal velocity for teff, wheat, maize, sorghum, and barley: 3.6 m/s, 9.1 m/s, 10.8 m/s, 9.6 m/s, and 6.6 m/s, respectively, demonstrating strong agreement with experimental findings. These results confirm the reliability of the DEM-CFD coupling approach for determining terminal velocity, making it a viable alternative to traditional experimental methods. Additionally, the lower terminal velocity of the teff grain indicates that it requires a lower airflow rate for full suspension in a pneumatic conveyor. The strong agreement confirms the model's reliability and highlights teff's much lower terminal velocity, emphasizing the need for conveying systems tailored to its unique aerodynamic behavior (Song & Litchfield, 1991; Guner, 2007; Zewdu, 2007a).

4.1.3. Minimum conveying velocity

The investigation confirmed two critical velocity parameters governing pneumatic conveying performance. Saltation velocity, defined as the minimum air velocity required maintaining particle suspension in horizontal flow and preventing settling, was established as a fundamental design parameter. Simultaneously, superficial gas velocity, representing the actual conveying gas velocity calculated based on the entire pipe cross-sectional area, was characterized as the operational velocity parameter. The relationship between these two velocities proved crucial for system optimization, with the superficial gas velocity necessarily maintained above the saltation velocity to ensure stable, non-settling transport conditions throughout the pneumatic conveying system.

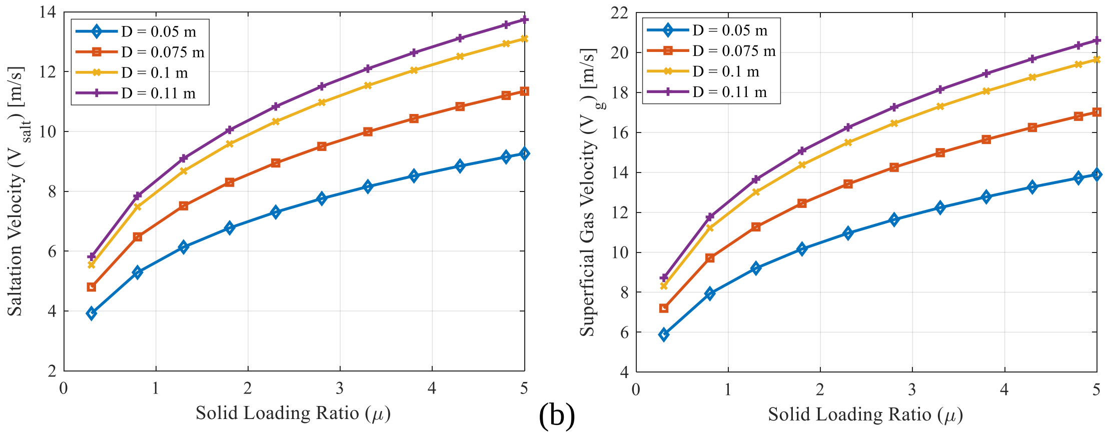

(a) (b)

Figure 4.4. Minimum conveying air velocity of teff grain

Figure 4.4 illustrates the variation of saltation velocity for teff grain, calculated using Rizk's Equation (Equation 2.11) concerning pipe diameter (50 mm to 110 mm) and solid loading ratio (0.3 to 5). As pipe diameter and solid loading ratio increase, higher saltation velocities were required. For each pipe diameter, the saltation velocity was: for D = 50 mm, it ranges from 4.0 to 9.5 m/s. For D = 75 mm, it ranges from 4.8 to 11.5 m/s. For D = 100 mm, it ranges from 5.6 to 13.2 m/s, and for D = 110 mm, it ranges from 5.8 to 13.8 m/s.

Since the superficial gas velocity was typically 1.5 times the saltation velocity (Kong, 2022), its corresponding ranges were: for D = 50mm, it ranges from 6.0 to 14.25 m/s, for D = 75 mm, it ranges from 7.2 to 17.25 m/s, for D = 100 mm, it ranges from 7.5 to 19.8 m/s and for D = 110 mm, it ranges from 7.5 to 20.7 m/s. This finding was supported by Yang et al. (2024) and Barrozo et al. (2010); accordingly minimum conveying velocity of teff grain was within the range of the minimum conveying velocity of common fine dry bulk material.

4.1.4. Gas fluidization characteristics of teff grain

Gas fluidization was identified as a critical process behavior for fine, dry bulk materials in industrial applications such as drying, mixing, and pneumatic transport. The analysis confirmed that the fluidization characteristics of teff grain differed substantially from those of major cereals. This divergence was attributed to teff's distinct physical properties, primarily its exceptionally small particle size, unique density, and lower aerodynamic drag, as evidenced by its lower terminal velocity. These specific characteristics directly influenced the minimum fluidization velocity, bed expansion, and overall flow dynamics. Consequently, a thorough understanding of teff's unique fluidization behavior was essential for the effective design and optimization of industrial handling systems, including pneumatic conveyors, to ensure efficient and reliable operation.

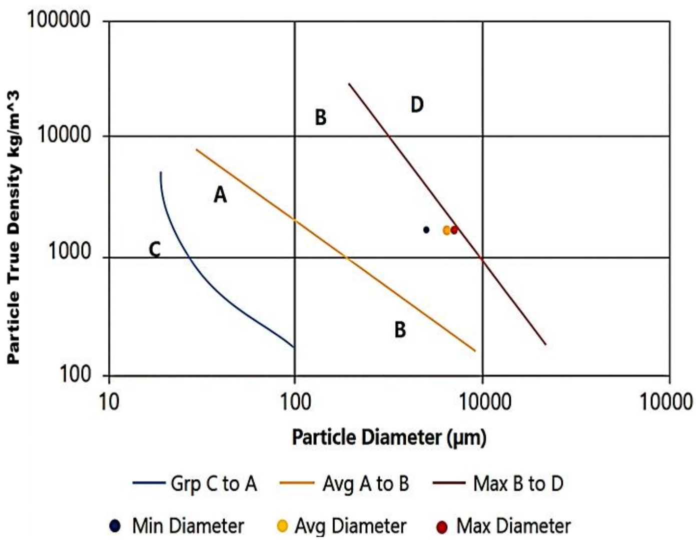

Figure 4.5. Geldart classification graph for teff grain generated by Pneucalc software

Based on Geldart's classification of particles shown in Figure 4.5, the teff grain falls under Group B, medium-sized and medium-density particles (Yehuda & Kalman, 2020). Group B materials exhibit bubbling in the bed with bubbles causing disturbances. These disturbances typically lead to turbulent flow in dense-phase pneumatic conveying systems, resulting in uneven flow, high-pressure drop, and blockages. This classification forms the foundation for understanding the gas-fluidization characteristics of teff grain and its implications for pneumatic conveying. Figure 4.6 (a) shows a non-fluidized bed, Figure 4.6 (b) marks the start of bubbling, Figure 4.6 (c) presents bubble expansion, Figure 4.6 (d) indicates bed instability with moderate bubbles, and Figure 4.6 (e) illustrates large bubbles with particle escape. Experimental observations confirm that teff grain fluidizes and forms bubbles at low air velocities, with a clear dependence between minimum fluidization velocity and pressure drop. Due to weak air retention, teff grain performs better in dilute-phase pneumatic conveying than in dense-phase systems, improving operational efficiency.

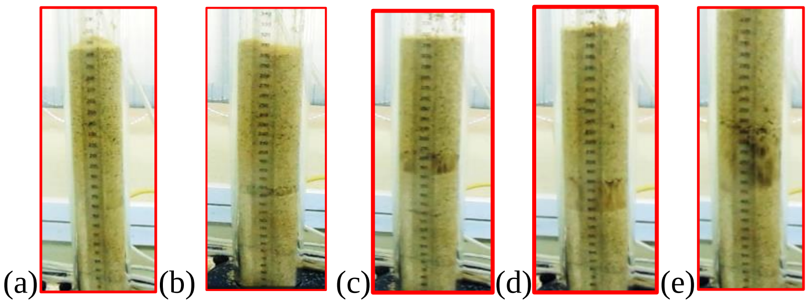

Figure 4.6. Fluidized bed test result for teff grain (a) fixed bed, (b) bubble formed, (c) bubbles growth, (d) moderate bubble and unstable bed formed, and (e) large bubble formed

Figure 4.6 shows that teff grains begin bubbling at low air speeds and continue until pressure stabilizes. Increasing airflow raises pressure loss, enlarges bubbles, and disturbs the bed. At peak pressure, conditions remain constant, while excessive airflow causes particle discharge. Minimum fluidization velocity and pressure loss vary with teff grain moisture content and variety.

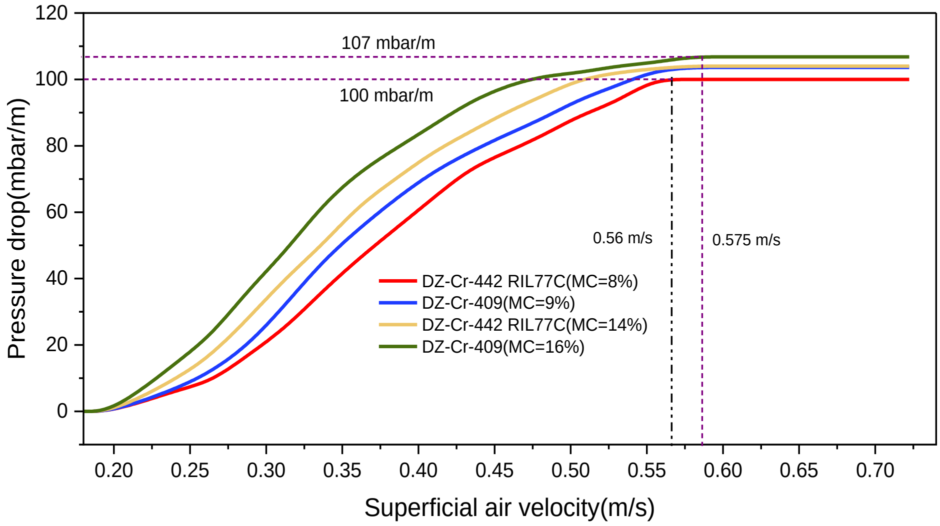

Figure 4.7. Effect of superficial air velocity on pressure drop/bed height of teff grain

Figure 4.7 fluidized bed test for DZ-CR-442 RL77C (8%), DZ-CR-442 RL77C (14%), DZ-Cr-409 (9%), and DZ-Cr-409 (16%) illustrates the varying moisture levels and its variety. Minimum fluidization velocity ranges from 0.56 - 0.575m/s, while the pressure drop ranges from 100 - 107mbar/m. The finding aligns with prior research that supports this finding (Zewdu & Siraj, 2021).

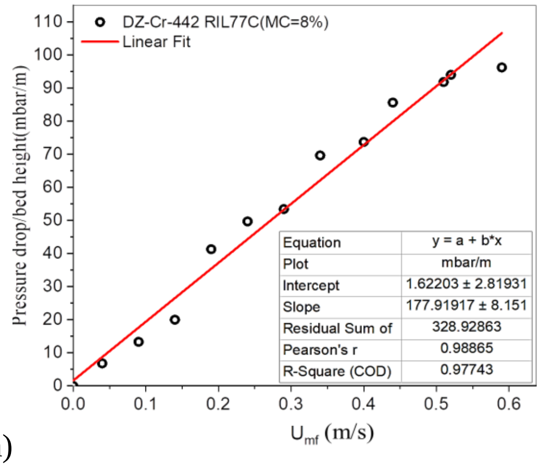

(a)

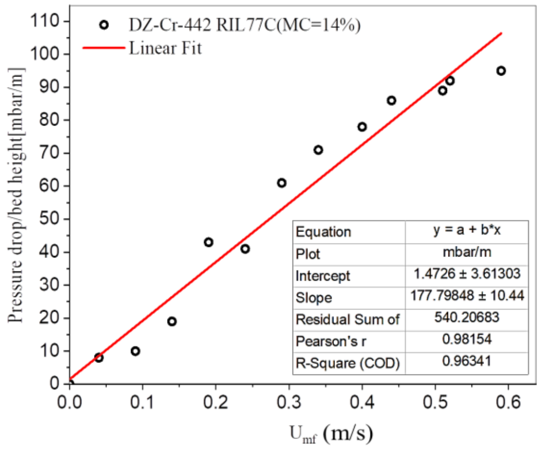

(b)

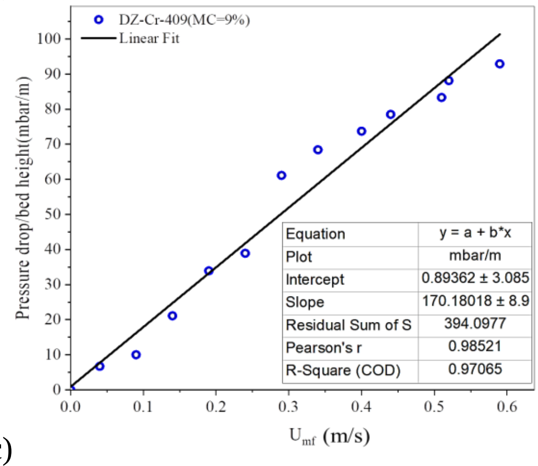

(c)

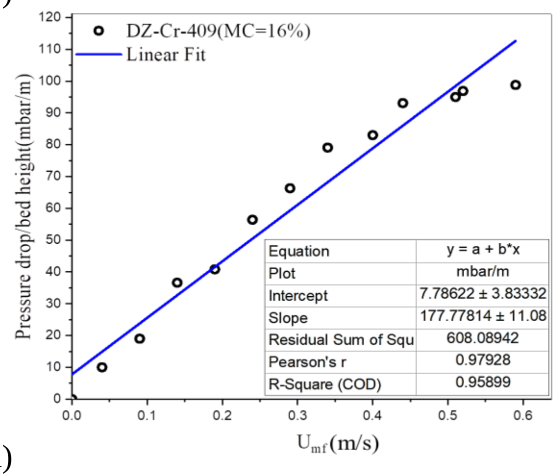

(d)

Figure 4.8. Effect of moisture content on U_{mf} and pressure drop/bed height of teff grain

Figure 4.8 illustrates how minimum fluidization velocity and pressure drop vary with bed height for two teff varieties (DZ-Cr-442 RIL77C and DZ-Cr-409), highlighting the effects of grain type and moisture content. DZ-Cr-442 RIL77C at 8% moisture shows the strongest correlation (R^2 = 0.977), reflecting very consistent fluidization. At 14% moisture, the same variety has a slightly lower correlation (R^2 = 0.963), indicating minor changes with increased moisture. DZ-Cr-409 at 9% maintains a high correlation (R^2 = 0.970), while at 16% it is lowest (R^2 = 0.958), suggesting that higher moisture slightly influences inter-particle cohesion or density. Overall, the high R^2 values verify the experimental data's reliability.

Overall, both the moisture level and the specific variety of teff grain strongly affect its gas fluidization behavior, providing valuable guidance for enhancing the efficiency and performance of industrial processes, including drying, pneumatic transport, handling, and separation of teff grains under different operating conditions.

Table 4.5. ANOVA on effect of MC and teff variety on fluidization of teff grain

ANOVA					
Source of Variation	The sum of Squares (SS)	Degrees of Freedom (df)	Mean Square (MS)	F-value	p-value
Moisture Content(MC)	1125.6	3	375.2	58.4	< 0.001
Variety	420.3	1	420.3	65.4	< 0.001
Residuals	313.5	63	4.98		
Total	1859.4				

Table 4.5 indicates that ANOVA results confirm both moisture content (MC) and teff grain variety have a significant impact on gas fluidization behavior. Moisture content shows a highly significant effect ($p < 0.001$) with an F-value of 58.4, demonstrating strong control over fluidization. The sum of squares (1125.6) suggests moisture is the dominant factor influencing pressure drop. Increased moisture likely enhances inter-grain cohesion, making fluidization more challenging and resulting in higher pressure drop values.

Likewise, teff grain variety shows a significant influence ($p < 0.001$, $F = 65.4$), demonstrating that different varieties display unique fluidization patterns. These variations are attributed to differences in grain size, shape, and surface properties, which in turn impact airflow resistance and overall fluidization performance.

The residual variance remained fairly low (SS = 313.5), indicating that the model accounts for the majority of the observed variation. These results carry practical significance for industrial processes such as drying, pneumatic transport, and grain separation, where knowledge of how moisture content and grain variety influence fluidization can assist in optimizing operational conditions and improving overall process efficiency.

4.2. Results and discussions on an investigation of pressure drop in the system

4.2.1. Experimental investigation of pressure drop in the system

The results showed that the system's pressure drop was strongly influenced by all tested factors. It increased with higher air velocity and material flow rate due to greater friction and particle interaction losses. A smaller pipe diameter of 46 mm and longer pipe length significantly raised the pressure drop, while the bend configuration, particularly the horizontal-to-vertical upward H-V UP bend, proved to be a major source of energy loss. The 150 mm cyclone separator also produced a higher pressure drop than larger units, showing that system geometry was as crucial as operating conditions in determining energy demand. The detailed results and discussion were presented below.

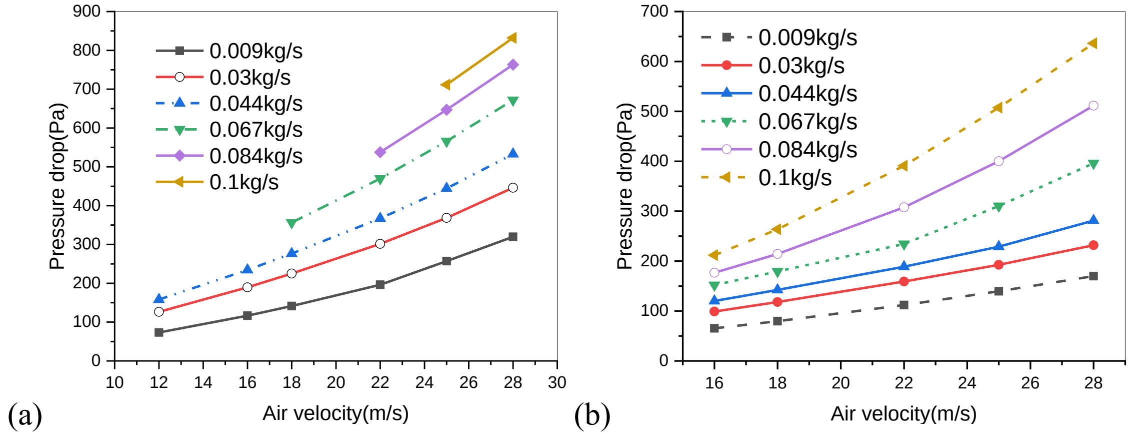

Figure 4.9. Effect of air velocity and feed rate on PD for feeder: (a) 46mm and (b) 71mm

Figure 4.9 illustrates that pressure drop due to the feeder for Figure 4.9 (a) v = 12 - 28 m/s, m_s = 0.009 - 0.1 kg/s, and D = 46mm, and Figure 4.9 (b) v = 16 - 28 m/s, m_s = 0.009 - 0.1 kg/s, and for D = 71 mm.

Feeder Section: Figure 4.9 shows clear performance differences between the 46 mm and 71 mm feeders tested at 12-28 m/s air velocity and 0.009-0.1 kg/s material flow. The smaller feeder produced much higher pressure drops, especially at lower velocities, highlighting the critical role of feeder design in system efficiency.

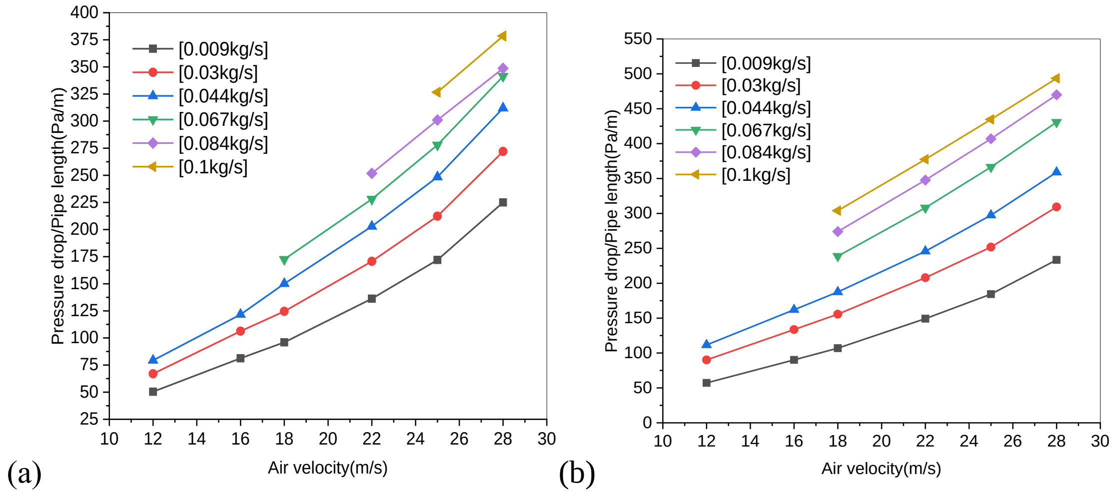

Figure 4.10. Effect of air velocity and feed rate on PD in HP for length (a) 4000mm and (b) 6000mm

Figure 4.10 shows that pressure drop due to horizontal pipes for Figure 4.10 (a) v = 12 - 28 m/s, m_s = 0.009 - 0.1 kg/s, D = 46 mm and L = 4000 mm, and Figure 4.10 (b) v = 12 - 28 m/s, m_s = 0.009 - 0.1 kg/s, D = 46 mm and L = 6000 mm.

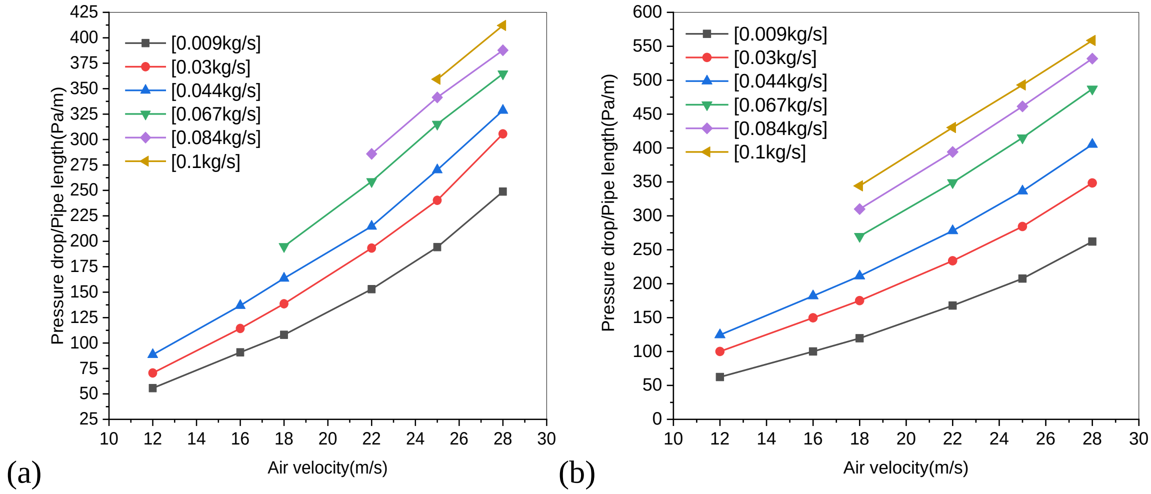

Figure 4.11. Effect of air velocity and feed rate on PD for VP with diameter length (a) 4000mm and (b) 6000mm

Figure 4.11 shows that pressure drop due to verticle pipes for Figure 4.11 (a) v = 12 - 28 m/s, m_s = 0.009 - 0.1 kg/s, D = 46 mm and L = 4000 mm, and Figure 4.11 (b) v = 12 - 28 m/s, m_s = 0.009 - 0.1 kg/s, D = 46 mm and L = 6000 mm.

Horizontal and Vertical Pipes: Figures 4.10-4.11 show pressure losses in 46 mm pipes of 4000 mm and 6000 mm under all test velocities and flow rates. Pressure drop increased linearly with pipe length, with the 6000 mm sections showing higher losses. Vertical pipes also produced slightly higher pressure drops than horizontal ones due to the added energy required to overcome gravity.

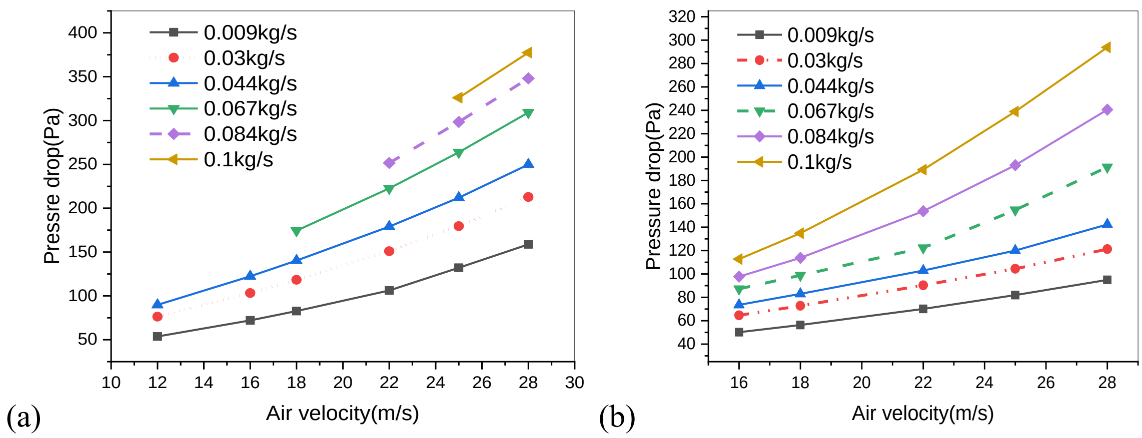

Figure 4.12. Effect of air velocity and feed rate on PD for 90^o bends for diameter (a) 46mm and (b) 71mm

Figure 4.12 highlights that pressure drop due to 90^0 bends for Figure 4.12 (a) v = 12 - 28 m/s, m_s = 0.009 - 0.1 kg/s, and for D = 46 mm for 90^0 bends, and Figure 4.12 (b) v = 12 - 28 m/s, m_s = 0.009 - 0.1 kg/s, and D = 71 mm for 90^0 bends.

90° Bends: The influence of pipe diameter on bend losses was shown in Figure 4.12, comparing 46 mm and 71 mm diameters across velocities of 12-28 m/s and material flow rates of 0.009-0.1 kg/s. The 46 mm diameter bends generated substantially higher pressure drops, particularly at elevated velocities, highlighting the significant impact of flow constriction and particle-wall interactions in directional changes.

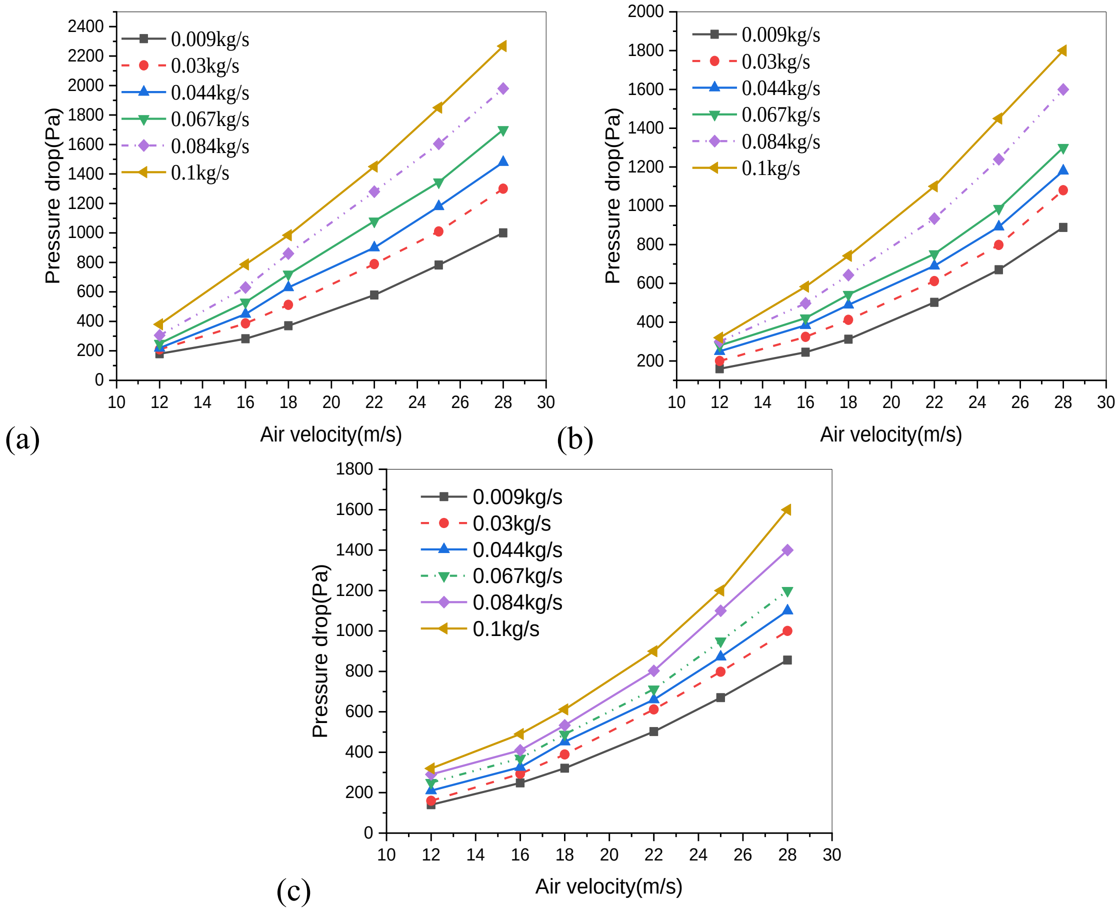

Figure 4.13. Effect of air velocity and feed rate on PD in CS for diameter (a) 150mm, (b) 180mm, and (c) 200mm

Figure 4.13 highlight that pressure drop due to cyclone separator for Figure 4.13 (a) v = 12 - 28 m/s, m_s = 0.009 - 0.1 kg/s, and D = 150 mm and Figure 4.13 (b) v = 12 - 28 m/s, m_s = 0.009 - 0.1 kg/s and D = 180 mm, and Figure 4.13 (c) v = 12 - 28 m/s, m_s = 0.009 - 0.1 kg/s and D = 200 mm.

Cyclone Separators: Figure 4.13 illustrates the pressure drop across three cyclone diameters (150 mm, 180 mm, and 200 mm) under the same operational conditions. The results demonstrate an inverse relationship between cyclone diameter and pressure drop, with the 150 mm cyclone exhibiting the highest resistance due to intensified centrifugal forces and internal turbulence. This establishes a critical trade-off between separation efficiency and energy consumption in cyclone selection.

Overall, the results show that pressure drop was strongly affected by both operating conditions and system geometry. Smaller diameters and longer pipes increase energy loss, with vertical sections adding extra drop due to gravity. Bends and cyclone separators further raise losses because of directional changes and constricted flow paths. Importantly, these combined effects significantly influence system performance. Pressure drop rises with increasing material flow rate and decreases with higher air velocity, consistent with the findings of Ozlu & Guner (2022) and Shijo & Behera (2021).

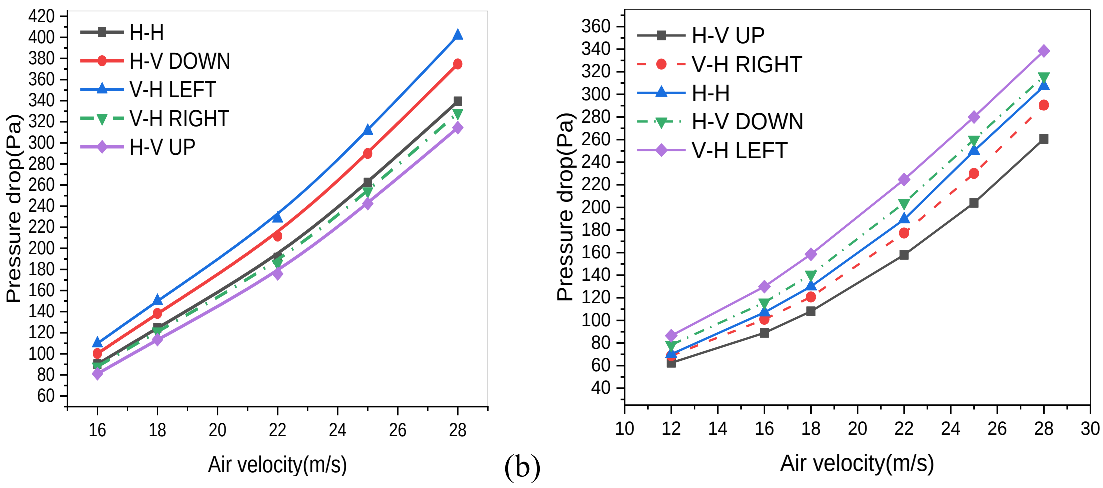

(a) (b)

Figure 4.14. Effect of 90^{o} bend layout and air velocity on pressure drop for pipe diameters of 46 and 71 mm

Figure 4.14 shows that the pressure drop due to 90^{0} bends layouts for Figure 4.14 (a) v = 12 - 28 m/s, m_s = 0.009 - 0.1kg/s and D = 46 mm, and Figure 4.14 (b) v = 12 - 28 m/s, m_s = 0.009 - 0.1 kg/s and D = 71mm.

Table 4.6. Analysis of variance for small pipe size (D = 46 mm)

ANOVA					
Pressure drop for 90^{o} bends layouts					
Source of Variation	The sum of Squares (SS)	Degrees of Freedom (df)	Mean Square (MS)	F-value	p-value
Between groups	11729.045	4	2932.262	0.999	0.414
Within groups	220129.10	75	2935.055		
Total	231858.15	79			

Table 4.7. Analysis of variance for medium pipe size (D = 71 mm)

ANOVA					
Pressure drop for 90^o bends layouts					
Source of Variation	The sum of Squares (SS)	Degrees of Freedom (df)	Mean Square (MS)	F-value	p-value
Between groups	1166.52	4	291.631	0.265	0.899
Within groups	82496.06	75	1099.94		
Total	83662.59	79			

As the pressure drops across different 90^o bend layouts in Figure 4.14 comparative analysis done and presented in Table 4.6 and Table 4.7 which illustrates ANOVA results for the 90^o bends layout with pipe bore diameters of 46 mm and 71 mm indicate no statistically significant differences in pressure drop across the different bend layouts, as shown by high p-values 0.414 for 46 mm and 0.899 for 71 mm and F-values lower than 1. For the 46 mm pipe, the total variability in pressure drop was a higher sum of squares = 231858.15 compared to the 71 mm pipe sum of squares = 83662.59, suggesting that the smaller diameter contributes to greater resistance and variation. However, in both cases, the majority of the variability was attributed to within-group differences rather than differences between the bend layouts, indicating that the bend layout does not significantly affect pressure drop under the tested conditions. The findings of this study were also in agreement with the trends reported by Dikty (2025).

4.2.2. CFD-DPM simulation

The CFD-DPM simulation results demonstrated the model's feasibility as a reliable alternative to laboratory experiments. Validation was conducted through comparison with experimental data, which confirmed the accuracy of the simulation approach. The analysis focused on critical teff grain properties, including particle size distribution, shape characteristics, and density variations. Computational parameters such as mesh sensitivity, wall functions, and residual convergence were systematically evaluated to ensure numerical reliability.

For the pneumatic conveying simulation, the model incorporated specific particle properties: a size distribution with minimum (d_{min} = 0.68 mm), mean (d_{mean} = 0.70 mm), and maximum (d_{max} = 0.72 mm) diameters; density values of ρ_{min} = 1120 kg/m³, ρ_{mean} = 1284 kg/m³ and ρ_{max} = 1381 kg/m³; and sphericity values of φ = 0.67- 0.70. The operating conditions included a mass flow rate of 0.03 kg/s, an air velocity of 20 m/s, and a pipe diameter of 46 mm, as documented in Figure 4.15 and Table 4.8. These comprehensive input parameters ensured the simulation accurately represented the physical behavior of teff grains in pneumatic conveying systems.

Table 4.8. Physical property of teff grain considered for CFD-DPM simulation setup

No	Mean particle diameter(mm)			Particle density(kg/m^3)			Sphericity(-)		
1	d_1	d_2	d_3	ρ_1	ρ_2	ρ_3	ϕ_1	ϕ_2	ϕ_3
	0.68	0.7	0.72	1120	1284	1381	0.67	0.68	0.7
2	$d_p = 0.7$			$\rho = 1240$			$\phi = 0.68$		

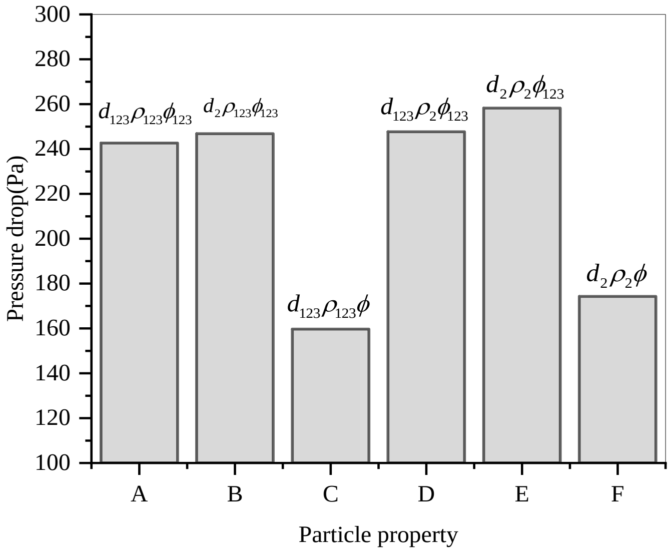

Figure 4.15. Particle properties considered in the CFD-DPM simulation

Figure 4.15, the bar chart illustrates the relationship between different particle properties and pressure drop (Pa). The x-axis represents various particle properties labeled A to F, while the y-axis shows the pressure drop (Pa). Bars A and B have similar pressure drops of 240 Pa, suggesting that all particle properties and influence pressure were similar. Bars C and F have the lowest pressure drop of 160 Pa - 170 Pa with a single particle shape, and Bars D and E have the highest pressure drop of 260 Pa, implying how much variation in particle shape contributes to resistance. Overall, the results indicate that pressure drop was highly influenced by variation in particle shape, as shown in bar E. A Combination of variations of particle shapes (ϕ_{123}) with mean particle diameter and particle density leads to a significant pressure drop when compared with a single particle shape (ϕ). The result in Figure 4.15 reflects the findings of Benard and Nally (2004), reporting that irregular or elongated particle shapes lead to significantly higher pressure drop, whereas spherical or uniform particles produce lower resistance.

4.2.3. Mesh sensitivity analysis

A sensitivity analysis was conducted on parameters like mesh size, pipeline layout, gas properties, material characteristics, and boundary conditions to validate the CFD-DPM simulation and assess their impact on pneumatic teff grain conveying. Results indicate that small parameter changes significantly affect system behavior, particularly pressure drop, highlighting the importance of precise parameter control for accurate modeling and reliable performance prediction.

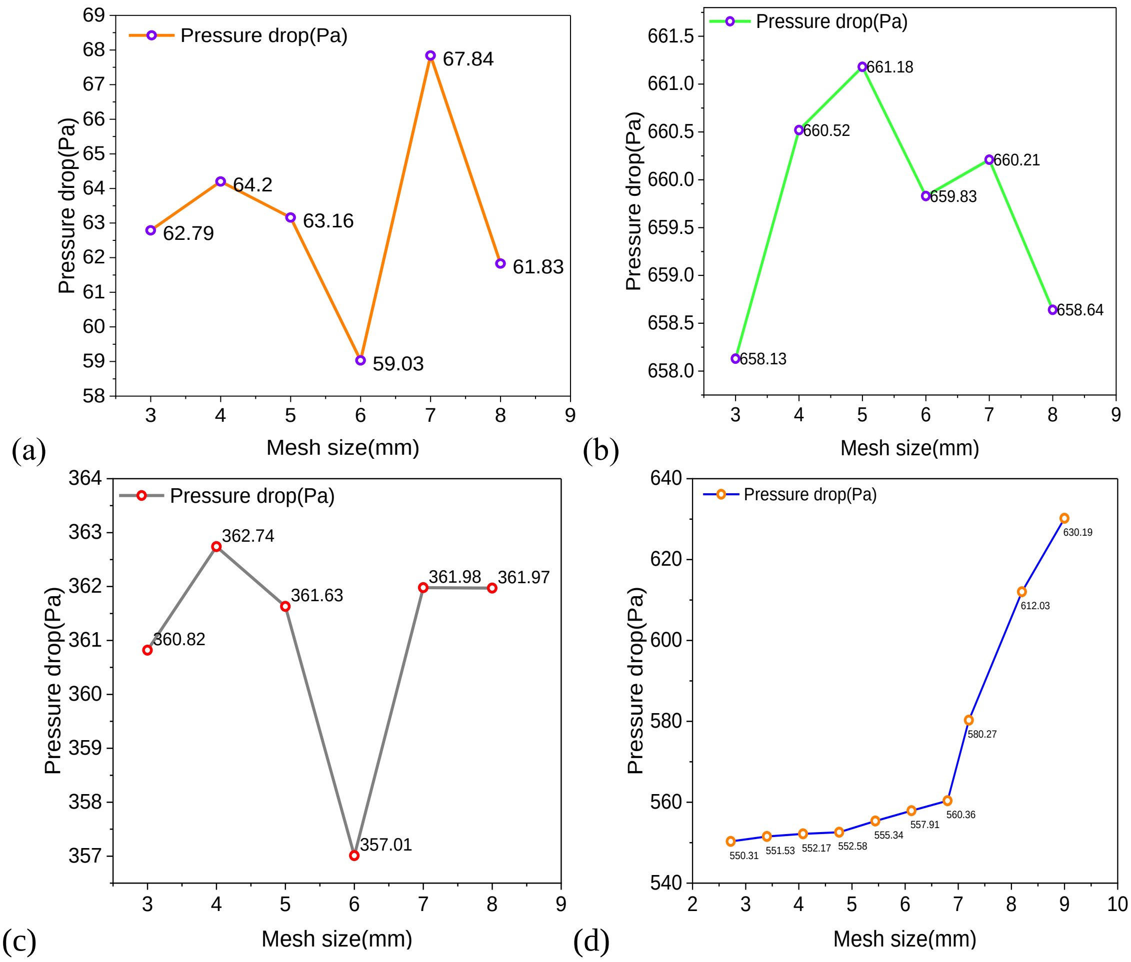

Figure 4.16. Effect of mesh size on pressure drop of (a) feeder, (b) SP, (d) 90^{o} bends, and (d) CS

Figure 4.16(a) grid dependency analysis for the feeder was analyzed for air velocity (v) = 16 m/s, material mass flow rate (m_s) = 0.009 kg/s, particle density (ρ) = 1284 kg/m^3, Rosin Rammler particle size distribution d_{p1} = 0.68mm, d_{p2} = 0.70 mm and d_{p3} = 0.72 mm, number of diameter = 10, spread diameter = 3.5. According to Cao et al. (2022), in CFD-DPM mesh size was 4 - 10 times the mean particle diameter.

Table 4.9. Regression ANOVA of mesh size vs. pressure drop for feeder

ANOVA					
Source of Variation	The sum of Squares (SS)	Degrees of Freedom (df)	Mean Square (MS)	F-value	p-value
Regression	1	0.0563	0.0563	0.00537	0.945
Residual	4	41.933	10.483		
Total	5	41.990			

Based on Table 4.9 on the regression analysis, mesh size did not have a significant effect on the pressure drop (Pa) in this dataset. This conclusion was supported by a p-value of 0.945, which was much higher than the typical significance level ($\alpha = 0.05$), and a very low F-value (0.00537), the regression model for (mesh size 3mm - 8 mm) indicating almost none of the variation in pressure drop of the feeder in a positive-pressure dilute-phase pneumatic teff grain conveyor.

Figure 4.16 (b) Grid dependency was analysis for straight pipeline was analyzed for pipe diameter (D) = 0.71 mm, pipe length (L) = 1500 mm, air velocity (v) = 20m/s, material mass flow rate (m_s) = 0.13 kg/s, particle density (ρ) = 1283 kg/m^3, Rosin Rammler particle size distribution d_{p1} = 0.68 mm, d_{p2} = 0.70 mm and d_{p3} = 0.72 mm, number of diameter = 10, spread diameter = 3.5, and mesh 3 mm - 8 mm as in CFD-DPM simulation mesh size was 4 -10 times, nodes, elements and pressure drop(Pa).

Table 4.10. Regression ANOVA of mesh size vs. pressure drop for straight pipelines

ANOVA					
Source of Variation	The sum of Squares (SS)	Degrees of Freedom (df)	Mean Square (MS)	F-value	p-value
Regression	1	0.000834	0.000834	0.000499	0.983255762
Residual	4	6.693251	1.673313		
Total	5	6.694085			

Table 4.10 indicates that mesh size varies from 3 mm to 8 mm; it has no significant effect on the pressure drop in the straight pipeline of a positive-pressure dilute-phase pneumatic teff grain conveyor, as indicated by the ANOVA results with an extremely low F-statistic (0.000499), a high p-value (0.983), and minimal variance explained by the regression model. Figure 4.16(c) Grid dependency analysis for 90^o bends was analyzed for pipe diameter (D) = 0.71mm, air velocity (v) = 20 m/s, material mass flow rate (m_s) = 0.1 kg/s,

particle density (ρ) = 1283 kg/m^3, Rosin Rammler particle size distribution dp1 = 0.68 mm, d_{p2} = 0.70 mm and dp3 = 0.72 mm, number of diameter = 10, spread diameter = 3.5, and mesh 3 mm - 8mm as in CFD-DPM simulation mesh size was 4 - 10 times, nodes, elements and pressure drop(Pa).

Figure 4.16(c) Grid dependency analysis for 90° bends was analyzed for pipe diameter (D) = 0.71mm, air velocity (v) = 20 m/s, material mass flow rate (m_s) = 0.1 kg/s, particle density (ρ) = 1283 kg/m^3, Rosin Rammler particle size distribution d_{p1} = 0.68 mm, d_{p2} = 0.70 mm and d_{p3} = 0.72 mm, number of diameter = 10, spread diameter = 3.5, and mesh 3 mm - 8mm as in CFD-DPM simulation mesh size was 4 - 10 times, nodes, elements and pressure drop(Pa).

Table 4.11. Regression ANOVA of mesh size vs. pressure drop for 90° bends

ANOVA					
Source of Variation	The sum of Squares (SS)	Degrees of Freedom (df)	Mean Square (MS)	F-value	p-value
Regression	1	0.018893	0.018893	0.00356	0.9553
Residual	4	21.25566	5.313914		
Total	5	21.27455			

Table 4.11 highlights that for (mesh size 3mm - 8 mm), ANOVA results for the 90° bend in the pneumatic conveying system indicate that the variation in pressure drop due to changes in mesh size was not statistically significant. The regression model explains only a small portion of the total variance, with a sum of squares (SS) of 0.0189 out of a total SS of 21.2746. The residual SS (21.2557) accounts for almost all the variance, indicating that most of the variation was due to other factors or random noise. The F-statistic (0.0036) was very low, and the p-value (0.9553) was much greater than the typical significance threshold of 0.05, confirming that the effect of mesh size on pressure drop in the 90° bend was negligible.

Figure 4.16(d) Grid dependency analysis for cyclone separator was analyzed for cyclone diameter (D) = 150 mm, air velocity (v) = 22m/s, material mass flow rate (m_s) = 0.067 kg/s, particle density (ρ) = 1283 kg/m^3, Rosin Rammler particle size distribution d_{p1} = 0.68mm, d_{p2} = 0.70 mm and d_{p3} = 0.72 mm, number of diameter = 10, spread diameter = 3.5, and mesh 3 mm - 9 mm as in CFD-DPM simulation mesh size was 4 - 10 times, nodes, elements and pressure drop(Pa).

From the mesh size versus the pressure drop curve of the cyclone separator, it was observed that the pressure drop curve exhibits a flat section. This flat section, occurring in the mesh refinement range of 2.72 mm to 6.8 mm, indicates that further mesh refinement has no significant effect on the solution.

4.2.4. Wall function

Wall functions were used to validate the CFD-DPM simulations by approximating the log-law region (30 < y+ < 300) for near-wall turbulence (Salim & Cheah, 2009). Computed y+ values across the pneumatic conveying system remained consistently within this range under all tested conditions, ensuring accurate modeling. The y+ parameter was expressed and evaluated as follows:

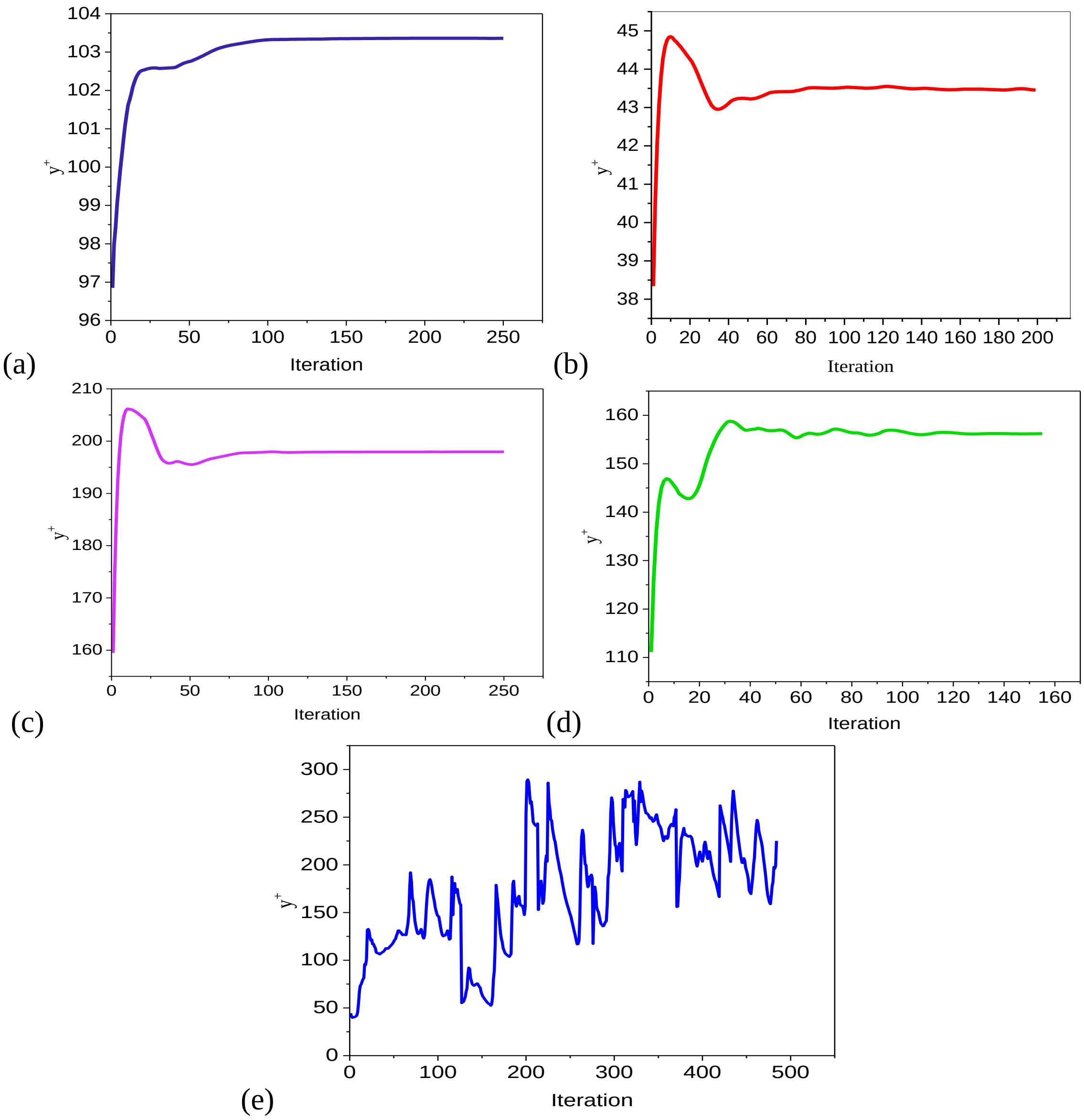

Figure 4.17. Y-Plus vs. iteration for (a) feeder, (b) HP, (c) VP, (d) 90^{o} bend, and (e) CS

Figure 4.17(a) y^+ value for D = 71mm, v = 20 m/s, m_s = 0.13 kg/s, mesh size 0.003 m, particle size for teff d_{p1} = 0.68 mm, d_{p2} = 0.70 mm and d_{p3}= 0.72 mm, teff particle density ρ_p = 1284kg/m^3 for feeder. It demonstrates that y^+ approaches 103 and remains constant around iteration 100.

Figure 4.17(b) y^+ value for D = 71 mm, v = 20m/s, m_s = 0.13kg/s, L = 4000 mm, mesh size 0.003m, particle size for teff d_{p1} = 0.68 mm, d_{p2} = 0.7 mm, and d_{p3} = 0.72 mm, teff particle density ρ_p = 1284 kg/m^3 for horizontal pipeline. Shows that y^+ approaches 43 and remains constant around iteration 80.

Figure 4.17(c) y^+ value for D = 71 mm, v = 20 m/s, m_s = 0.13 kg/s, L = 4000 mm, mesh size 0.003m, particle size for teff d_{p1} = 0.68 mm, d_{p2} = 0.7 mm, and d_{p3}= 0.72 mm, teff particle density ρ_p = 1284 kg/m^3 for vertical pipeline. Shows that y^+ approaches 195 and remains constant around iteration 100.

Figure 4.17(d) y^+ value for D = 71 mm, v = 20 m/s, m_s = 0.13 kg/s, R/D = 6, mesh size 0.003m, particle size for teff d_{p1} = 0.68 mm, d_{p2} = 0.7 mm, and d_{p3}= 0.72 mm, teff particle density ρ_p = 1284 kg/m^3 for 90^o bends. Shows that y^+ approaches 155 and remains constant around iteration 50.

Figure 4.17 (e) y^+ value for D = 180 mm, v = 16 m/s, m_s = 0.03 kg/s, mesh size 0.003 m, particle size for teff d_{p1} = 0.68 mm, d_{p2} = 0.7 mm and d_{p3} = 0.72 mm, teff particle density ρ_p = 1284 kg/m^3 for cyclone separator. Shows that y^+ fluctuates between 50 - 290 iterations from 0 - 500. This fluctuation happens due to swirling-dominated flow in a cyclone separator.

All the above results were supported by wall functions, which served as a critical validation criterion for the CFD-DPM simulations, providing a calibrated method corresponding to $30 < y+ < 300$ (Salim & Cheah, 2009).

4.2.5. Scaled residuals

In the CFD-DPM simulations, scaled residuals tracked imbalances in continuity, momentum, energy, turbulence, and discrete phase equations to indicate convergence and accuracy. Convergence was achieved when normalized residuals fell below 10^{-3}-10^{-6}, verified by mass balance and pressure stability checks. Residual monitoring also guided mesh refinement, solver optimization, and ensured physically consistent results.

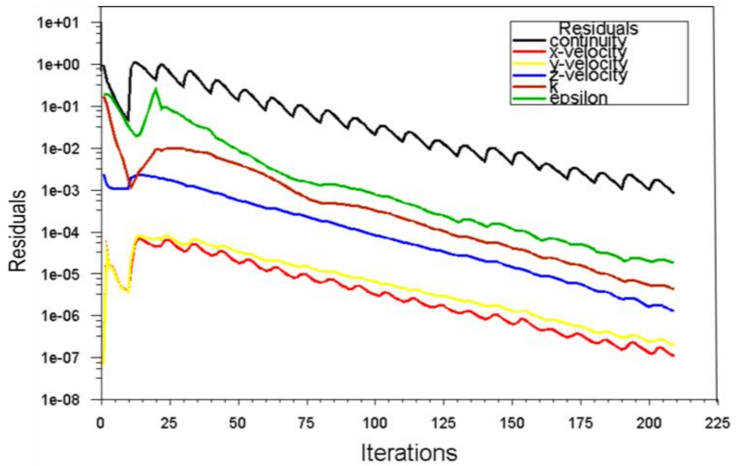

Figure 4.18. Scaled residuals for CFD-DPM simulation of a horizontal pipe

Figure 4.18. Scaled residuals for CFD-DPM simulation of a horizontal component with a diameter of 71 mm, mass flow rate of 0.13 kg/s, and velocity of 25 m/s show that convergence was attained by increasing the number of iterations from 300 to 400 and most of scaled residuals failed in the range between 10^{-3} to 10^{-7}, ensuring consistency, with convergence generally reached when values fall below 10^{-3} to 10^{-6}.

4.2.6. CFD-DPM simulation result

Figure 4.19- 4.23 illustrates ANYS fluent CFD-POST result for feeder, horizontal pipe, vertical pipe, 90^{o} bend, and cyclone separator. The results include pressure distribution (Pa), air velocity distribution (m/s), particle concentration (kg/m^3), and particle time (s). The results were presented for each component as follows:

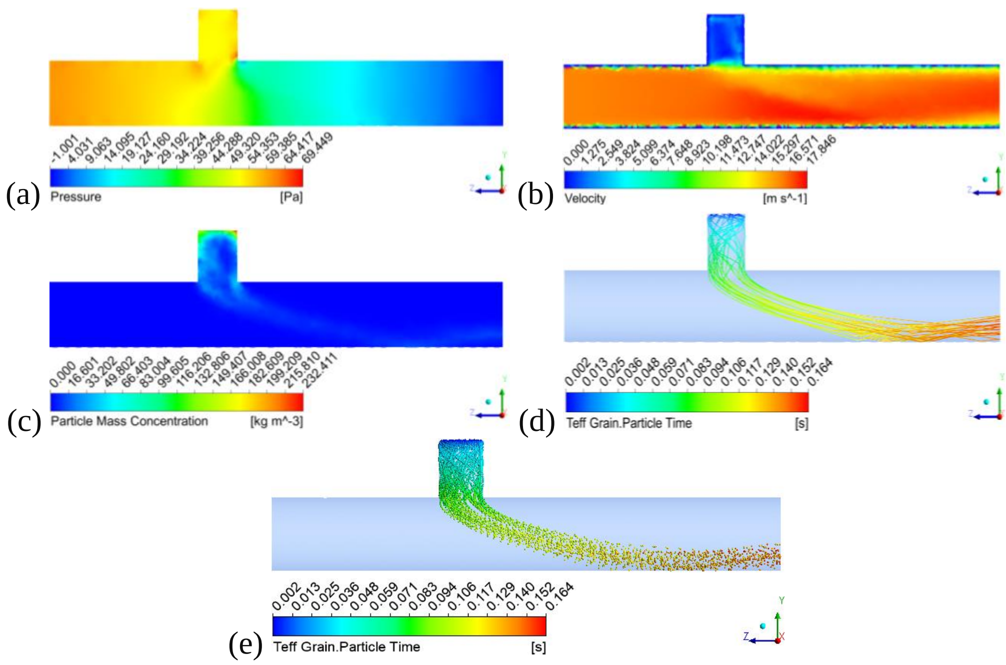

Figure 4.19. CFD-DPM simulation results for feeder

Figure 4.19 presents the CFD-DPM simulation results for the feeder, illustrating key parameters including pressure distribution (a), air velocity distribution (b), particle concentration (c), and teff particle travel time (d and e). The simulation was conducted under the conditions of a pipe diameter (D) of 46 mm, a material flow rate (m_s) of 0.009 kg/s, and an air velocity (v) of 16 m/s.

Figure 4.19(a) Pressure distribution ranges from -1.001 Pa to 69.449 Pa, showing that the pressure within the system varies significantly, with some areas experiencing pressure drops (negative values) and others under higher pressure. This pressure variation was crucial in understanding the dynamics of the material flow through the feeder.

Figure 4.19(b) Air velocity distribution spans from 0.000 m/s to 17.846 m/s, indicating that there were regions with almost no airflow (0 m/s) and others where the airflow reaches higher speeds. This variation in velocity affects how effectively the teff particles were conveyed through the system.

Figure 4.19(c) Particle concentration ranges from 0.000 kg/m³ to 232.411 kg/m³, indicating how the teff particles were dispersed within the airflow. A concentration of 0.000kg/m³ suggests areas with no particles, while values up to 232.411 kg/m³ represent regions with particle concentration.

Figure 4.19(e-d) particles move from the inlet to the outlet between 0.002 s and 0.164 s. This time frame captures their transit, interactions, and behavior, providing insights into particle-air dynamics.

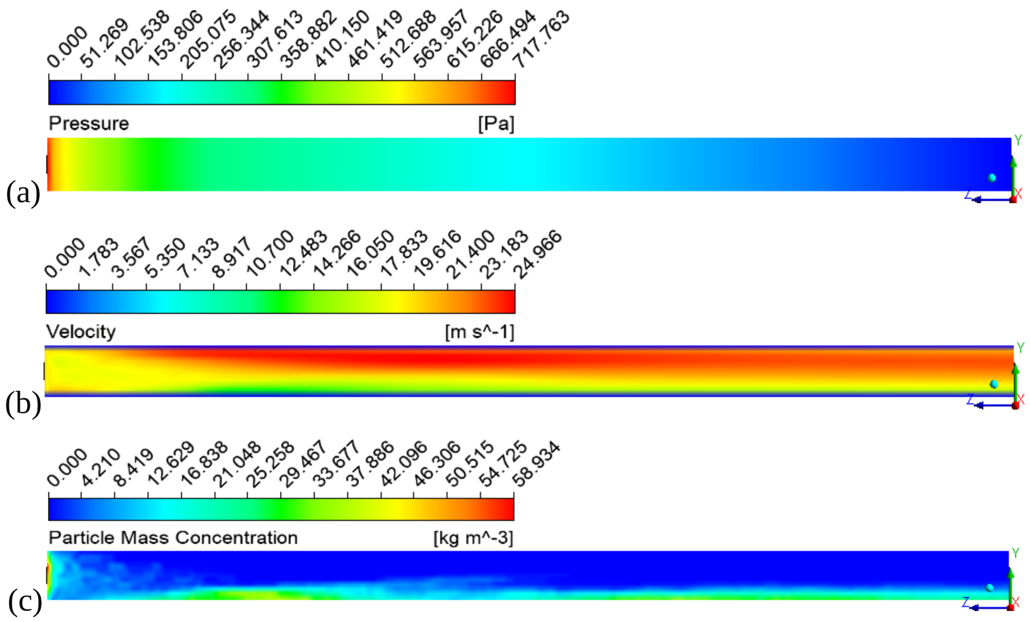

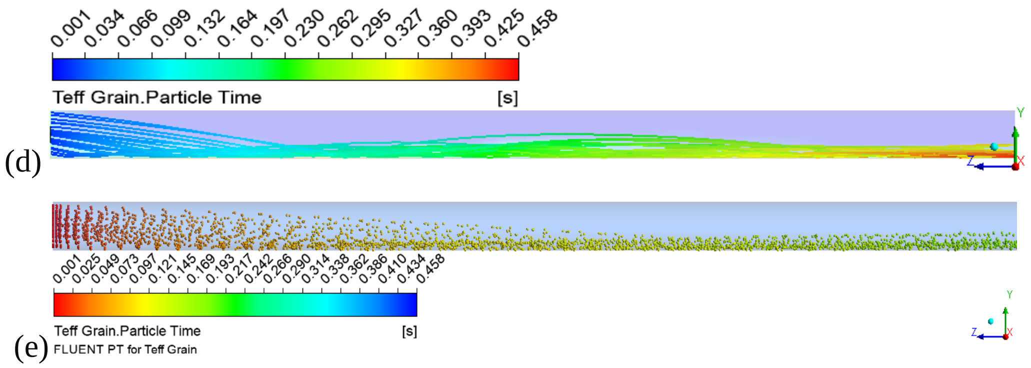

Figure 4.20. CFD-DPM simulation results for horizontal pipe

Figure 4.20, shows the CFD-DPM simulation results for the horizontal pipeline, illustrating pressure distribution (a), air velocity distribution (b), particle concentration (c), and teff particle travel time (d and e) for a pipeline with a diameter (D) of 71 mm, length (L) of 4000mm, a material flow rate (m_s) of 0.13 kg/s, and an air velocity (v) of 20 m/s.

Figure 4.20(a) Pressure distribution ranges from 0 Pa to 717.783 Pa, indicating significant pressure increases along the pipeline. This variation in pressure was critical for understanding how the system's flow resistance changes as the grain were conveyed through the horizontal pipe.

Figure 4.20(b) Air velocity distributions vary from 0.000 m/s to 24.966 m/s, showing regions where the airflow was absent (0 m/s) and other areas where the airflow reaches higher speeds. These differences in air velocity affect the overall efficiency of the pneumatic conveying system by influencing the movement of teff grains.

Figure 4.20(c) Particle concentration spans from 0.000 kg/m³ to 58.934 kg/m³, reflecting the distribution of teff grain particles within the airflow. The lower concentration values indicate areas where few or no particles were present, while the higher concentration values suggest regions of greater particle accumulation, which could affect the system's performance in terms of efficiency and material handling.

Figure 4.20(d-e) finally, the teff particle travel times were shown, with values in (d) ranging from 0.001 s to 0.458 s and in (e) from 0.001 s to 0.458 s. These travel times indicate the duration for teff particles to pass through the horizontal pipeline, with slight variations between the two travel times, reflecting differences in particle movement throughout the system.

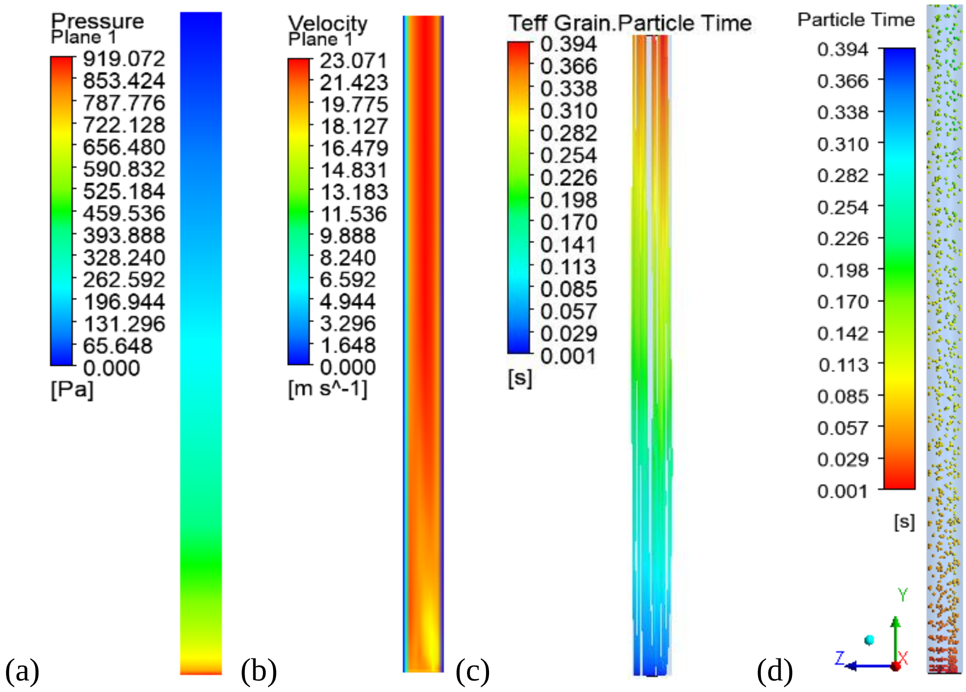

Figure 4.21. CFD-DPM simulation results for vertical pipe

Figure 4.21 presents the CFD-DPM simulation results for pneumatic conveying of teff grain through a vertical pipeline with a diameter of 71 mm, a material flow rate of 0.13 kg/s, and an air velocity of 20 m/s. The simulation highlights four key parameters: (a) pressure distribution, (b) air velocity distribution, and (c) and (d) teff particle travel times. The study focuses on the pneumatic conveying of teff grain through a vertical pipeline under specific operating conditions. These parameters establish the baseline for analyzing flow dynamics and particle behavior.

Figure 4.21(a) pressure distribution (a) ranges from 0 to 919.072 Pa, indicating the variation in pressure along the pipeline.

Figure 4.21(b) air velocity distribution spans from 0.000 to 23.071 m/s, representing the flow characteristics of the conveying air.

Figure 4.21(c-d) teff particle travel time was depicted in both, ranging from 0.001 to 0.394 seconds, which shows the duration taken by the particles to traverse the pipeline under the given operating conditions. These results provide a detailed visualization of the flow dynamics and particle behavior in the vertical pipeline. It was essential to break them down into key insights and technical implications.

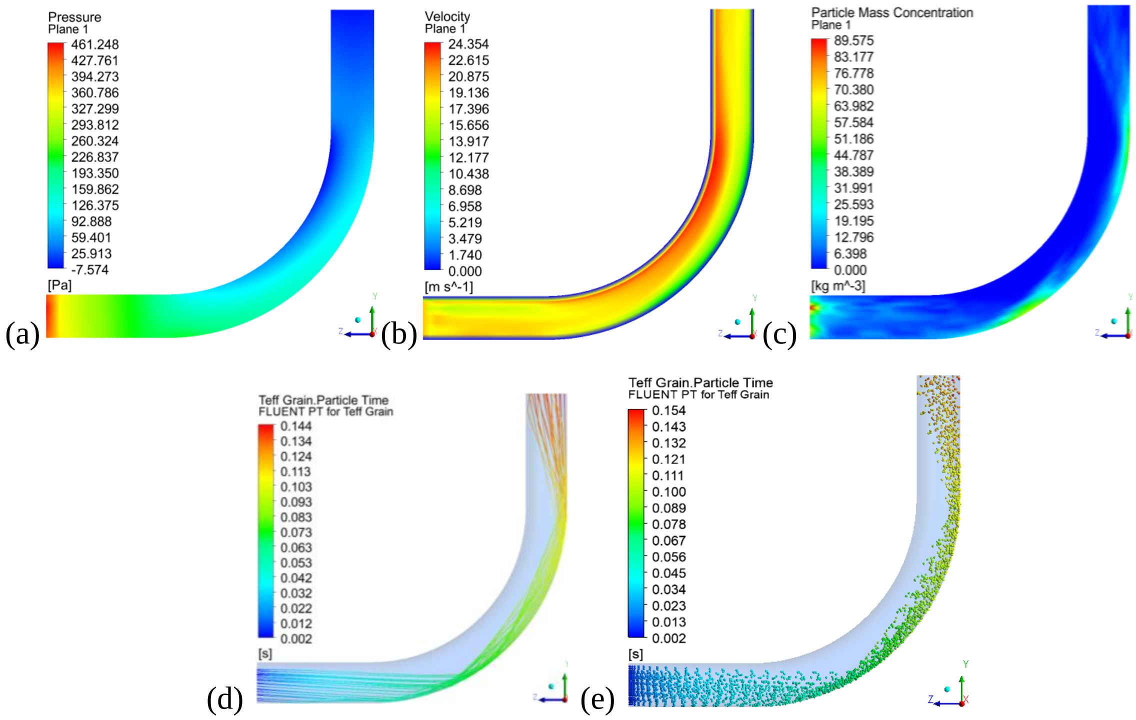

Figure 4.22. CFD-DPM simulation results for bends

Figure 4.22 presents the CFD-DPM simulation results for pneumatic conveying of teff grain through an H-V UP 90^{o} bend in a pipe with a diameter of 71 mm, a material flow rate of 0.13 kg/s, and an air velocity of 20 m/s.

Figure 4.22(a) Pressure distribution within the system ranges between -7.574 Pa and 461.248 Pa. This indicates a significant variation in pressure, with negative values suggesting areas where pressure drops, likely due to the bend in the pipe and changes in flow dynamics.

Figure 4.22(b) Air velocity distributions vary from 0.000 m/s to 24.354 m/s, showing areas where the airflow was minimal or absent and areas where it reaches high speeds. This variation in air velocity was important for understanding the performance of the pneumatic conveying system, particularly in how it affects the movement of teff grains.

Figure 4.22(c) Particle mass concentration spans from 0.000 kg/m^3 to 89.575 kg/m^3. This represents the density of teff grain particles in the air, with higher concentrations indicating regions of greater particle accumulation. The concentration varies across the system, highlighting how the particles disperse or cluster depending on the airflow conditions.

Figure 4.22(d-e) travel times of teff grains depicted in (d) and (e). In (d), the travel times range from 0.002 s to 0.144 s, while in (e), it was range from 0.002 s to 0.154 s. These variations in travel times reflect differences in how long it takes for particles to move through the system, which can be influenced by factors such as air velocity and particle concentration.

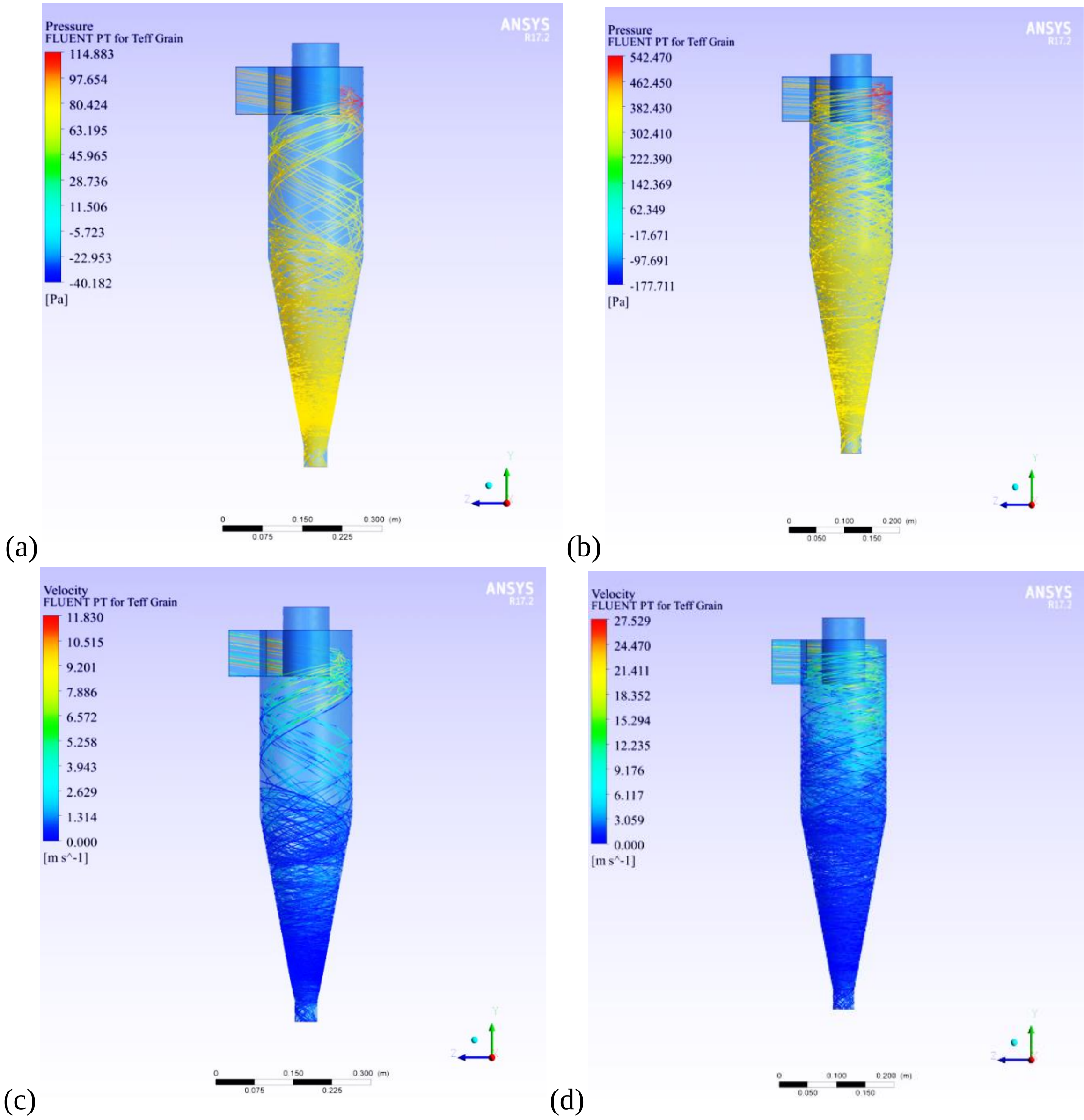

Figure 4.23. CFD-DPM simulation results for cyclone separator

Figure 4.23 presents the performance characteristics of a 0.9D cyclone separator under varying air velocities and material flow rates. The analysis includes pressure drop and air velocity distributions for two cases: at an air velocity of v = 10m/s with a material flow rate of m_s = 0.009 kg/s and at v = 22m/s with m_s = 0.067 kg/s.

Figures 4.23(a) and (c): As the air velocity increases from 0 to 11.83 m/s, the pressure within the cyclone varies between roughly -40 Pa and 115 Pa. This indicates a relatively moderate pressure change at lower airflow rates. The negative pressures suggest suction regions, typically near the inlet or vortex areas, while the positive pressures indicate zones of compression.

Figures 4.23(b) and (d): At higher air velocities, ranging from 0 to 27.53 m/s, the pressure distribution expands significantly, from -178 Pa to 542 Pa. This shows that increasing the air velocity dramatically amplifies both the maximum and minimum pressures inside the cyclone. The larger pressure range reflects stronger centrifugal effects and higher dynamic interactions between the air and particles at these velocities.

These results highlight the significant influence of increased air velocity and material flow rate on flow dynamics and pressure distribution, emphasizing the performance variations of the 0.9D cyclone separator in a positive-pressure dilute-phase pneumatic conveying system, and a detailed illustration of the CFD-DPM simulation set-up for the full system was shown in APPENDIX B.

4.2.7. Validation of CFD-DPM simulation against experimental results

The integrated approach combining CFD-DPM simulations with laboratory experiments revealed significant insights into the pressure drop in a positive-pressure dilute-phase pneumatic conveying system for teff grain. This comprehensive analysis provided a detailed understanding of the observed flow behavior and energy losses throughout the system. The results highlighted five key components where notable pressure variations occurred: the feeder, horizontal pipelines, vertical pipelines, bends, and the cyclone separator.

Laboratory experiments provided real-world pressure drop data under controlled conditions, serving as a benchmark to validate the CFD-DPM results. The findings demonstrated consistency with computational predictions, although limitations in setup, scale, and resources prevented measurement of every parameter across all components, highlighting the continued importance of computational support.

CFD-DPM simulations revealed detailed information about the airflow patterns, particle trajectories, and the complex interactions between solid particles and the conveying air. These results provided high-resolution insights into velocity distribution, turbulence, and pressure variations that would be difficult to observe through experimental methods alone. The computational analysis also highlighted the system behavior under multiple operating conditions, offering flexibility and reducing the need for extensive physical testing.

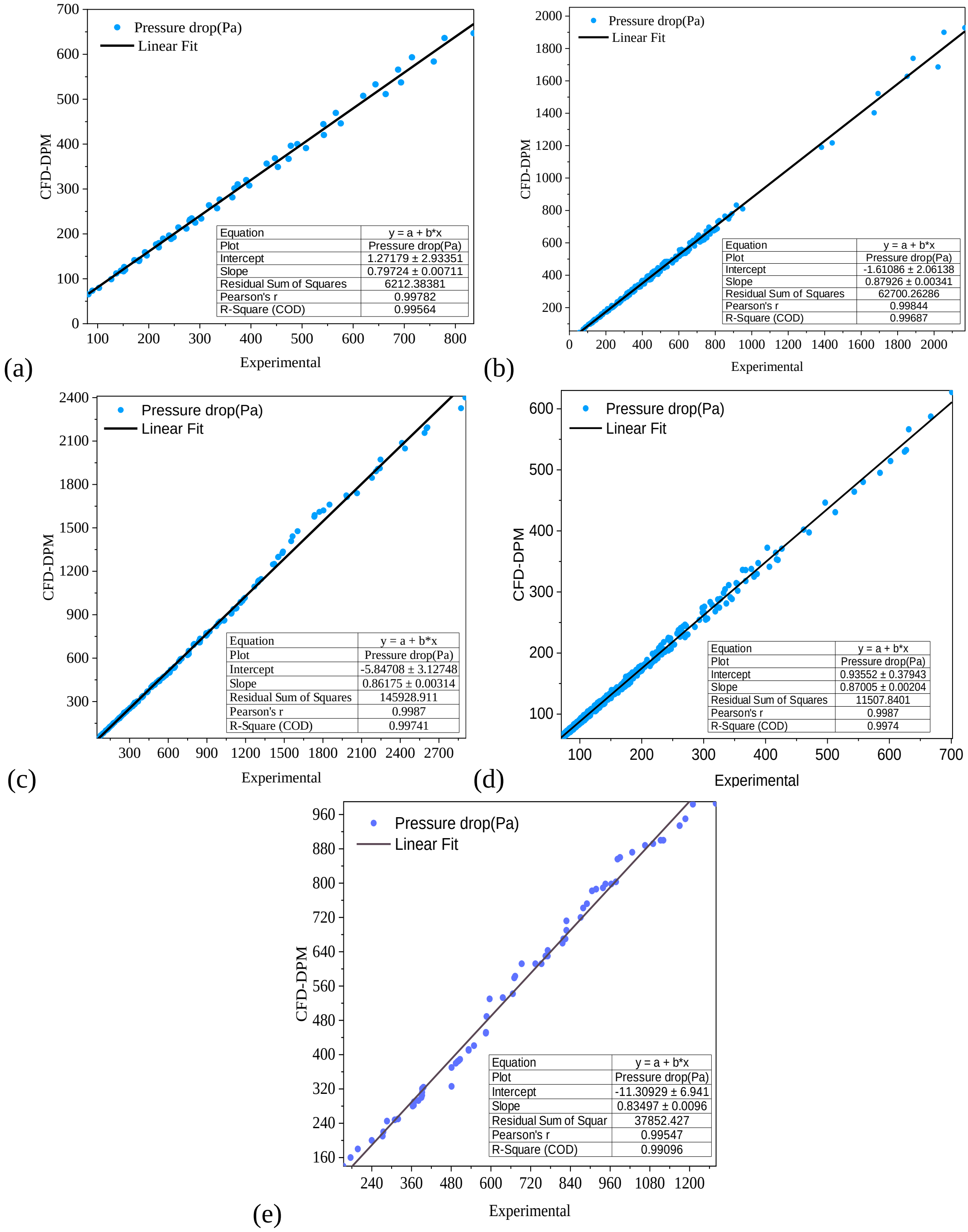

Figure 4.24. CFD-DPM vs. Exp for (a) feeder, (b) HP, (c) VP, (d) bends, and (e) CS

The results from Figure 4.24 demonstrate a highly successful validation of the CFD-DPM, where the exceptionally high R-Square values across all system components, ranging from

0.99096 for the cyclone separator to 0.9974 for the vertical pipes and 90° bends, with the feeder at 0.9956 and horizontal pipes at 0.9968, collectively indicate a near-perfect correlation between the simulation and experimental data. This consistently strong performance, with all values exceeding 0.99, confirms that the model was remarkably accurate and reliable for predicting particle behavior throughout the entire system, from the feeder and through the complex flows within pipes, bends, and the cyclone separator, establishing it as a highly trustworthy tool for analysis.

Table 4.12. Regression evaluation metrics for CFD-DPM validation

Evaluation metrics	Feeder	Horizontal pipes	Vertical pipes	90^{o} Bends	Cyclone separator
R-Square	0.9956	0.9968	0.9974	0.9974	0.99096
MSE	287.22	67.324	29.980	27.191	206.892
RMSE	16.947	8.2051	5.4753	5.2144	14.3837
MAE	16.65	7.5713	4.4699	4.1462	14
MAPE	20.304	13.904	9.5542	13.990	9.0909

Figure 4.24 (a-e) presents the CFD-DPM simulated versus experimental pressure drops for the feeder, horizontal pipes, vertical pipes, 90° bends, and cyclone separator. Table 4.12 summarizes the regression metrics used to evaluate the CFD-DPM model's predictive accuracy across these pipeline components. The metrics include R^2, MSE, RMSE, MAE, and MAPE, which together provide a comprehensive assessment of absolute and relative errors in Table 3.4 (Akoglu, 2018; Hange et al., 2020; Jierula et al., 2021).

Feeder: The CFD-DPM model for the feeder achieves an R^2 of 0.9956, indicating a very strong correlation between simulated and experimental data. Absolute error metrics (MSE = 287.22 Pa^2, RMSE = 16.947 Pa, MAE = 16.65 Pa) were slightly higher compared to other components, while MAPE = 20.304% reflects moderate proportional accuracy. These elevated errors were likely due to complex flow dynamics at the feeder inlet, where particle acceleration and turbulence contribute to prediction variability.

Horizontal Pipes: For horizontal pipes, the model demonstrates excellent predictive performance with R^2 = 0.9968, confirming high agreement with experimental observations. The error metrics (MSE = 67.324 Pa^2, RMSE = 8.2051 Pa, MAE = 7.5713 Pa, MAPE = 13.90%) were relatively low, indicating that the CFD-DPM model reliably captures pressure drop behavior in straight horizontal sections. This demonstrates the model's capacity to simulate steady, uniform flow accurately.

Vertical Pipes: The vertical pipe configuration also exhibits outstanding agreement with experimental data, achieving $R^2 = 0.9974$. Errors were minimal, with MSE = 29.980 Pa^2, RMSE = 5.4753 Pa, MAE = 4.4699 Pa, and MAPE = 9.55%, reflecting the model's high precision in predicting vertical flow characteristics. The low absolute and proportional errors indicate effective handling of gravitational effects and particle acceleration in vertical flow paths.

90° Bends: The CFD-DPM model shows robust predictive capability for 90° bends, with $R^2 = 0.9974$ and the lowest absolute errors among all components (MSE = 27.191 Pa^2, RMSE = 5.2144 Pa, MAE = 4.1462 Pa). The MAPE of 13.99% indicates good relative accuracy. These results confirm that the model effectively simulates curved flow paths and associated energy losses due to momentum changes and secondary flow structures in bends.

Cyclone Separator: For the cyclone separator, the model maintains high predictive performance with $R^2 = 0.9910$, while absolute errors (MSE = 206.892 Pa^2, RMSE = 14.3837 Pa, MAE = 14 Pa) were slightly higher than in straight pipes and bends. MAPE = 9.09% remains low, suggesting acceptable proportional accuracy. The relatively higher absolute errors reflect the complex swirling flow and particle separation mechanisms characteristic of cyclonic motion, which introduce additional modeling challenges.

The CFD-DPM model demonstrates strong predictive capability across all system components. While error magnitudes vary with the complexity of flow in each component, consistently high R^2 values and low-to-moderate error metrics indicate the model was reliable and valid for simulating pressure drops in the pneumatic conveyor system. The results highlight the model's robustness in both straight and curved pipelines, as well as in complex cyclone flow, supporting its use for design and operational optimization.

4.2.8. Power loss across system components

Pressure drop in a pneumatic conveyor directly affects energy efficiency, influencing power requirements and operating costs. Higher pressure drop increases resistance, demanding more energy to maintain airflow and prevent blockages. Proper system design, including pipe diameter and airflow rate, ensures efficient transport while minimizing energy consumption. In a positive-pressure dilute-phase pneumatic conveying system for teff grain, the pressure drop across different system components was calculated from the sum of the pressure drop across individual components.

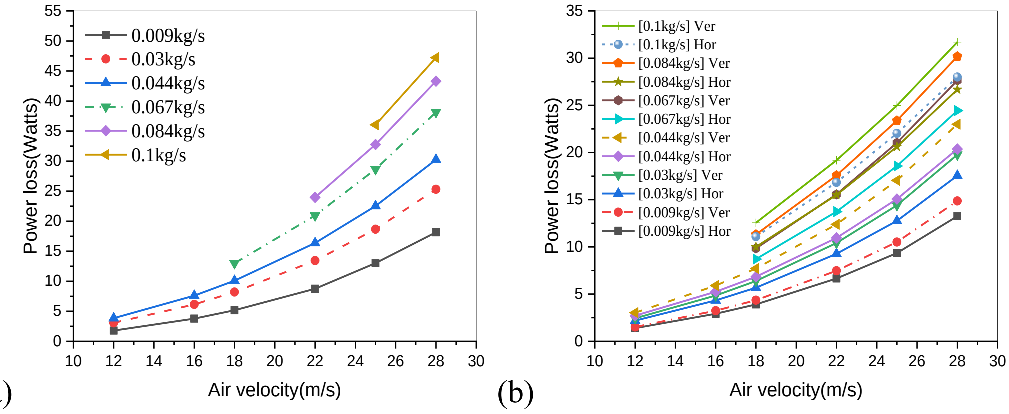

(a) (b)

Figure 4.25. Power loss due to (a) feeder and (b) straight pipe

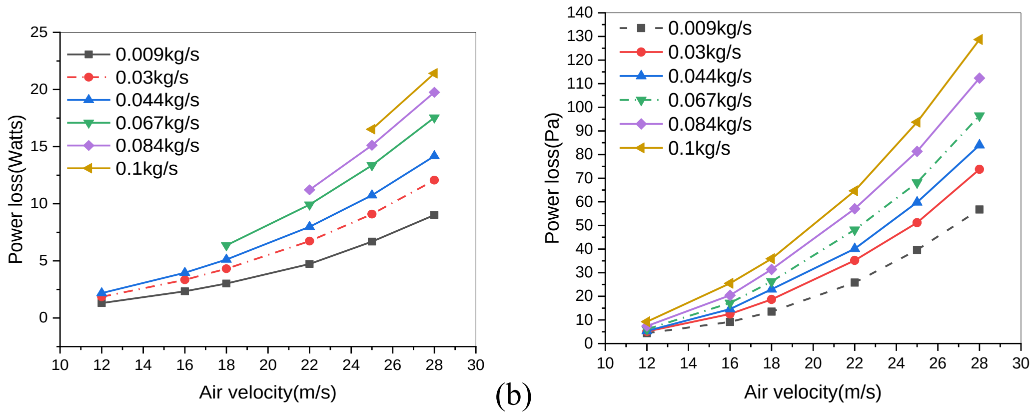

(a) (b)

Figure 4.26. Power loss due to (a) bend and (b) cyclone separator

The results show the effect of increasing inlet air velocity within the range of 12 to 28 m/s, with a material flow rate of 0.009 to 0.1 kg/s and pipe diameters ranging from 46 to 71 mm across various system components, including the feeder, horizontal and vertical pipelines, 90° bends, and the cyclone separator. Figure 4.31 power loss vs. inlet air velocity (a) at v = 12-28 m/s, material flow rate m_s = 0.009 - 0.1 kg/s and diameter D = 46 mm for feeder and (b) v = 12 - 28 m/s, material flow rate m_s = 0.009 - 0.1 kg/s and D = 46 mm and L = 6000 mm for horizontal and vertical pipe illustrate the relationship between inlet air velocity and power loss in a positive-pressure dilute-phase pneumatic teff grain conveying system.

Figure 4.32 power loss vs. inlet air velocity at (a) v = 12 - 28 m/s, material flow rate m_s= 0.009 - 0.1 kg/s and D = 46 mm for bends (b) v = 12-28 m/s, material flow rate m_s = 0.009 - 0.1 kg/s and D = 150 mm for cyclone separator. Pressure drop across the full system was shown in Figure 4.33. For a 46 mm diameter pipeline, the total length was 22.73 m, comprising an 18 m horizontal section, a 3 m vertical section, and an equivalent length of 1.73 m of bends. For a 71 mm diameter pipeline, the total length was 23.67 m, including 18 m horizontal, 3 m vertical, and an equivalent length of 2.67 m of bends.

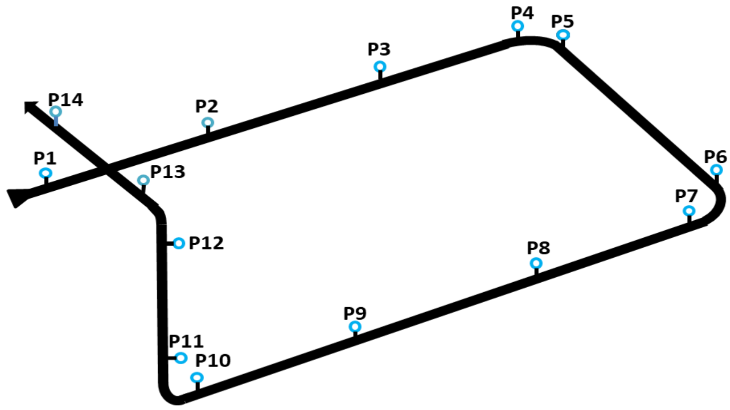

Figure 4.27. The profile of pneumatic teff grain conveying system

Table 4.13. Pressure drop for D = 46 mm and L= 22.73 m

Inlet air velocity (m/s)	Pressure drop(Pa) for D = 46 mm, L= 22.73 m					
	Material flow rate					
	0.009(kg/s)	0.03(kg/s)	0.044(kg/s)	0.067(kg/s)	0.084(kg/s)	0.1(kg/s)
12	2563	4104	5023	-	-	-
16	3073	4433	5710	-	-	-
18	3079	4781	5540	7308	-	-
22	3463	5212	5980	7332	8521	10171
25	4039	5274	6350	7821	8562	9490
28	4210	5845	6335	8263	9080	9757

Table 4.14. Pressure drop for D = 71 mm and L= 23.67 m

Inlet air velocity (m/s)	Pressure drop(Pa) for D = 71 mm, L= 23.67 m					
	Material flow rate					
	0.009(kg/s)	0.03(kg/s)	0.044(kg/s)	0.067(kg/s)	0.084(kg/s)	0.1(kg/s)
16	1652	2145	2383	2859	3250	3602
18	1750	2210	2496	2959	3172	3499
22	2025	2590	2880	3237	3463	3786
25	2348	2821	2852	3308	3639	3785
28	2644	2801	3093	3520	3682	4022

Table 4.13 shows that the results show that pressure drop increases with air velocity and material flow rate. In the 46 mm pipe, it ranges from 2563 Pa at 12 m/s (0.009 kg/s) to 9757 Pa at 28 m/s (0.1 kg/s). Tables 4.14 highlight that the 71 mm pipe exhibits lower pressure drops, 1652 Pa at 16 m/s (0.009 kg/s) and a maximum of 4022 Pa at 28 m/s (0.1 kg/s). These findings highlight that increasing air velocity and material flow rate result in a higher pressure drop, but using a larger pipe diameter significantly reduces energy losses.

Selecting an appropriate pipe diameter and operating conditions was crucial for optimizing the energy efficiency of pneumatic conveying systems.

4.2.9. Power requirements

The total power requirement of the pneumatic conveying system was calculated based on the overall pressure drop that occurs as the conveying air and particles move through different components. These include the feeder, horizontal and vertical pipelines, 90° bends, and the cyclone separator. Each component contributes to the total resistance depending on factors such as air velocity, pipe diameter, pipe length, and solid loading ratio. The total pressure drop was obtained by summing the individual losses across all system components, which reflects the overall resistance encountered by the conveying airflow and particles. Accurate estimation of these pressure drops was essential for determining the energy needed to operate the system efficiently.

Once the total pressure drop was known, the system power requirement was determined by multiplying it by the volumetric airflow rate at the inlet of the conveying line. This value represents the energy necessary to overcome flow resistance and maintain continuous material transport. Figure 4.28 presents a summary of the calculated power requirements under different operating conditions.

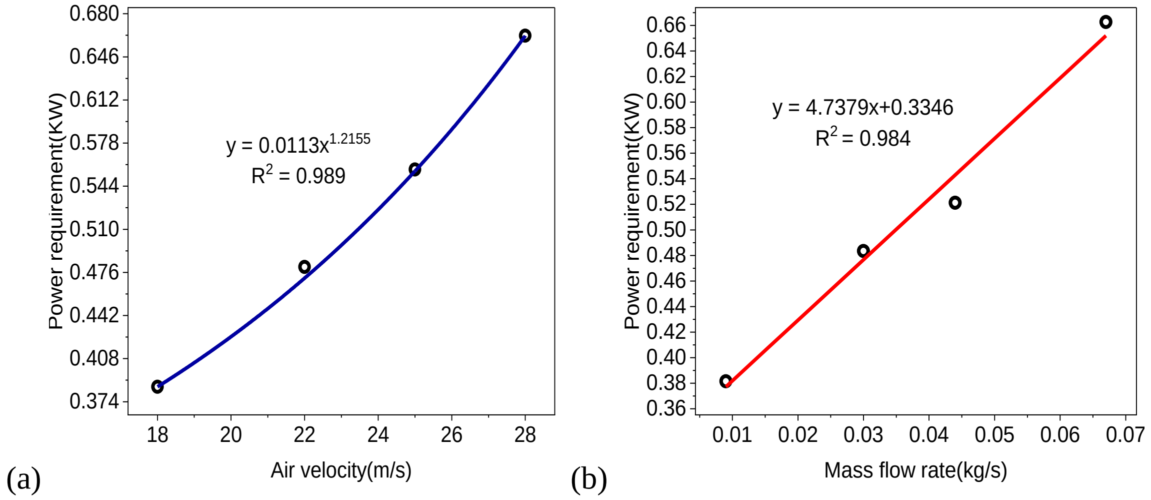

Figure 4.28. Power required for D = 46 mm

Figure 4.28 highlights that power required: Figure 4.28 (a) D = 46 mm, v = 18 - 28 m/s, m_s = 0.067 kg/s, and η = 0.7, and Figure 4.28 (b) power required for D = 46 mm, m_s = 0.009 kg/s - 0.067 kg/s, v = 28 m/s, and η = 0.7.

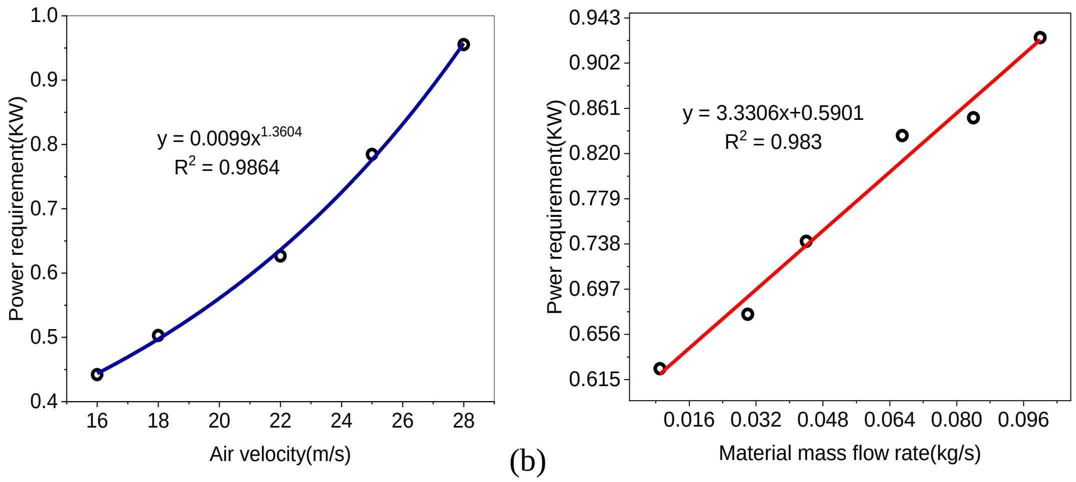

(a) (b)

Figure 4.29. Power required for D = 71 mm

Figure 4.29 indicates the power required: Figure 4.29 (a) D = 71 mm, v = 16-28 m/s, m_s = 0.1 kg/s, and η = 0.7 and Figure 4.29 (b) power required for D = 71 mm, m_s = 0.0009 kg/s - 0.1 kg/s, v = 28m/s, and η = 0.7.

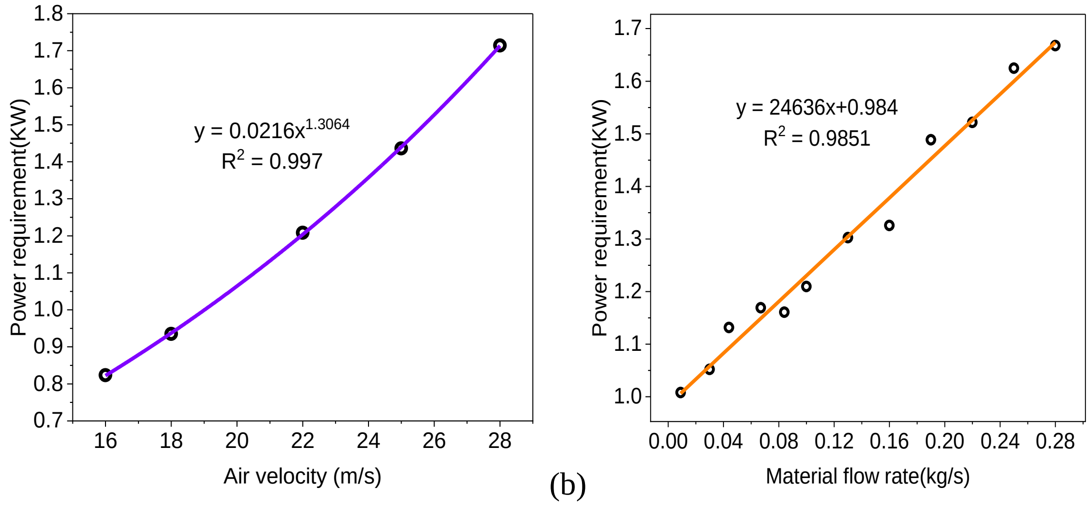

(a) (b)

Figure 4.30. Power required for D = 102 mm

Figure 4.30 indicates that the power required: Figure 4.30 (a) D = 102 mm, v = 16-28 m/s, m_s = 0.28 kg/s, and η = 0.7, Figure 4.30 (b) power required for D = 102 mm, m_s = 0.009 kg/s - 0.28 kg/s, v = 28 m/s, and η = 0.7.

Figures 4.28-4.30 illustrate that the power requirement for the system was directly dependent on the airflow rate, material flow rate, pipe size, and total pressure drop in the system. As airflow rate and material flow rate increase, and for smaller pipe sizes, pressure drop increases, and energy required also increases, and vice versa for the same operating condition. Therefore, optimizing system parameters was a key consideration in the design of an energy-efficient pneumatic conveyor system for teff grain.

4.3. Results and discussions on artificial neural network model

4.3.1. Size of data for ANN model

The application of an artificial neural network demonstrated significant advantages over traditional statistical models for predicting pressure drop in the pneumatic conveying system. The ANN proved capable of accurately capturing the complex, non-linear relationships between the independent variables air velocity, material flow rate, pipe diameter, cyclone diameter, pipe length, and pipe layout, and the dependent variable of pressure drop. This superior performance was consistent with previous findings (Alizadehdakhel et al., 2009; Zhao & Su, 2010; Ghode et al., 2017; Jardon et al., 2019; Shadloo et al., 2020; Haghighi et al., 2020) and was further validated through direct comparison with regression models. As evidenced in APPENDIX D and APPENDIX E, the nonlinear multiple regression models demonstrated substantially poorer accuracy compared to the full ANN model, confirming the ANN's enhanced capability in modeling the intricate dynamics of pneumatic teff grain conveyance.

Table 4.15. Data size for ANN model

Components	Laboratory test results	CFD-DPM simulation result	Total
Feeder	245	283	528
Horizontal pipe	249	465	714
Vertical pipe	176	472	648
Bends	240	480	720
Cyclone separator	248	292	540
Total	1158	1992	3150
Percentage (%)	36.76	63.24	100

Table 4.15 presents the data size used for an ANN model, categorizing it into experimental (laboratory results) and CFD-DPM Simulation data. The total dataset consists of 3,150 data points, with 1,158 (36.76%) from experiments and 1,992 (63.24%) from simulations. Data was distributed across different components: the feeder has 528 data points (245 experimental, 283 simulations), the horizontal pipe has 714 (249 experimental, 465 simulations), the vertical pipe has 648 (176 experimental, 472 simulations), the bends have 720 (240 experimental, 480 simulations), and the cyclone separator has 540 (248 experimental, 292 simulations). CFD-DPM simulation contributes more data than

experimental results due to its flexibility, higher level of detail compared to experiments, and its role in enhancing the robustness and generalizability of the ANN model.

4.3.2. K-Fold cross-validation

K-Fold cross-validation was performed using the metrics such as R-squared, MSE, RMSE, MAE, and MAPE for K = 6 and n = 10. This validation was applied to the feeder, horizontal pipelines, vertical pipelines, 90° bends, and cyclone separators to evaluate model performance and generalization.

Table 4.16. K-Fold cross-validation metrics of feeder for (K = 6 and n = 10)

Evaluation metrics	Fold 1	Fold 2	Fold 3	Fold 4	Fold 5	Fold 6	Average
R-squared	0.9891	0.9907	0.9935	0.9901	0.9795	0.9879	0.9884
MSE	2406.58	1814.24	1357.02	1813.85	2989.53	2251.01	2105.37
RMSE	49.0570	42.5939	36.8378	42.5894	54.6766	47.4449	45.5333
MAE	37.892	33.9712	29.3039	33.2290	43.6332	36.1580	35.6980
MAPE	9.2228	7.6727	6.6583	6.8618	10.2480	7.8364	8.0834

Table 4.16 presents the K-Fold cross-validation results of the ANN model for the feeder component using K = 6 and n = 10. Metrics include R^2, MSE, RMSE, MAE, and MAPE, which evaluate the model's predictive consistency across multiple validation folds in Table 3.4 (Akoglu, 2018; Hange et al., 2020; Jierula et al., 2021).

The ANN model demonstrates consistent predictive performance across all folds. R^2 values range from 0.9795 to 0.9935, with an average of 0.9884, indicating a very strong fit between predicted and actual pressure drop values. This confirms that the model generalizes well across different subsets of the data.

Error metrics further support the model's reliability. MSE values range from 1357.02 to 2989.53 Pa^2, reflecting moderate absolute prediction errors across folds. RMSE values vary between 36.84 Pa and 54.68 Pa, demonstrating reasonable deviations from the observed data. MAE values range from 29.30 Pa to 43.63 Pa, indicating fairly low average errors, while MAPE ranges from 6.66% to 10.25%, suggesting the model maintains good proportional accuracy across folds.

Overall, the K-Fold cross-validation confirms that the ANN model for the feeder was robust and reliable, with low to moderate absolute and relative errors. The consistency of R^2 and error metrics across folds demonstrates that the model can effectively predict feeder pressure drops under varying data subsets, reinforcing its suitability for practical applications in pneumatic conveyor system design and optimization.

Table 4.17. K-Fold cross-validation metrics of horizontal pipe for (K = 6 and n = 10)

Evaluation metrics	Fold 1	Fold 2	Fold 3	Fold 4	Fold 5	Fold 6	Average
R-squared	0.9611	0.9471	0.9774	0.9713	0.8931	0.9689	0.9532
MSE	11630.67	11284.88	5395.14	6576.20	23800.59	9387.28	11345.7
RMSE	107.8456	106.2303	73.4517	81.0938	154.2744	96.8880	103.297
MAE	69.9476	81.6370	52.1029	54.6237	119.5923	70.1089	74.6687
MAPE	11.0982	18.8553	10.4561	10.2994	27.9275	12.2097	15.1411

Table 4.17 summarizes the K-Fold cross-validation metrics for the ANN model predicting pressure drops in horizontal pipes, with K = 6 and n = 10. Metrics include R^2, MSE, RMSE, MAE, and MAPE, which collectively assess the model's consistency and predictive accuracy across multiple folds was as shown in Table 3.4 (Akoglu, 2018; Hange et al., 2020; Jierula et al., 2021).

The ANN model demonstrates moderate variability in predictive performance across folds. R^2 values range from 0.8931 to 0.9774, with an average of 0.9532, indicating a fairly strong fit overall but reduced consistency compared to the feeder component. This variability suggests that certain data subsets may be more challenging for the model, potentially due to variations in material flow or local turbulence effects in horizontal pipelines.

Error metrics reflect this variation. MSE spans from 5395.14 Pa^2 to 23800.59 Pa^2, with RMSE ranging from 73.45 Pa to 154.27 Pa, showing that some folds exhibit significantly larger deviations from the observed data. MAE values vary between 52.10 Pa and 119.59 Pa, while MAPE ranges from 10.46% to 27.93%, indicating that proportional accuracy was less stable compared to the feeder.

Cross-validation for horizontal pipes shows a generally good fit, but with higher variability and errors than the feeder, highlighting challenges in modeling pressure drops and the potential need for improved feature engineering or model tuning.

Table 4.18. K-Fold cross-validation metrics of vertical pipe for (K = 6 and n = 10)

Evaluation metrics	Fold 1	Fold 2	Fold 3	Fold 4	Fold 5	Fold 6	Average
R-squared	0.9766	0.9885	0.9886	0.9661	0.9642	0.9728	0.9761
MSE	5338.79	4054.36	3465.50	7757.88	7557.12	9986.59	6360.04
RMSE	73.0671	63.6739	58.8686	88.0788	86.9317	99.9330	78.4255
MAE	52.2277	48.3086	46.5679	68.1661	67.2827	69.3615	58.6524
MAPE	12.9783	17.3946	10.6120	12.9865	15.7130	14.4268	14.0185

Table 4.18 presents the K-Fold cross-validation results for the ANN model predicting pressure drops in vertical pipes with K = 6 and n = 10. Metrics include R^2, MSE, RMSE,

MAE, and MAPE, which collectively evaluate model consistency and predictive accuracy across multiple folds as highlighted in Table 3.4 (Akoglu, 2018; Hange et al., 2020; Jierula et al., 2021).

The model demonstrates strong predictive performance across all folds. R^2 values range from 0.9642 to 0.9886, with an average of 0.9761, indicating that the model effectively captures the variance in experimental data and provides a strong fit for vertical pipeline pressure drops.

Error metrics show moderate absolute deviations. MSE ranges from 3465.50 Pa^2 to 9986.59 Pa^2, while RMSE varies between 58.87 Pa and 99.93 Pa, reflecting reasonable differences between predicted and observed values. MAE values, ranging from 46.57 Pa to 69.36 Pa, indicate fairly low average errors, and MAPE values vary from 10.61% to 17.39%, demonstrating good proportional accuracy across folds.

Overall, the cross-validation results indicate that the ANN model for vertical pipes was reliable and accurate. The model maintains strong predictive power and consistent performance, even with varying data subsets, highlighting its suitability for modeling vertical flow sections in pneumatic conveyor systems.

Table 4.19. K-Fold cross-validation metrics of bends for (K = 6 and n = 10)

Evaluation metrics	Fold 1	Fold 2	Fold 3	Fold 4	Fold 5	Average
R-squared	0.9567	0.9438	0.9606	0.9357	0.9637	0.9521
MSE	695.053	822.63	759.60	986.65	725.60	797.91
RMSE	26.3639	28.6817	27.5609	31.4110	26.9371	28.1909
MAE	17.9154	18.3707	18.0400	20.5225	17.9942	18.5686
MAPE	13.5950	12.2889	11.2634	13.3343	12.1628	12.5289

Table 4.19 presents the K-Fold cross-validation metrics for the ANN model predicting pressure drops across 90° bends, with K = 6 and n = 10. Metrics include R^2, MSE, RMSE, MAE, and MAPE, which collectively assess the model's accuracy and consistency across multiple validation folds as indicated in Table 3.4 (Akoglu, 2018; Hange et al., 2020; Jierula et al., 2021).

The model demonstrates a fairly strong fit across folds, with R^2 values ranging from 0.9357 to 0.9637 and an average of 0.9521. Although slightly lower than other system components, these values indicate that the ANN effectively captures the pressure drop behavior in curved flow sections.

Error metrics were relatively consistent across folds. MSE ranges from 695.05 Pa^2 to 986.65 Pa^2, while RMSE values range from 26.36 Pa to 31.41 Pa, reflecting reasonably small deviations from observed data. MAE values vary from 17.92 Pa to 20.52 Pa, and MAPE ranges from 11.26% to 13.59%, showing that the model maintains good proportional accuracy even in curved pipe sections where flow dynamics were more complex.

K-Fold validation confirms that the ANN model for 90° bends was reliable and provides reasonable predictive accuracy. Despite the slightly lower R^2 compared to other components, the error metrics indicate that the model can effectively predict pressure drops in bends, supporting its use for practical applications in pneumatic conveyor design.

Table 4.20. K-Fold cross-validation metrics of cyclone separator for (K = 6 and n = 10)

Evaluation metrics	Fold 1	Fold 2	Fold 3	Fold 4	Fold 5	Average
R-squared	0.9675	0.9566	0.9493	0.9710	0.9406	0.9570
MSE	5245.32	6330.11	7983.04	3779.43	6513.14	5970.21
RMSE	72.4246	79.5620	89.3479	61.4771	80.7041	76.7031
MAE	57.4013	62.0486	64.5142	44.3110	67.8268	59.2204
MAPE	9.6482	16.3478	10.2761	8.2392	27.6522	14.4327

Table 4.20 presents the K-Fold cross-validation results for the ANN model predicting pressure drops in the cyclone separator, with K = 6 and n = 10. The table includes R^2, MSE, RMSE, MAE, and MAPE, which collectively assess the consistency and accuracy of the model across multiple validation folds as shown in Table 3.4 (Akoglu, 2018; Hange et al., 2020; Jierula et al., 2021).

The ANN model demonstrates a reasonably strong fit, with R^2 values ranging from 0.9406 to 0.9710 and an average of 0.9570, indicating that the model captures the main patterns in cyclone separator pressure drop data. Error metrics vary across folds: MSE ranges from 3779.43 Pa^2 to 7983.04 Pa^2, RMSE from 61.48 Pa to 89.35 Pa, MAE from 44.31 Pa to 67.83 Pa, and MAPE from 8.24% to 27.65%. The larger spread in MAPE values suggests that the model's relative accuracy was less consistent in some folds, likely due to the complex swirling flow and particle separation mechanisms inherent to the cyclone separator.

Across all system components, the neural network model demonstrates generally strong performance. The feeder exhibits the highest consistency, with high R^2 values and low errors, whereas the horizontal pipelines and cyclone separator show greater variability, indicating slightly less stable predictive performance for these components.

The K-Fold cross-validation analysis confirms that the ANN model demonstrates robust predictive performance across all components of the pneumatic teff grain conveying system, including the feeder, horizontal and vertical pipelines, 90° bends, and cyclone separator. The feeder exhibited the most consistent predictions, with high R^2 values (0.9795–0.9935) and low error metrics (MSE, RMSE, MAE, and MAPE), indicating excellent model generalization across folds. Vertical pipelines and 90° bends also showed strong predictive capabilities, with average R^2 values of 0.9761 and 0.9521, respectively, and moderate absolute and relative errors, highlighting reliable performance even under varying flow conditions.

Horizontal pipelines and the cyclone separator displayed slightly higher variability in errors and lower consistency in proportional accuracy (R^2 averages of 0.9532 and 0.9570, respectively), likely due to more complex flow dynamics, turbulence, and particle separation effects. Despite these variations, the model maintained overall strong predictive power and reasonable error magnitudes, demonstrating its suitability for practical applications.

Overall, the K-Fold cross-validation confirms that the ANN model was robust, reliable, and capable of generalizing across different data subsets, making it effective for accurately predicting pressure drops in all major components of the pneumatic conveyor system.

4.3.3. Hyperparameter tuning of neural network fitting

Hyperparameter tuning of neural network fitting was carried out by carefully assessing key parameters such as fold number, number of neurons, and R-squared values through detailed contour plots. These visualizations allowed for a systematic evaluation of how changes in network architecture and training configurations influenced model performance. Additionally, data splitting strategies, neuron count variations, and R-squared trends were analyzed for different components of the pneumatic teff grain conveying system, including the feeder, horizontal and vertical pipelines, 90° bends, and cyclone separators. By examining each component individually, the study ensured that the model could capture the distinct behaviors and dynamics associated with different sections of the conveying system.

The primary goal of this parameter tuning process was to determine the ideal combination of neuron numbers and data split sizes to maximize the neural network's predictive accuracy. Fine-tuning these parameters enabled the model to more effectively learn the complex relationships between input variables such as air velocity, material flow rate, and system geometry, thereby enhancing its ability to simulate pressure drop and airflow characteristics accurately. These adjustments not only improved the overall performance of the model but also ensured that predictions remained reliable and consistent across different operating conditions and system components, providing a robust model for designing and optimizing pneumatic conveying of teff grain.

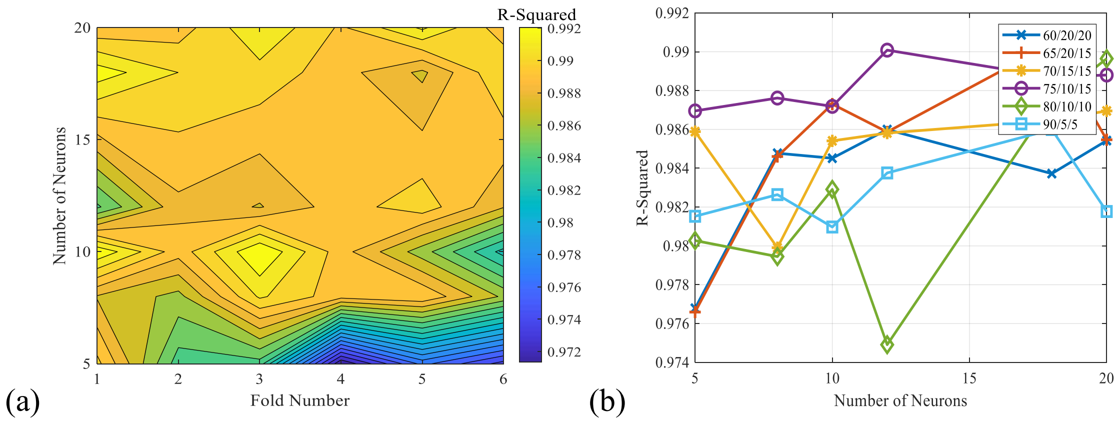

Figure 4.31. The optimum number of neurons and data split size for feeder

For the feeder model shown in Figure 4.31(a) and Figure 4.31(b), the hyperparameter configuration for the neural network was determined to be 10 neurons (n = 10) and a 3-fold cross-validation (K = 3). This configuration yielded the highest R-squared value when using a 75/10/15 data split for training, validation, and testing, respectively. Therefore, to maximize model accuracy and ensure good generalization, the neural network fitting model was implemented with n = 10 and the specified 75/10/15 data split.

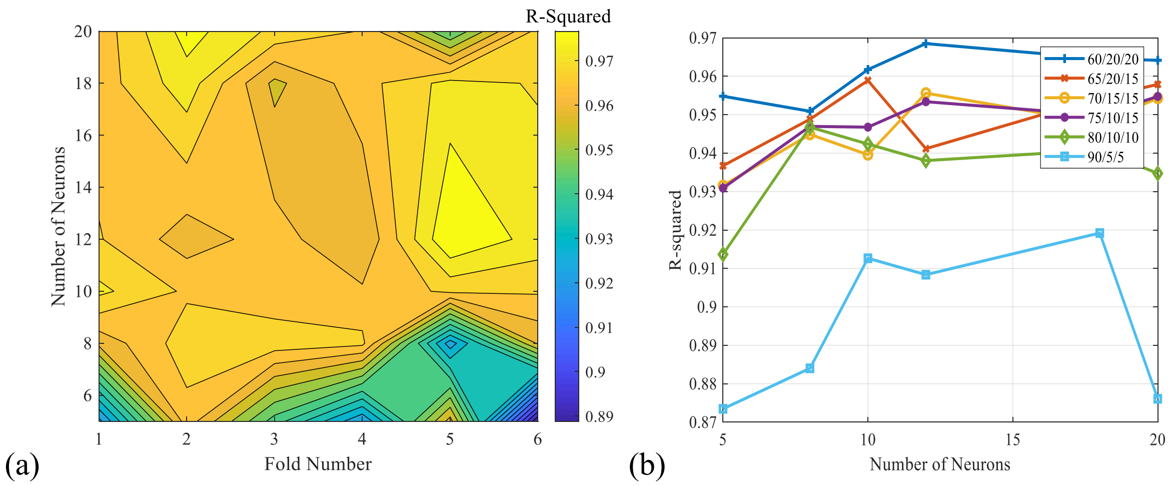

Figure 4.32. The optimum number of neurons and data split size for horizontal pipe

For the horizontal pipe model shown in Figure 4.32(a) and Figure 4.32(b), the hyperparameter configuration for the neural network was determined to be 12 neurons (n = 12) and a 5-fold cross-validation (K = 5). This configuration yielded the highest R-squared value when using a 60/20/20 data split for training, validation, and testing, respectively. Therefore, to maximize model accuracy and ensure good generalization, the neural network fitting model was implemented with n = 12 and the specified 60/20/20 data split.

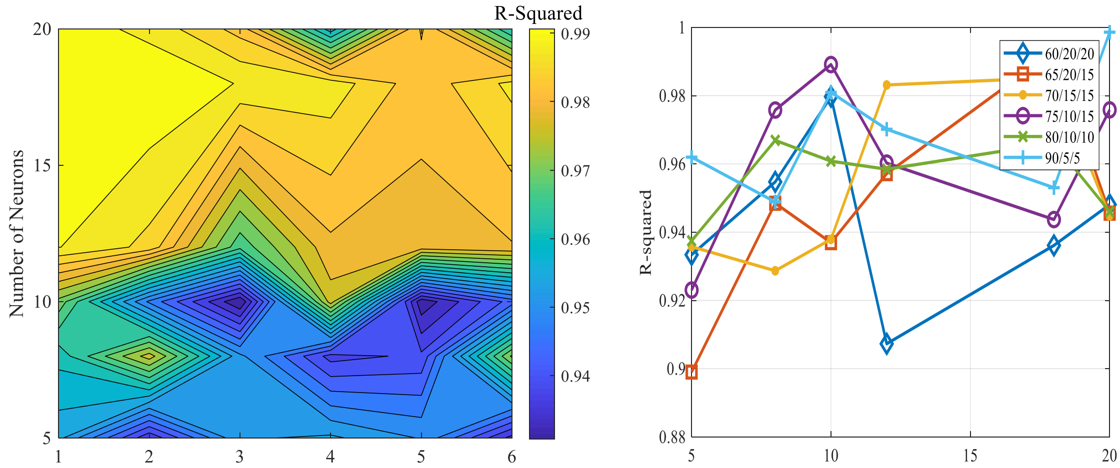

(a) (b)

Figure 4.33. The optimum number of neurons and data split size for vertical pipe

For the vertical pipe model shown in Figure 4.33(a) and Figure 4.33(b), the hyperparameter configuration for the neural network was determined to be 18 neurons (n = 18) and a 1-fold cross-validation (K = 1). This configuration yielded the highest R-squared value when using a 90/5/5 data split for training, validation, and testing, respectively. Therefore, to maximize model accuracy and ensure good generalization, the neural network fitting model was implemented with n = 18 and the specified 90/5/5 data split.

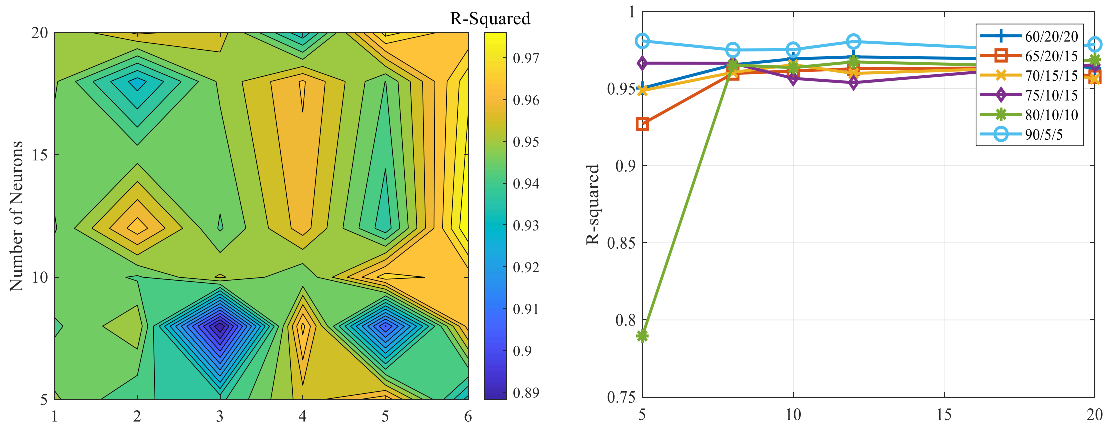

(a) (b)

Figure 4.34. The optimum number of neurons and data split size for bends

For the 90° bends model shown in Figure 4.34(a) and Figure 4.34(b), the hyperparameter configuration for the neural network was determined to be 12 neurons (n = 12) and a 6-fold cross-validation (K = 6). This configuration yielded the highest R-squared value when using a 90/5/5 data split for training, validation, and testing, respectively. Therefore, to maximize model accuracy and ensure good generalization, the neural network fitting model was implemented with n = 12 and the specified 90/5/5 data split.

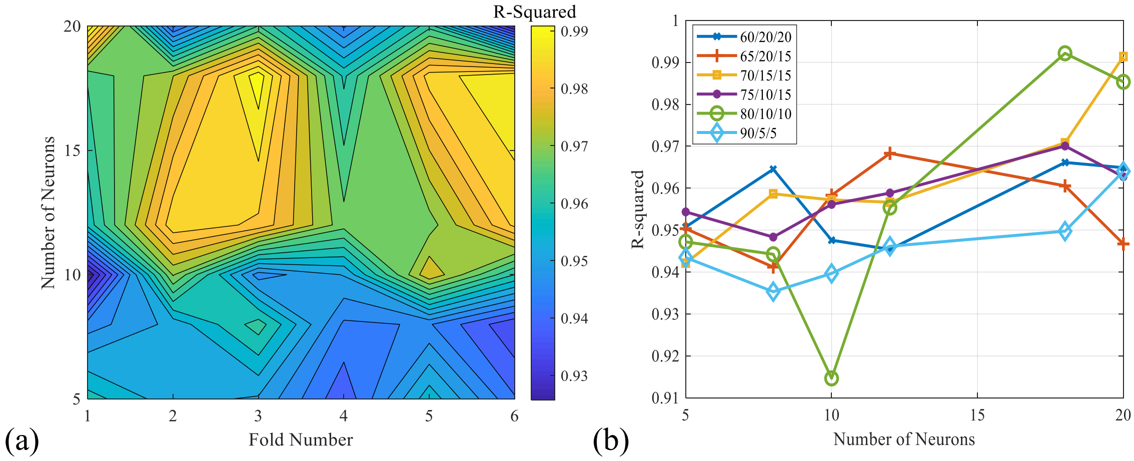

Figure 4.35. The optimum number of neurons and data split size for cyclone separator

For the cyclone separator model shown in Figure 4.35(a) and Figure 4.35(b), the hyperparameter configuration for the neural network was determined to be 18 neurons (n = 18) and a 3-fold cross-validation (K = 3). This configuration yielded the highest R-squared value when using an 80/10/10 data split for training, validation, and testing, respectively. Therefore, to maximize model accuracy and ensure good generalization, the neural network fitting model was implemented with n = 18 and the specified 80/10/10 data split.

Table 4.21. ANN neurons and data split for system components

System component	Number of neurons	Dataset split
Feeder	10	75/10/15
Horizontal pipes	10	60/20/20
Vertical pipes	10	75/10/15
90° Bends	10	90/05/05
Cyclone separator	10	65/20/15

Table 4.21 summarizes the ANN configurations for different system components: feeder (75/10/15), horizontal pipes (60/20/20), vertical pipes (75/10/15), 90° bends (90/5/5), and cyclone separator (65/20/15). Each component used 10 hidden neurons, balancing model complexity with data size (528-714 samples) based on the 10× parameters rule (Alwosheel et al., 2018). Varying data splits optimized training, validation, and generalizability. The Levenberg-Marquardt algorithm was selected for its efficiency and adaptability. In

MATLAB’s nntool, the correlation coefficient was shown as (R) in figures but interpreted as (r).

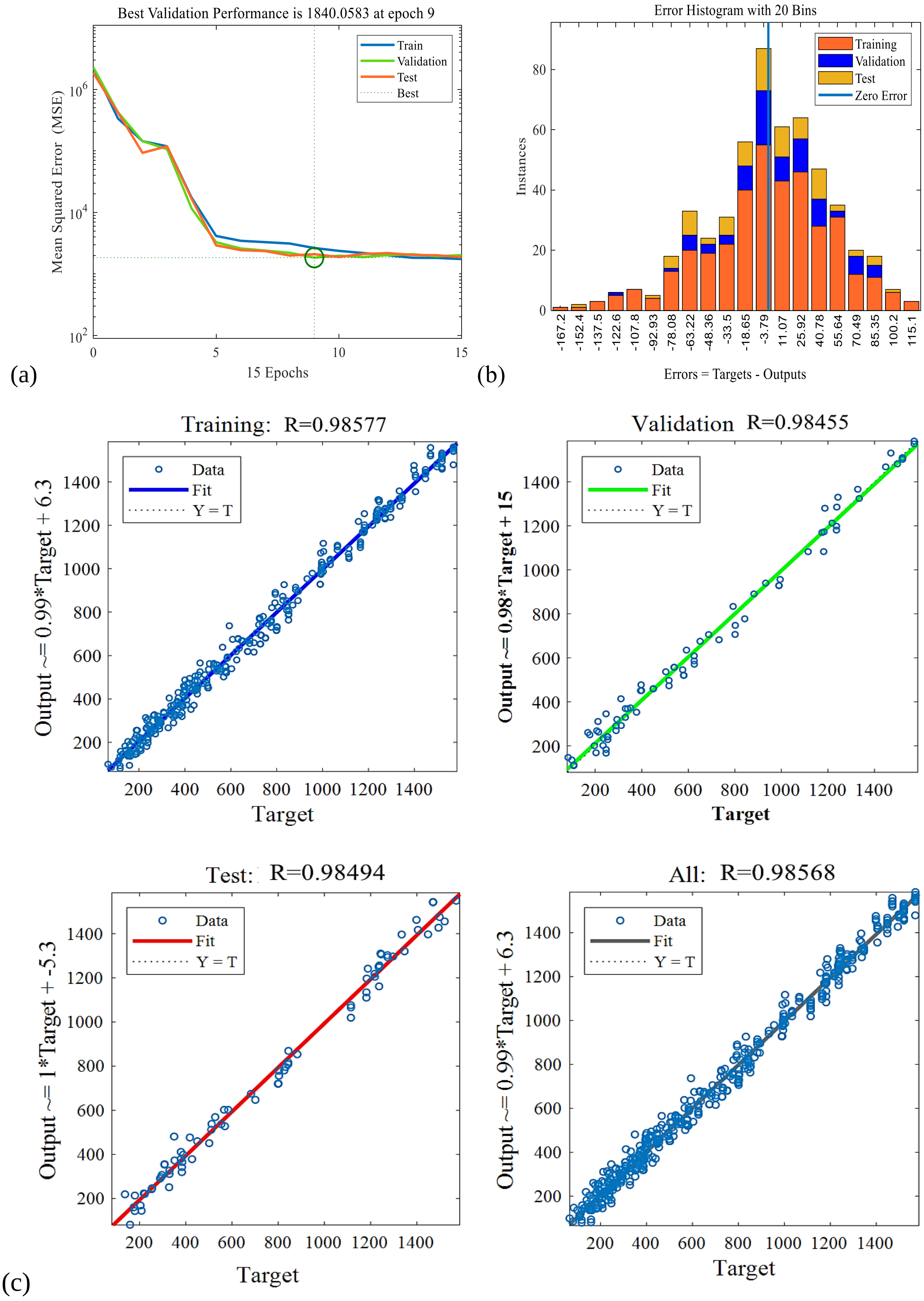

Figure 4.36. ANN model for feeder

In Figure 4.36(a-c), for a feeder with diameters of 46, 71, and 102 mm, velocities of 12-28 m/s, and mass flow rates of 0.009-0.28 kg/s, the ANN model achieved its best validation with an MSE of 1840.06 at epoch 9. The model showed excellent fit with training r = 0.98577, validation r = 0.98455, test r = 0.98494, and overall r = 0.98568, indicating accurate pressure drop predictions. The error histogram ranged from -167.2 to 115.1, reflecting minimal deviation between predicted and actual values.

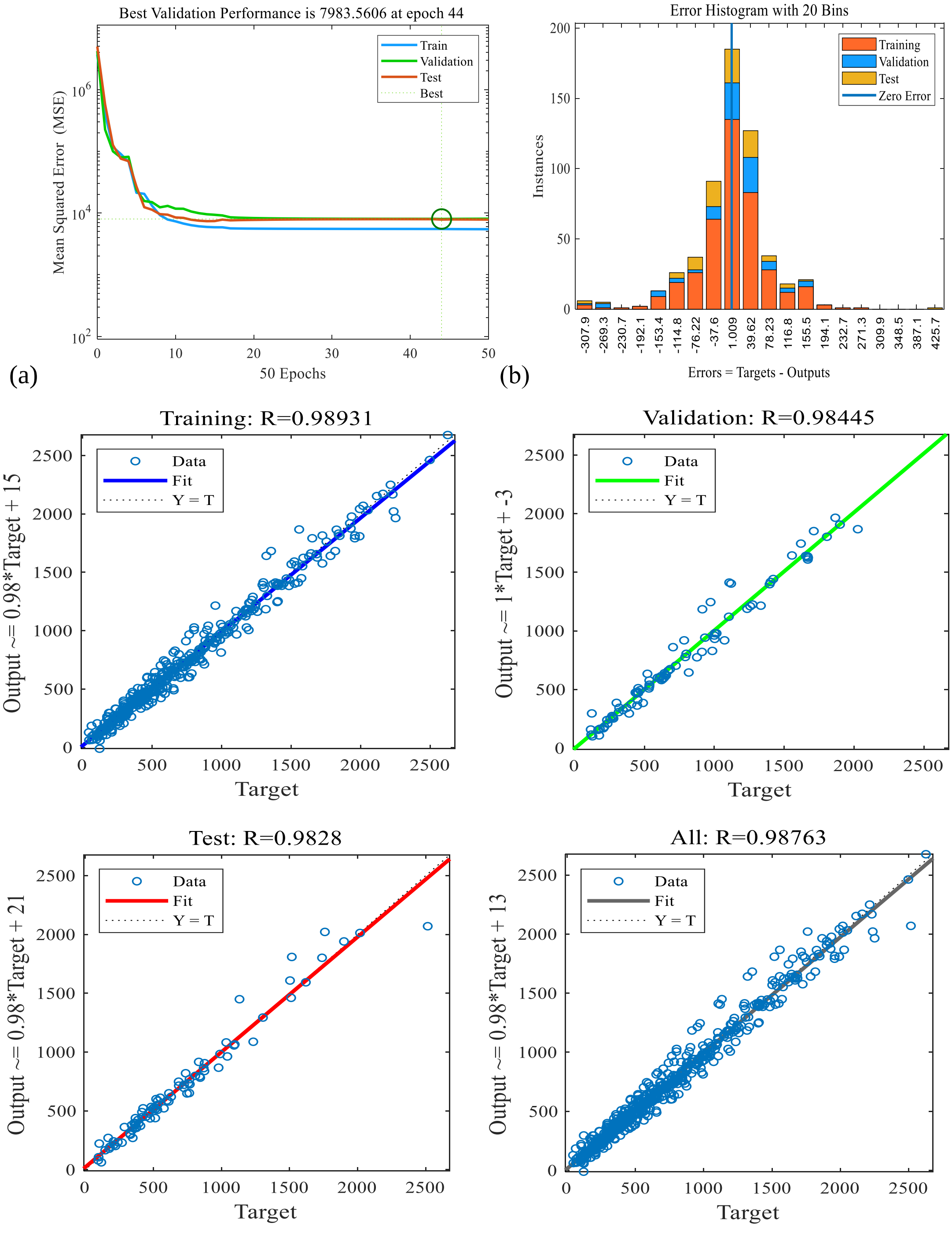

Figure 4.37. ANN model for horizontal pipe

Figure 4.37(a-c) shows horizontal pipelines with diameters of 46, 71, and 102 mm, lengths of 2000, 4000, and 6000 mm, velocities of 12-28 m/s, and mass flow rates of 0.009-0.28 kg/s. The best validation occurred at epoch 44 with an MSE of 7983.56. While slightly less optimal than the feeder, the model still performed well with training r = 0.98931, validation r = 0.98445, test r = 0.9828, and overall r = 0.98763. The error histogram ranged from -307.9 to 425.7, showing a wider spread but acceptable prediction accuracy, capturing the horizontal pipeline's behavior effectively.

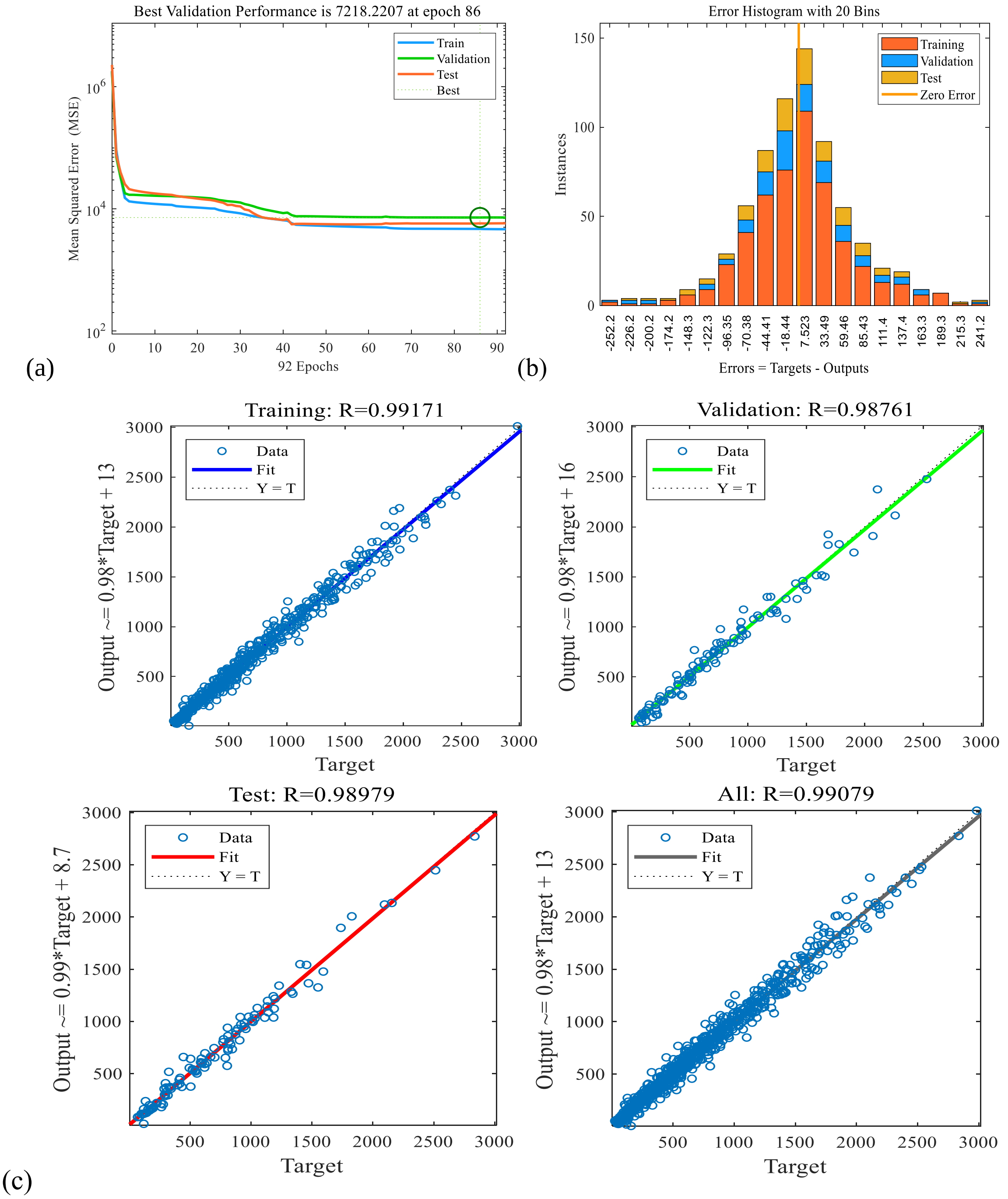

Figure 4.38. ANN model for vertical pipe

Figure 4.38(a-c) shows vertical pipelines with diameters of 46, 71, and 102 mm, lengths of 2000, 4000, and 6000 mm, velocities of 12-28 m/s, and mass flow rates of 0.009-0.28 kg/s. Over 92 epochs, the best validation occurred at epoch 86 with an MSE of 7218.22. r-values were slightly lower than other components training r = 0.99171, validation r = 0.98761, test r = 0.98979, and overall r = 0.99079 but still indicated strong predictive accuracy. The error histogram ranged from -252.2 to 241.2, showing small deviations and effective pressure drop prediction for the vertical pipeline.

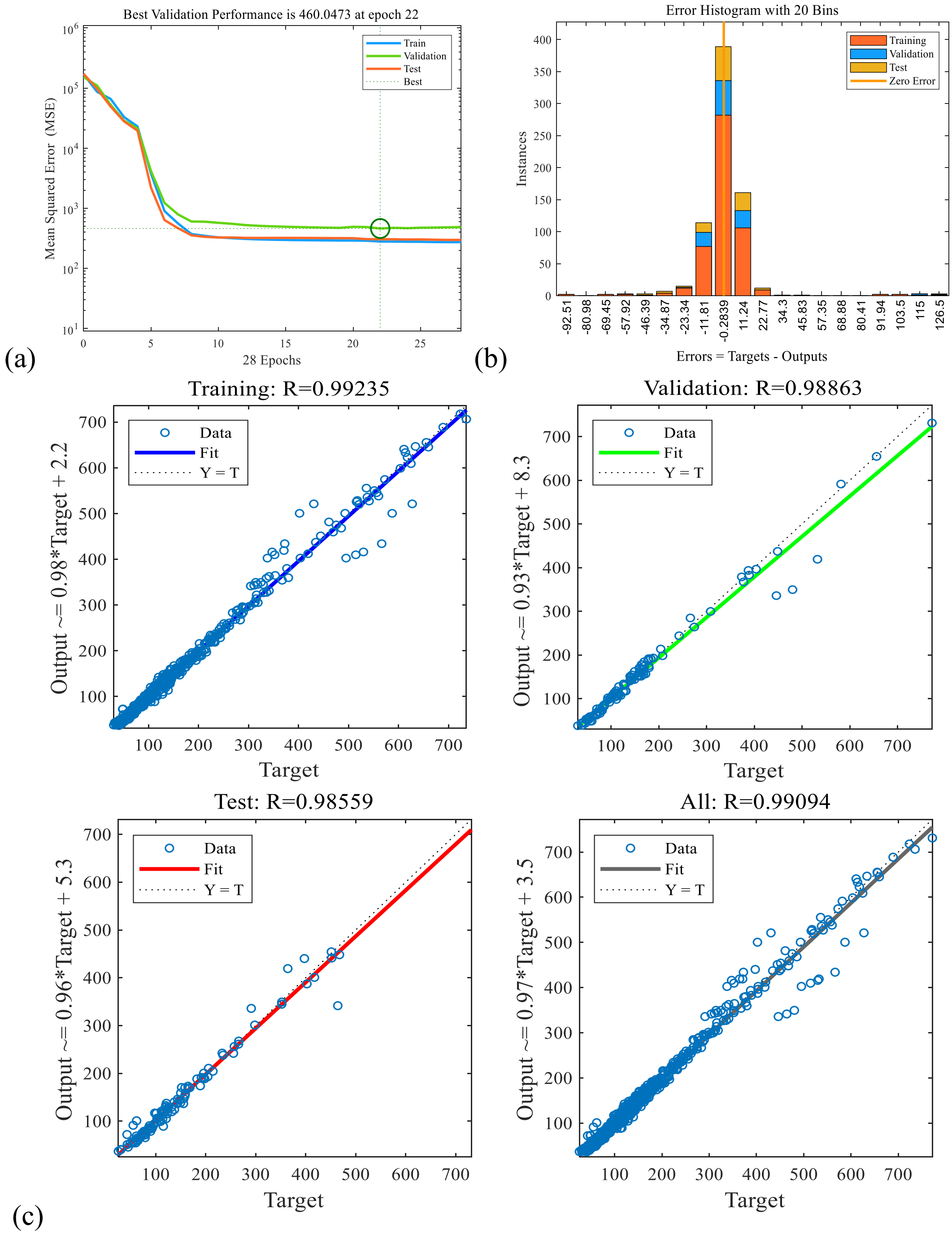

Figure 4.39. ANN model for bends

Figure 4.39(a-c) shows 90° bends with diameters of 46 and 71 mm, layouts H-H, H-V UP, V-H LEFT, H-V DOWN, V-H RIGHT, velocities of 12-28 m/s, and mass flow rates of 0.009-0.28 kg/s. After 28 epochs, the best validation occurred at epoch 22 with an MSE of 460.05. The model showed excellent fit with training r = 0.99235, validation r = 0.98863, test r = 0.98559, and overall r = 0.99094. The error histogram ranged from -92.51 to 126.5, confirming minimal deviation and high predictive accuracy for pressure drop across the bends.

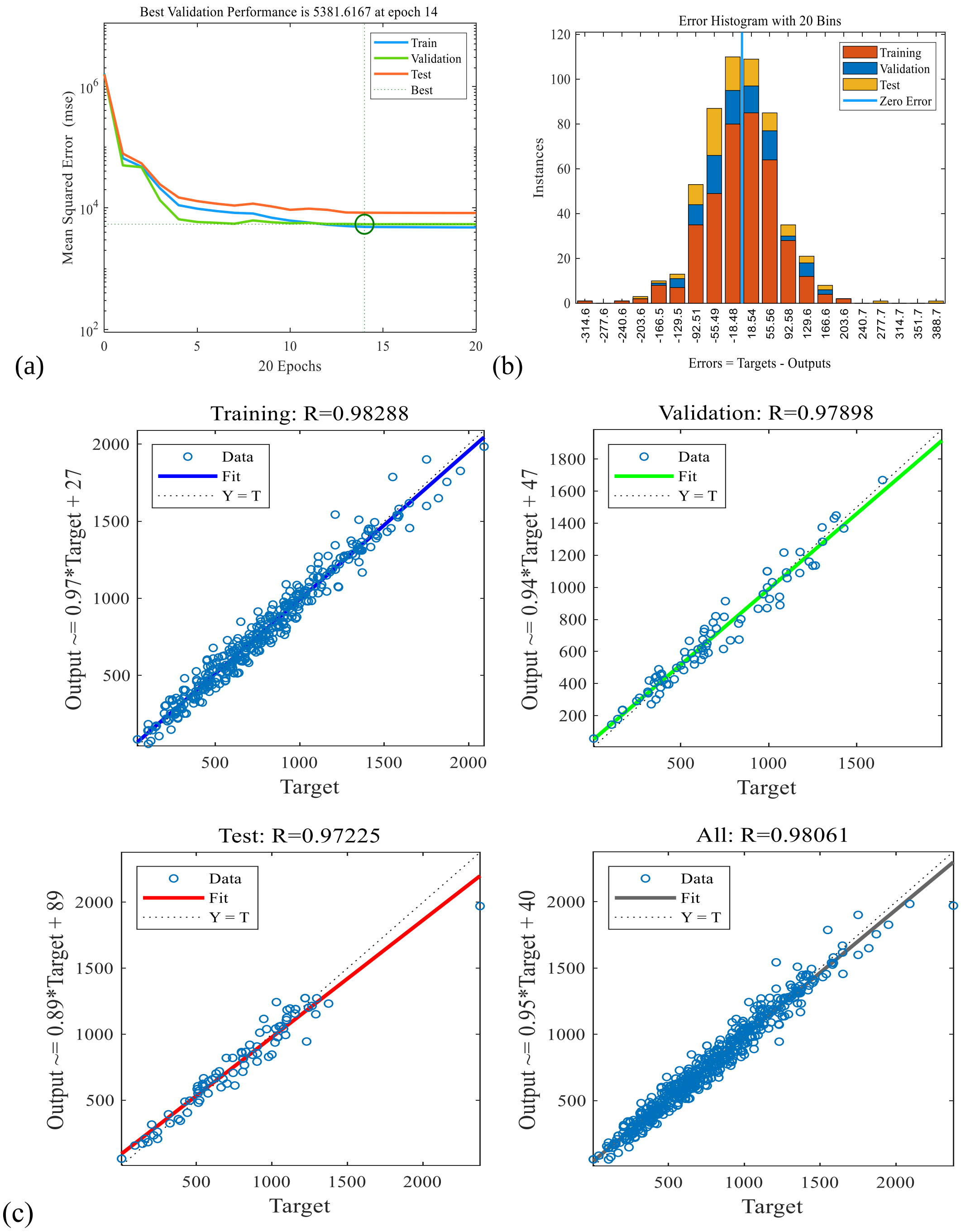

Figure 4.40. ANN model for cyclone separator

Lastly, Figure 4.40(a-c) illustrates the performance of the cyclone separator at cyclone diameter (D) = 150 mm, 180 mm, and 200 mm, air velocity (v) = 12 - 28 m/s, mass flow rate (m_s) = 0.009 - 0.28 kg/s, Figure 4.40(a) showed the best validation performance at epoch 20, with an MSE of 5381.6167 after 14 epochs. Figure 4.40(c) the model achieved a training (r = 0.98288), a validation (r = 0.97898), a test (r = 0.97225), and all (r = 0.98061). Figure 4.40(b) error histogram ranged from -314.6 to 388.7, indicating slight variability but overall acceptable precision in predicting the pressure drop for this component.

4.3.4. Performance evaluation of neural network fitting model

Performance of the ANN model was evaluated through metrics: R-Square (R^2), Mean Squared Error (MSE), Mean Absolute Error (MAE), Root Mean Square Error (RMSE), Mean Absolute Percentage Error (MAPE) (%), and their relative versions (Relative MAE, Relative MSE, and Relative RMSE). These metrics assess the performance of neural network prediction accuracy, error magnitudes, and variability, which provides a comprehensive evaluation approach.

Table 4.22. Performance of the neural network for prediction

Evaluation metrics	Feeder	Horizontal pipes	Vertical pipes	90^o Bends	Cyclone separator
r	0.98568	0.98763	0.99079	0.99094	0.98601
R^2	0.97158	0.97541	0.98167	0.98196	0.97222
MSE	1840.05	7983.56	7218.22	460.0473	5381.61
MAE	29.9178	64.48	64.79	13.2658	30.5056
RMSE	39.0647	89.347	82.7	21.142	73.359
MAPE	6.3092	11.36	24.66	10.124	6.3484
Relative MAE	0.0431	0.055	0.0877	0.0825	0.0397
Relative MSE	0.0081	0.00741	0.0125	0.0173	0.0026
Relative RMSE	0.0563	0.08	0.112	0.1315	0.0508

Table 4.22 presents the regression metrics of the ANN model for the feeder, horizontal pipes, vertical pipes, 90° bends, and cyclone separator. The metrics include MSE, MAE, RMSE, MAPE, and relative errors. To interpret these results, the performance thresholds provided in Table 3.4 (Akoglu, 2018; Hange et al., 2020; Jierula et al., 2021; Uyeh et al., 2022; Chicco et al., 2021) were used.

Feeder: The ANN model for the feeder exhibits exceptional predictive accuracy in estimating pressure drop. The correlation coefficient (r = 0.98568) and the coefficient of determination (R^2 = 0.97158) indicate a very strong relationship and explain approximately 97% of the variance, consistent with an excellent model fit. The MSE of 1840.05 Pa^2, MAE of 29.92 Pa, and RMSE of 39.06 Pa demonstrate high precision and minimal error magnitude. The MAPE of 6.31% confirms strong relative accuracy and consistency, while the low relative errors (Relative MAE = 0.0431, Relative MSE = 0.0081, Relative RMSE = 0.0563) reinforce the robustness of the model predictions (Hange et al., 2020). These results suggest that the ANN can reliably guide feeder design and operational control.

Horizontal Pipes: For horizontal pipes, the ANN model demonstrates excellent performance with r = 0.98763 and R^2 = 0.97541, showing a near-perfect correlation and high explanatory power. The MSE of 7983.56 Pa^2, MAE of 64.48 Pa, and RMSE of 89.35 Pa indicate moderate absolute errors, which were acceptable given the system's complexity from Table 3.4. A MAPE of 11.36% falls in the "good accuracy" range, confirming reliable relative prediction. Relative errors (Relative MAE = 0.055, Relative MSE = 0.00741, Relative RMSE = 0.08) further demonstrate the model's effectiveness in capturing pressure drop behavior, making it suitable for horizontal pipe system design and analysis (Jierula et al., 2021).

Vertical Pipes: The ANN model for vertical pipes achieves excellent predictive performance with r = 0.99079 and R^2 = 0.98166, explaining about 98.2% of the variance in pressure drop. The MSE of 7218.22 Pa^2, MAE of 64.79 Pa, and RMSE of 82.70 Pa indicate consistent prediction quality. The MAPE of 24.66% was within the "acceptable accuracy" range in Table 3.4, reflecting expected variability due to gravity-driven flow and particle settling in vertical pipes. Relative errors (Relative MAE = 0.0877, Relative MSE = 0.0125, Relative RMSE = 0.112) confirm that the ANN can effectively predict pressure drops despite flow complexities (Jierula et al., 2021). These results highlight that vertical pipe predictions were reliable, though designers may consider slight variability in system optimization.

90° Bends: The ANN model for 90° bends shows strong predictive accuracy with r = 0.99094 and R^2 = 0.98196, capturing approximately 98.2% of the variance. Low error metrics (MSE = 460.05 Pa^2, MAE = 13.27 Pa, RMSE = 21.14 Pa) reflect precise predictions. The MAPE of 10.12% falls in the "good accuracy" range, while relative errors (Relative MAE = 0.0825, Relative MSE = 0.0173, Relative RMSE = 0.1315) indicate consistent model performance even in the complex curved flow paths of bends. This demonstrates the ANN's suitability for predicting pressure drops in bend sections.

Cyclone Separator: For the cyclone separator, the ANN exhibits strong predictive performance with r = 0.98601 and R^2 = 0.97223, explaining 97.2% of the variance. Error metrics MSE = 5381.61 Pa^2, MAE = 30.51 Pa, RMSE = 73.36 Pa reflect high precision. The MAPE of 6.35% was within the "excellent accuracy" range from Table 3.4, and relative errors (Relative MAE = 0.0397, Relative MSE = 0.0026, Relative RMSE = 0.0508) confirm the reliability of predictions. These results demonstrate that the ANN can effectively model the cyclone separator's complex flow behavior (Jierula et al., 2021).

Across all components, the ANN consistently demonstrates very high to good predictive accuracy according to Table 3.4 benchmarks. Only vertical pipes show slightly higher variability due to inherent flow dynamics, while all other components exhibit low errors and high robustness. This validates the ANN model as a reliable tool for predicting pressure drops, supporting the design, optimization, and operational control of the pneumatic conveyor system.

4.3.5. Comparative analysis between ANN model and new experimental data

In this study, a dedicated Simulink ANN simulation block was developed to predict the behavior of a pneumatic teff grain conveying system with combined CFD-DPM and experimental data. The model generated predictive results, which were then compared with a new set of experimental data not used during training, for each system component: for feeder (50), for horizontal pipes (50), for vertical pipes (50), for bends (50), and for cyclone separator (50) data were used. This approach simulated real-world deployment, where the model must handle previously unseen operating conditions. The comparison provided insights into the model's generalization ability and its effectiveness in replicating actual system performance, as presented in Table 4.24.

Table 4.23. Evaluation of ANN model performance using new experimental data

Evaluation metrics	Feeder	Horizontal pipes	Vertical pipes	90^o Bends	Cyclone separator
r	0.9802	0.98763	0.9875	0.9908	0.9863
R^2	0.9608	0.97541	0.9752	0.9792	0.9727
MSE	1220.1	1933.16	2,685.6	570.63	1264.30
MAE	34.93	43.9666	56.1	23.89	27.2231
RMSE	26.45	33.2308	35.4	14.64	35.5550
MAPE	24.63	18.01	16.64	13.632	22.38
Relative MAE	0.0244	0.0311	0.0564	0.0612	0.02342
Relative MSE	0.010	0.017	0.015	0.0674	0.093
Relative RMSE	0.0323	0.0412	0.058	0.0999	0.03059

Table 4.23 shows the ANN model's predictive performance with new experimental data. Metrics include MSE, MAE, RMSE, MAPE, and relative errors. Interpretation follows the performance benchmarks of Table 3.4 (Akoglu, 2018; Chicco et al., 2021; Jierula et al., 2021; Hange et al., 2020; Uyeh et al., 2022), allowing assessment of both absolute and proportional prediction accuracy.

Feeder: The ANN model demonstrated strong predictive capability for the feeder, with a high correlation coefficient ($r = 0.9802$) and $R^2 = 0.9608$, indicating a very strong relationship. Absolute errors ($MSE = 1220.1\ Pa^2$, $RMSE = 26.45$ Pa, $MAE = 34.93$ Pa) were low, reflecting precise predictions. The MAPE of 24.63% falls in the "acceptable accuracy" range of Table 3.4 (Jierula et al., 2021), indicating slightly reduced proportional accuracy. Relative errors (Relative MAE = 0.0244, Relative RMSE = 0.0323) confirm effective performance on a scaled basis. The slightly lower R^2 compared to other configurations suggests mild underfitting, pointing to opportunities for additional feature engineering or data refinement.

Horizontal Pipes: Horizontal pipes exhibit very strong predictive performance, with $r = 0.98763$ and $R^2 = 0.97541$, explaining about 97.5% of the variance. Absolute errors ($MSE = 1933.16\ Pa^2$, $RMSE = 33.23$ Pa, $MAE = 43.97$ Pa) were slightly higher than the feeder but remain within acceptable limits. The MAPE of 18.01% indicates good proportional accuracy, and relative errors (Relative MAE = 0.0311, Relative RMSE = 0.0412) show stable performance across the data range. This configuration demonstrates reliable and consistent predictions suitable for applications requiring balanced accuracy.

Vertical Pipes: Vertical pipes show slightly weaker performance compared to other configurations, with $r = 0.9875$ and $R^2 = 0.9752$. Absolute errors ($MSE = 2685.6\ Pa^2$, $RMSE = 35.4$ Pa, $MAE = 56.1$ Pa) were higher, likely due to outliers or complex vertical flow dynamics. MAPE = 16.64% indicates good proportional accuracy, while relative errors (Relative MAE = 0.0564, Relative RMSE = 0.058) suggest minor scaling challenges. The results indicate the ANN predicts vertical pipe pressure drops effectively but may benefit from additional preprocessing or model refinement.

90° Bends: The ANN achieves the best absolute error performance for 90° bends, with $MSE = 570.63\ Pa^2$, $RMSE = 14.64$ Pa, and $MAE = 23.89$ Pa. Correlation metrics ($r = 0.9908$, $R^2 = 0.9792$) indicate an excellent fit. MAPE = 13.63% reflects slightly higher proportional error due to small absolute pressure values, while relative RMSE = 0.0999 remains acceptable. These results highlight the ANN's high precision in predicting pressure drops through bends, ideal for applications prioritizing absolute accuracy.

Cyclone Separator: The cyclone separator shows strong proportional accuracy, with MAPE = 22.38%, and correlation metrics of r = 0.9863 and R^2 = 0.9727. Absolute errors (MSE = 1264.30 Pa^2, RMSE = 35.56 Pa, MAE = 27.22 Pa) were moderate, and relative errors (Relative MAE = 0.0234, Relative RMSE = 0.0306) were the lowest among all components, confirming excellent scaled performance. These results indicate the ANN reliably models complex cyclone flow behavior.

ANN demonstrates high predictive performance across all components, with excellent correlation and R^2 values. Absolute errors were lowest in 90° bends, while proportional accuracy was strongest in the cyclone separator. Vertical pipes exhibit higher absolute errors, reflecting inherent flow complexities. The findings confirm the ANN's suitability for both absolute and proportional predictions, supporting its use in system design, optimization, and operational control. The CFD-DPM model demonstrated excellent predictive performance for the pneumatic conveying of teff grain in a dilute-phase system.

As shown in Table 4.12, the model achieved R^2 values between 0.99096 and 0.9974 across all sections of the conveyor, including the feeder, horizontal and vertical pipes, 90° bends, and cyclone separator. The low RMSE and MAPE values indicate precise simulation of particle behavior, flow dynamics, and pressure loss throughout the system. This makes CFD-DPM particularly suitable for the detailed analysis and design optimization of pneumatic teff grain conveyors, especially when high-fidelity modeling of particle-fluid interactions was required.

ANN model with combined CFD-DPM and experimental results in Table 4.22; it also demonstrated strong predictive capability across all conveyor sections. While slightly lower in accuracy, evidenced by R^2 values ranging from 0.970 to 0.981 and moderately higher error metrics, the ANN effectively captured the general trends in particle flow and system behavior.

Furthermore, its evaluation against new experimental data in Table 4.23 revealed improved generalization, with R^2 values consistently above 0.96 and MAPE mostly below 6.5%. This suggests that the ANN model can reliably predict the performance of a pneumatic teff grain conveyor under varying operating conditions when trained with representative datasets.

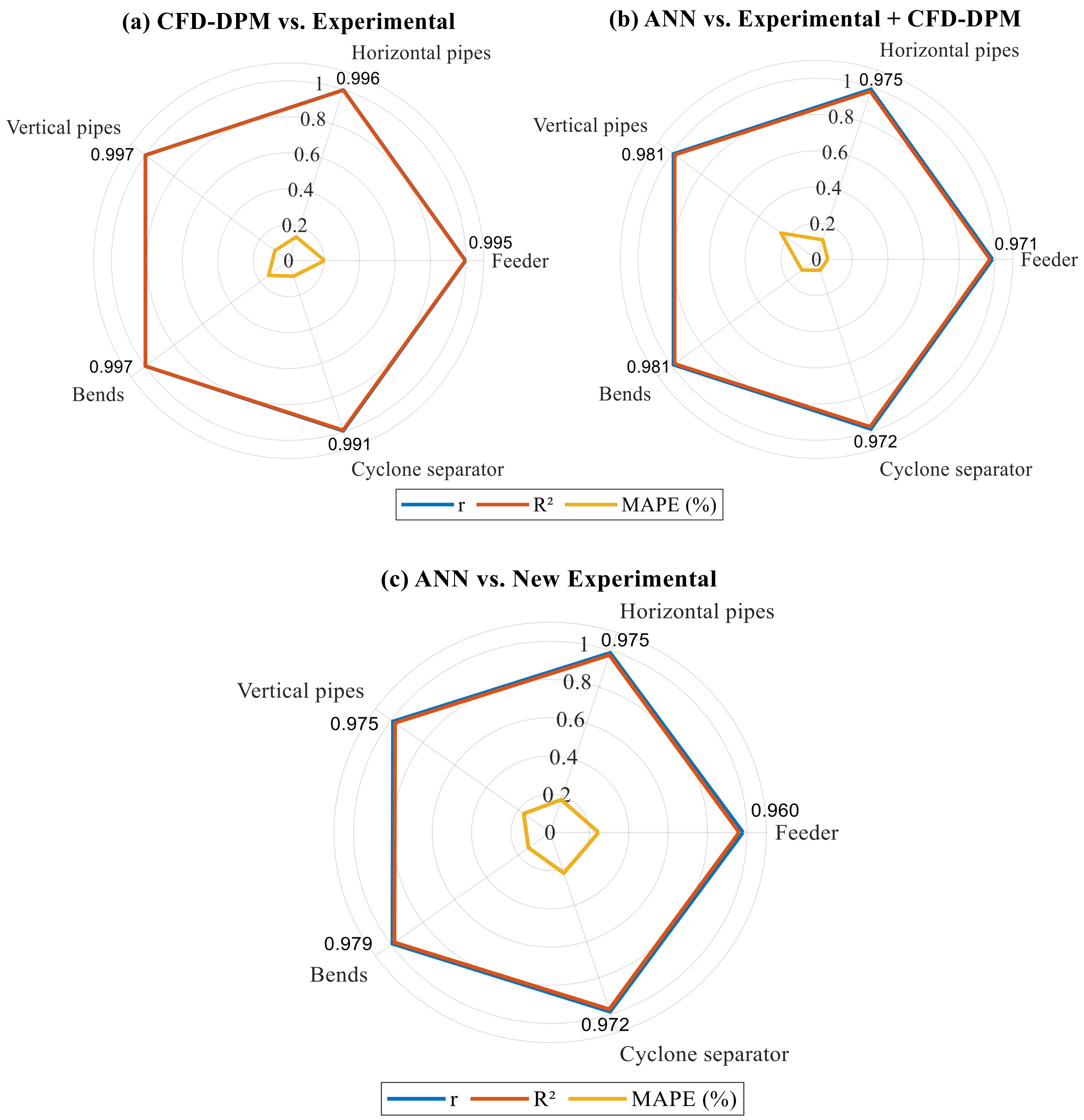

Figure 4.41. Comparison of CFD-DPM and ANN models with Experimental results

Figure 4.41(a) compares CFD-DPM simulations with experimental results. The model shows excellent agreement across all components: feeder ($r = 0.998$, $R^2 = 0.996$, MAPE = 0.203%), horizontal pipes ($r = 0.998$, $R^2 = 0.997$, MAPE = 0.139%), vertical pipes ($r = 0.999$, $R^2 = 0.997$, MAPE = 0.096%), bends ($r = 0.999$, $R^2 = 0.997$, MAPE = 0.140%), and cyclone separator ($r = 0.996$, $R^2 = 0.991$, MAPE = 0.091%). The high correlations and very low errors indicate that CFD-DPM accurately captures system behavior, confirming the model's reliability (Akoglu, 2018; Hange et al., 2020; Jierula et al., 2021).

Figure 4.41(b) presents ANN predictions against the combined dataset of experimental and CFD-DPM results. The ANN demonstrates strong performance: feeder ($r = 0.986$, $R^2 = 0.972$, MAPE = 0.063%), horizontal pipes ($r = 0.988$, $R^2 = 0.975$, MAPE = 0.114%), vertical pipes ($r = 0.991$, $R^2 = 0.982$, MAPE = 0.247%), bends ($r = 0.991$, $R^2 = 0.982$, MAPE = 0.101%), and cyclone separator ($r = 0.986$, $R^2 = 0.972$, MAPE = 0.063%). These results indicate that the ANN effectively learned from the enriched dataset, capturing underlying flow patterns with high fidelity (Chicco et al., 2021; Jierula et al., 2021).

Figure 4.41(c) shows ANN predictions compared with experimental data not included in training. Performance remains strong, though slightly lower: feeder ($r = 0.980$, $R^2 = 0.961$, MAPE = 0.246%), horizontal pipes ($r = 0.988$, $R^2 = 0.975$, MAPE = 0.180%), vertical pipes ($r = 0.988$, $R^2 = 0.975$, MAPE = 0.166%), bends ($r = 0.991$, $R^2 = 0.979$, MAPE = 0.136%), and cyclone separator ($r = 0.986$, $R^2 = 0.973$, MAPE = 0.224%). These results demonstrate good generalization to unseen data, confirming the ANN's robustness and predictive capability (Akoglu, 2018; Chicco et al., 2021).

Overall, the ANN trained on combined data effectively balances accuracy, speed, and cost. Accuracy ranking follows: experimental > CFD-DPM > ANN (combined) > ANN (new data), while efficiency ranking was reversed: ANN > CFD-DPM > experimental. This shows that the ANN provides a practical, low-cost alternative, with slightly lower precision compared to CFD-DPM but strong overall predictive capability.

5. CONCLUSIONS AND RECOMMENDATIONS

5.1. Conclusions

The study explores pneumatic conveying characteristics of teff grain with an emphasis on determining key engineering properties, designing, and constructing the system. The selection of an appropriate conveying phase, investigation of pneumatic conveying characteristics, and development of predictive models for pressure drop across key system components. Based on these findings, the following conclusions were drawn:

- Engineering properties of teff grain those were relevant to its pneumatic conveying characteristics such as particle size, density, sphericity, terminal velocity, and angle of repose were thoroughly determined and analyzed. These properties were utilized in this research for the design and modeling of the pneumatic conveying system to ensure accurate prediction of pressure drop. The findings revealed that teff grains possess a mean particle diameter ranging from 0.68-0.72 mm, particle density between 1120-1381 kg/m³, sphericity values of 0.67-0.69, terminal velocity of approximately 3.6 m/s, and an angle of repose ranging from 20.2-23.8°. When compared with other cereal grains, teff exhibited slight variations in sphericity, particle density, and angle of repose. However, the most noticeable differences were observed in particle size and terminal velocity, which play a significant role in defining the unique pneumatic conveying behavior of teff grain.

- Gas fluidization characteristic of teff grain was a critical aspect in designing efficient pneumatic conveying systems. In the Geldart classification of particles, teff is classified under Group B material, which refers to medium-sized and medium-density particles. The particles tend to have bubbly fluidization properties, and thus, it was more suitable for dilute-phase pneumatic conveying than dense-phase pneumatic conveying. The bubbly-ready nature of the teff grain in the bed tends to cause turbulence to flow in dense-phase pneumatic conveying systems, causing excessive pressure drops and also instant blockage of the system.

- Experiments revealed that the fluidized bed exhibited bubble formation at the lowest superficial gas velocity, with a pressure drop/bed height ranging from 100-107 mbar/m and a minimum fluidization velocity between 0.56 and 0.575 m/s. This early formation of bubbling in teff grain fluidization supports the conclusion that teff grain was more suitable for dilute-phase pneumatic conveying. In contrast, dense-phase pneumatic conveying leads to operational inefficiencies due to the inherent fluidizing characteristics of teff grain.

- The finding indicates that the minimum conveying velocity of teff grain, based on its saltation and superficial gas velocity, was between 4 m/s - 13.8 m/s for a solid loading ratio of 0.3 - 5 and pipe diameters of 50 mm - 110 mm. From the calculated result, superficial velocity was between 6 m/s - 20.7 m/s under the same conditions. These results indicate that teff grain requires a relatively lower airflow rate to achieve full particle suspension in a pneumatic conveyor than other cereal grains.

- The findings show that the variation in 90° bend layouts does not significantly affect the pressure drop in pneumatic conveying systems. ANOVA results revealed an F-value of 0.999 with a p-value of 0.414 for D = 46 mm and an F-value of 0.265 with a p-value of 0.899 for D = 71 mm. Since both p-values were greater than the standard significance level ($p < 0.05$), the differences in pressure drop between bend configurations were statistically insignificant. This indicates the bend layout was not a critical factor influencing pressure drops in the system.

- Combination of experimental, CFD-DPM, and ANN methods proved highly effective in modeling and analyzing the pneumatic conveying characteristics of teff grain. The CFD-DPM simulations closely matched laboratory results, with R^2 values ranging from 0.990-0.997 across major components: feeders 0.9956, horizontal pipes 0.9968, vertical pipes 0.9974, 90° bends 0.9974, and cyclone separators 0.9909. Statistical evaluation further confirmed this strong correlation, with MSE values of 27-287, RMSE of 5.2-16.9, MAE of 4.1-16.6, and MAPE between 9-20%, demonstrating the high predictive accuracy and reliability of the CFD-DPM model in replicating experimental pressure drop behavior across all components.

- ANN model also effectively predicted pressure drops across all system components, achieving R^2 values between 0.971-0.981 for feeders 0.9716, horizontal pipes 0.9754, vertical pipes 0.9817, 90° bends 0.9820, and cyclone separators 0.9722. Statistical indicators further validated this performance, with MSE ranging from 460-7984, RMSE from 21-89, MAE from 13-65, and MAPE between 6-25%. These results confirm that the ANN model, trained on both experimental and simulation data, provides strong generalization and predictive capability for pressure drop estimation in the pneumatic conveying of teff grain.

- Integrating experimental analysis with CFD-DPM simulations and ANN modeling provides a robust and comprehensive framework for understanding and predicting the flow dynamics of teff grain in pneumatic conveying systems. Validation using new experimental data also demonstrated high predictive performance, with R^2 values exceeding 0.96, MSE between 571-2686, RMSE of 14.6-35.6, MAE of 23.9-56.1, and MAPE between 13.6-24.6%. Among the models, CFD-DPM achieved slightly higher precision than ANN alone, though both showed strong consistency with experimental results, confirming their reliability for predictive applications and system optimization.

- Integrated approach offers a balanced trade-off between accuracy, computational speed, and cost-effectiveness. Experimental measurements provide the highest accuracy but were time-consuming and resource-intensive. CFD-DPM simulations deliver near-experimental precision while requiring significant computational resources. In contrast, the ANN model particularly when trained on combined experimental and CFD-DPM data offers rapid predictions at substantially lower cost. This balance makes the integrated methodology a practical and efficient tool for design optimization and performance evaluation of pneumatic conveying systems for teff grain.

5.2. Recommendations

Based on the findings of this study, several recommendations were provided to guide researchers, system designers, and professionals in the agriculture, grain handling, and food processing industries. These recommendations aim to enhance the design, efficiency, and performance of pneumatic teff grain conveying systems, reduce energy consumption, and support broader practical applications.

- Implementation of pneumatic conveying technology in the form of precision pneumatic seed drills will be recommended to address major challenges in teff planting. This technology can improve seed distribution uniformity, enhance planting efficiency, and minimize seed loss, thereby promoting uniform crop establishment and contributing to higher yield productivity.

- Adoption of pneumatic teff grain conveying systems will recommended for grain handling operations to improve bulk handling efficiency during storage and transportation. These systems can support smooth and efficient loading and unloading in warehouses, silos, and transport vehicles. Integrating a cyclone separator will also recommended to effectively extract dust, improve workplace cleanliness, enhance environmental safety, and increase overall system performance.

- Utilization of pneumatic teff grain conveying systems in the food processing industry will recommended to ensure convenient and hygienic transportation of teff grain within processing facilities. Such systems can enable continuous, contamination-free movement of materials and support operations such as conveying, feeding, cleaning, moisture and temperature regulation, blending, and packaging. Its application can play an important role in improving efficiency, product quality, and safety in modern food processing operations.

- Researchers and engineers should prioritize the unique characteristics of teff grain, such as minimum conveying air velocity and higher pressure drops across system components when compared to other cereal grains, to design and develop pneumatic conveying systems specifically tailored for dilute-phase operation. This involves optimizing airflow rates, pressure drops, and incorporating efficient separation units to ensure stable, energy-efficient, and blockage-free conveying.

- Using integrated experimental analysis with CFD-DPM simulations and ANN modeling proves essential for accurate system design, optimization, and prediction of system characteristics when it is carried out under rigorous experimental validation to ensure accuracy and reliability.

5.3. Recommendations for future researches

The finding motivates researchers and designers to carry out additional research and development to increase the application of pneumatic conveyors to teff grain handling during production, post-harvesting activities, and processing. Part of the suggested future work areas includes:

- Development of a pneumatic teff seed drill: A well-designed pneumatic system has the potential to improve seed-rate control and achieve more uniform distribution than conventional mechanical seeders. Its performance should be verified through experiments, with careful evaluation of seed placement, seed loss, lodging, and final yield, to confirm both its technical value and its practical benefits.

- Development of a multifunctional pneumatic conveying system for teff grain: Future research should explore conveying systems that integrate heating and cooling modules so that drying and cooling can occur during transport. Such a system could help control grain moisture and temperature more effectively, improving storage stability and reducing post-harvest losses. However, it will require detailed studies on energy use, effects on grain quality, and overall system reliability before it can be applied in practice.

- Development of a pneumatic teff grain cleaning system: Future work could focus on designing a dedicated pneumatic cleaning unit for teff and evaluating its ability to remove dust, foreign materials, and biological contaminants while minimizing grain damage. Experimental trials should compare cleaning efficiency, grain loss, and key quality parameters with existing cleaning technologies to determine its real performance and practical benefits.

- Development of a small-scale, fully automated pneumatic teff grain conveyor: Future studies can investigate compact, automated conveying systems designed for local teff processors. Research should emphasize precise flow control, reliable automation, safety, and cost-benefit analysis, while carefully evaluating grain loss, productivity, and maintenance requirements to judge whether such systems were practical and affordable in real operations.

- Additional studies on pneumatic teff grain conveying systems: dense-phase and negative-pressure conveyors, mechanical damage behavior, and AI-based modeling to expand operational flexibility and improve the practicality and versatility of pneumatic teff grain conveyors.

REFERENCES

Abdollahpour, S., Kosari-Moghaddam, A., & Bannayan, M. (2020). Prediction of wheat monture content at harvest time through ANN and SVR modeling techniques. Information Processing in Agriculture, 7(4), 500-510. https://doi.org/10.1016/j.inpa.2020.01.003

Abe, M. C., Gelladuga, G. A., Mendoza, C. J., Natavio, J. M., Zabala, J. S., & Lopez, E. C. R. (2023). Pneumatic conveying technology: Recent advances and future outlook. Engineering Proceedings, 56(1). https://doi.org/10.3390/ASEC2023-16267

Abebaw Tsegaye, G., & Abera, S. (2020). The study of some engineering properties of teff (Eragrostis teff (Zucc.) Trotter) grain varieties. International Journal of Food Engineering and Technology, 4(1), 9. https://doi.org/10.11648/j.ijfet.20200401.12

Abewa, A., Adgo, E., Yitaferu, B., Alemayehu, G., Assefa, K., Solomon, J. K. Q., & Payne, W. (2019). Teff grain physical and chemical quality responses to soil physicochemical properties and the environment. Agronomy, 9(6), 1-19. https://doi.org/10.3390/agronomy9060283

Adepoju, M., Verheecke-Vaessen, C., Pillai, L. R., Phillips, H., & Cervini, C. (2024). Unlocking the potential of teff for sustainable, gluten-free diets and unravelling its production challenges to address global food and nutrition security: A review. Foods, 13(21). https://doi.org/10.3390/foods13213394

Dall'Agnol, C., Marchi, C. H., & Moro, D. F. (2020, November 16-19). Iteration error estimation in computational fluid dynamics using a new empirical estimator. In Proceedings of the XLI Ibero-Latin-American Congress on Computational Methods in Engineering (Vol. 2, No. 02). Foz do Iguaçu, PR, Brazil.

Akoglu, H. (2018). User's guide to correlation coefficients. Turkish Journal of Emergency Medicine, 18(3), 91–93. https://doi.org/10.1016/j.tjem.2018.08.001

Alauddin, M., Amyotte, P., Schrader, A., Addo, A., & Kamil, M. Z. (2024). A HAZOP of dust explosion testing and explosibility modelling using artificial neural networks. Canadian Journal of Chemical Engineering, April 2024, 110-125. https://doi.org/10.1002/cjce.25358

Alemu, M. D., Ben-Zeev, S., Barak, V., Tutus, Y., Cakmak, I., & Saranga, Y. (2024). Genomic loci associated with grain protein and mineral nutrients concentrations in Eragrostis tef under contrasting water regimes. Frontiers in Plant Science, 15(December), 1–15. https://doi.org/10.3389/fpls.2024.1458408

Alizadehdakhel, A., Rahimi, M., Sanjari, J., & Alsairafi, A. A. (2009). CFD and artificial neural network modeling of two-phase flow pressure drop. International Communications in Heat and Mass Transfer, 36(8), 850-856. https://doi.org/10.1016/j.icheatmasstransfer.2009.05.005

Alwosheel, A., van Cranenburgh, S., & Chorus, C. G. (2018). Is your dataset big enough? Sample size requirements when using artificial neural networks for discrete choice analysis. Journal of Choice Modelling, 28, 167-182. https://doi.org/10.1016/j.jocm.2018.07.002

Ambrosio, L., & Crippa, G. (2014). Continuity equations and ODE flows with non-smooth velocity. Proceedings of the Royal Society of Edinburgh Section A: Mathematics, 144(6), 1191–1244. https://doi.org/10.1017/S0308210513000085

Aremu, D. O., Babajide, N. A., & Ogunlade, C. A. (2014). Comparison of some engineering properties of common cereal grains in Nigeria. International Journal of Engineering Science Invention, 3, Retrieved from http://www.ijesi.org

Atzeni, C., Lesma, G., Dubini, G., Masi, M., Rossi, F., & Bianchi, E. (2021). Computational fluid dynamic models as tools to predict aerosol distribution in tracheobronchial airways. Scientific Reports, 11(1), 1-14. https://doi.org/10.1038/s41598-020-80241-0

Awgichew, A. (2017). Performance evaluation of tef grain and chaff separation and cleaning machine. International Journal of Scientific and Research Publications, 7(7), 379–389.

Awgichew, A. (2019). Aerodynamic Properties of Tef for Separation from Chaff. Civil and Environmental Research, 11(3), 39-43. https://doi.org/10.7176/cer/11-3-05

Bako, T., & Bardey, I. A. (2020). Engineering properties of acha (Digitaria exilis) grains in relation to the design of grain processing machines. Agricultural Engineering International: CIGR Journal, 22(3), 159-170.

Barretto, R., Buenavista, R. M., Rivera, J. Lou, Wang, S., Prasad, P. V. V., & Siliveru, K. (2021). Teff (Eragrostis tef) processing, utilization and future opportunities: a review. International Journal of Food Science and Technology, 56(7), 3125-3137. https://doi.org/10.1111/ijfs.14872

Barrozo, M. A. S., Duarte, C. R., Epstein, N., Grace, J. R., & Lim, C. J. (2010). Experimental and computational fluid dynamics study of dense-phase, transition region, and dilute-phase spouting. Industrial and Engineering Chemistry Research, 49(11), 5102–5109. https://doi.org/10.1021/ie9004892

Beigzadeh, R., Rahimi, M., Jafari, O., & Alsairafi, A. A. (2016). Computational fluid dynamics assists the artificial neural network and genetic algorithm approaches for thermal and flow modeling of air-forced convection on interrupted plate fins. Numerical Heat Transfer; Part A: Applications, 70(5), 546-565. https://doi.org/10.1080/10407782.2016.1177329

Bodkhe, N., Kanekar, S. L., Bhore, T. G., & Road, K. (2015). Design, analysis, and fabrication of pneumatic material handling. International Journal of Engineering Research and Applications, 6(8), 12–23.

Bultosa, G., Abebe, W., & Lemessa, F. (2011). Grain and starch properties of six durum wheat (Triticum turgidum L. var. durum Desf) varieties grown at Debre Zeit, Ethiopia. In J. Appl. Sci. Technol (Vol. 2, Issue 1). https://www.researchgate.net/publication/264852047

Cao, L., Zhang, Q., & Meng, R. (2022). CFD–DPM Simulation Study of the Effect of Powder Layer Thickness on the SLM Spatter Behavior. Metals, 12(11). https://doi.org/10.3390/met12111897

Chan, Y., Dyah, T. M. N., & Kamaruddin, A. (2015). Solar Dryer with Pneumatic Conveyor. Energy Procedia, 65, 378-385. https://doi.org/10.1016/j.egypro.2015.01.067

Chebra, A. F., Braikia, M., Khelil, A., Bedrouni, M., & Zied, D. (2024). Numerical study of turbulent flows around a cubic obstacle blown from a variable geometry jets diffuser. Ecosistemas, 18(1). https://doi.org/10.24132/acm.2024.837

Chicco, D., Warrens, M. J., & Jurman, G. (2021). The coefficient of determination R-squared is more informative than SMAPE, MAE, MAPE, MSE and RMSE in regression analysis evaluation. PeerJ Computer Science, 7, 1-24. https://doi.org/10.7717/PEERJ-CS.623

Dagnachew, M., Moges, A., Kebede, A., & Abebe, A. (2020). Effects of Soil and Water Conservation Measures on Soil Quality Indicators: The Case of Geshy Subcatchment, Gojeb River Catchment, Ethiopia. Applied and Environmental Soil Science, 2020. https://doi.org/10.1155/2020/1868792

Daraba, D., Pop, F., & Daraba, C. (2024). Digital Twin Used in Real-Time Monitoring of Operations Performed on CNC Technological Equipment. Applied Sciences (Switzerland), 14(22). https://doi.org/10.3390/app142210088

Datta, B. K., & Ratnayaka, C. (2003). A simple technique for scaling up pneumatic conveying systems. Particulate Science and Technology, 21(3), 227–236. https://doi.org/10.1080/02726350307480

Debele, Z. A., & Buse, S. K. (2021). Modeling and laboratory measurements of pressure drop of tef (Eragrostis tef) seed bulk. Trends in Chemical Engineering, 178(19), 43–51.

Deka, R., Borthakur, P. P., Baruah, E., Sarmah, P., & Saikia, M. (2024). A comprehensive review on mechanical conveyor systems: Evolution, types, and applications. Int. J. Eng. Nat. Sci, 18, 164-183.

Dikty, M. (2025). Experimental investigation and analysis of pressure fluctuations in pneumatic conveying systems with fine bulk solids. Powder Technology, 456, 120803. https://doi.org/10.1016/j.powtec.2025.120803

Dou, J., Wang, L., Ge, W., & Ouyang, J. (2023). Effect of mesoscale structures on solid phase stress in gas–solid flows. Chemical Engineering Journal, 455(P2), 140825. https://doi.org/10.1016/j.cej.2022.140825

Dutta, P. (2019). Numerical Study on Turbulent Separation Reattachment Flow in Pipe Bends with Different Small Curvature Ratio. Journal of The Institution of Engineers (India): Series C, 100(6), 995–1004. https://doi.org/10.1007/s40032-018-0488-9

Dutta, P., Saha, S. K., Nandi, N., & Pal, N. (2016). Numerical study on flow separation in 90° pipe bend under high Reynolds number by k-ε modelling. Engineering Science and Technology, an International Journal, 19(2), 904–910. https://doi.org/10.1016/j.jestch.2015.12.005

Ebrahimi, M., Crapper, M., & Ooi, J. Y. (2014). Experimental and simulation studies of dilute horizontal pneumatic conveying. Particulate Science and Technology, 32(2), 206–213. https://doi.org/10.1080/02726351.2013.851133

El-Alfy, T. S., Ezzat, S. M., & Sleem, A. A. (2012). Chemical and biological study of the seeds of Eragrostis tef (Zucc.) Trotter. Natural Product Research, 26(7), 619-629. https://doi.org/10.1080/14786419.2010.538924

El-Behery, S. M., El-Haroun, A. A., & Abuhegazy, M. R. (2017). Prediction of pressure drop in vertical pneumatic conveyors. Journal of Applied Fluid Mechanics, 10(2). https://doi.org/10.18869/acadpub.jafm.73.239.25384

El-Emam, M. A., Zhou, L., Shi, W., Han, C., Bai, L., & Agarwal, R. (2021). Theories and Applications of CFD-DEM Coupling Approach for Granular Flow: A Review. Archives of Computational Methods in Engineering, 28(7), 4979-5020. https://doi.org/10.1007/s11831-021-09568-9

El-Kholy, M. M., & Kamel, R. M. (2021). Development and evaluation of an innovative grain cart with a pneumatic conveyor. Heliyon, 7(11). https://doi.org/10.1016/j.heliyon.2021.e08461

El ajouri, O., Lahlaouti, M. L., & Kharbouch, B. (2022). CFD-simulation of gas-solid flow in bubbling fluidized bed reactor. E3S Web of Conferences, 336. https://doi.org/10.1051/e3sconf/202233600059

Elsayed, K., & Lacor, C. (2012). Modeling and Pareto optimization of gas cyclone separator performance using RBF type artificial neural networks and genetic algorithms. Powder Technology, 217, 84–99. https://doi.org/10.1016/j.powtec.2011.10.015

Endalew, B., Elias, A., & Yasunobu, K. (2024). Impact of cluster farming on smallholder farmers teff commercialization in Ethiopia. CABI Agriculture and Bioscience, 5(1), 1–12. https://doi.org/10.1186/s43170-024-00220-7

Erken, O., Ooi, J. Y., Gupta, P., Capozzi, L., & Hanley, K. J. (2024). Parameters affecting plug characteristics in dense phase pneumatic conveying of ellipsoidal particles. Powder Technology, 437(February), 119561. https://doi.org/10.1016/j.powtec.2024.119561

Erken, O., Gupta, P., Ooi, J. Y., & Hanley, K. J. (2025). Assessment of coarse-grained CFD–DEM modelling strategies in horizontal plug-flow pneumatic conveying. Powder Technology, 461, 121015. https://doi.org/10.1016/j.powtec.2025.121015

Fernando, S. D., & Hanna, M. A. (2005). Design and Development of a Threshing Chamber and Pneumatic Conveying and Cleaning Units for Soybean Harvesting. Transactions of the ASAE, 48(1984), 1681–1688.

Fredriksson, C. (1999). Exploratory experimental and theoretical studies of cyclone gasification of wood powder, Unpublished Ph.D. thesis Submitted to Luleå University of Technology, 1–169.

Freitas, A. G. De, Borges, R., Lima, Y. O., Furlan, V., Alberto, L., & Riascos, M. (2019). Original Research Article Open Access Energy Efficiency In The Development Of An Innovative Industrial Pressurized Solids Feeder For Pneumatic Conveying Systems. 09, 27147–27152.

Fu, P., Zhu, J., Li, Q., Cheng, T., Zhang, F., Huang, Y., Ma, L., Xiu, G., & Wang, H. (2021). DPM simulation of particle revolution and high-speed self-rotation in different pre-self-rotation cyclones. Powder Technology, 394, 290–299. https://doi.org/10.1016/j.powtec.2021.08.059

Furlong, A. J., Bond, N. K., Pegg, M. J., & Hughes, R. W. (2024). Evaluation of dust and gas explosion potential in chemical looping processes. Journal of Loss Prevention in the Process Industries, 89, 105277. https://doi.org/10.1016/j.jlp.2024.105277

Gadissa, F., & Adem, M. (2025). On-farm diversity and production challenges in Ethiopian tef [Eragrostis tef ((Zuccagni) Trotter)] landraces from Arsi zone, Ethiopia: Implications for breeding and conservation. Heliyon, 11(2), e41837. https://doi.org/10.1016/j.heliyon.2025.e41837

Gandia, R. M., de Paula, W. C., de Oliveira Junior, E. A., Rodrigo, G. H., Padín, Á. R., Vegas, A. T., Gomes, F. C., & Rodríguez, P. J. A. (2022). Effect of the Hopper Angle of a Silo on the Vertical Stress at the Cylinder-to-Hopper Transition. Agronomy, 12(4). https://doi.org/10.3390/agronomy12040830

Ghafori, H., Hemmat, A., Borghaee, A. M., & Minaei, S. (2011). Physical properties and conveying characteristics of corn and barley seeds using a suction-type pneumatic conveying system. African Journal of Agricultural Research, 6(27), 5972–5977. https://doi.org/10.5897/AJAR11.1098

Ghafori, H., & Sharifi, M. (2018). Numerical and experimental study of an innovative design of elbow in the pipe line of a pneumatic conveying system. Powder Technology, 331, 171–178. https://doi.org/10.1016/j.powtec.2018.03.022

Ghode, T., Begum, K. M. M. S., Desamala, A. B., & Narayanan, A. (2017). A Comparative Study of ANN and CFD Modelling for Pressure Drop Prediction in a Fluidized Bed with Internals. Indian Chemical Engineer, 59(1), 57–75. https://doi.org/10.1080/00194506.2015.1116962

Gomes de Freitas, A., Furlan de Oliveira, V., Oliveira Lima, Y., Borges dos Santos, R., & Alberto Martinez Riascos, L. (2021). Energy efficiency in pneumatic conveying: performance analysis of an alternative blow tank. Particulate Science and Technology, 39(7), 868–876. https://doi.org/10.1080/02726351.2020.1850574

Gomes, L. M., & Mesquita, A. L. A. (2014). On the prediction of pickup and saltation velocities in pneumatic conveying. Brazilian Journal of Chemical Engineering, 31(1), 35–46. https://doi.org/10.1590/S0104-66322014000100005

Gomes, T. L. C., Lourenço, G. A., Ataíde, C. H., & Duarte, C. R. (2021). Biomass feeding in a dilute pneumatic conveying system. Powder Technology, 391, 321–333. https://doi.org/10.1016/j.powtec.2021.06.020

Gonite, T. (2018). Design and Prototyping of Teff (ጤፍ) Row Planter and Fertilizer Applier. International Journal of Mechanical Engineering and Applications, 6(4), 91.

https://doi.org/10.11648/j.ijmea.20180604.11

Govindan, V., Palaniswamy, E., Sambathkumar, M., Vijayakumar, R., & Sakthimuruga, T. M. (2014). Conveyor belt troubles (bulk material handling). International Journal of Emerging Engineering Research and Technology, 2(3), 21-30. https://www.researchgate.net/publication/341451996

Güner, M. (2007). Pneumatic conveying characteristics of some agricultural seeds. Journal of Food Engineering, 80(3), 904-913. https://doi.org/10.1016/j.jfoodeng.2006.08.010

Guzman, L., Chen, Y., & Landry, H. (2020). Coupled CFD-DEM simulation of seed flow in an air seeder distributor tube. Processes, 8(12), 1-16. https://doi.org/10.3390/pr8121597

Haghighi, A., Shadloo, M. S., Maleki, A., & Abdollahzadeh Jamalabadi, M. Y. (2020). Using committee neural network for prediction of pressure drop in two-phase microchannels. Applied Sciences (Switzerland), 10(15). https://doi.org/10.3390/APP10155384

Hange, M. I. D. E. C., Ractical, P., Ago, V. I. R., & Oa, J. (2020). The Arrowhead Agility Test:Reliability, Minimum Detectable Change, and Practical Applications In Soccer Players . Journal of Strength and Conditioning Research, 34(2), 483–494.

Hashemisohi, A., Wang, L., & Shahbazi, A. (2019). Dense discrete phase model coupled with kinetic theory of granular flow to improve predictions of bubbling fluidized bed hydrodynamics. KONA Powder and Particle Journal, 36(36), 215-223. https://doi.org/10.14356/kona.2019017

He, X. (2021). ANN Model Using Gradient Descent to Train Weight Vectors. 2021 IEEE 3rd International Conference on Communications, Information System and Computer Engineering, CISCE 2021, Cisce, 574–577. https://doi.org/10.1109/CISCE52179.2021.9445953

Hein, K., Girma, D., & Mckay, J. (2025). Genetic diversity and environmental adaptation in Ethiopian tef. G3: Genes, Genomes, Genetics, 5(October 2024), 1–15. https://doi.org/10.1093/g3journal/jkae303

Helali, M., Ahmad, S., Abdollahpour, S., & Navid, H. (2023). Self-propelled chickpea harvester for small holding area. 25(3), 95–108.

Huang, F., Zhu, Q., Zhou, X., Gou, D., Yu, J., Li, R., Tong, Z., & Yang, R. (2021). Role of CFD based in silico modelling in establishing an in vitro-in vivo correlation of aerosol deposition in the respiratory tract. In Advanced Drug Delivery Reviews (Vol. 170). https://doi.org/10.1016/j.addr.2020.09.007

Jardon, E. L., Tlatelpa-Becerro, A., Rico-Martínez, R., Calderón-Ramírez, M., Reynoso-Jardón, E., Tlatelpa-Becerro, A., Rico-Martínez, R., Calderón-Ramírez, M., & Urquiza, G. (2019). Artificial Neural Networks (ANN) to Predict Overall Heat Transfer Coefficient and Pressure Drop on a Simulated Heat Exchanger. In International Journal of Applied Engineering Research (Vol. 14). http://www.ripublication.com

Jierula, A., Wang, S., Oh, T. M., & Wang, P. (2021). Study on accuracy metrics for evaluating the predictions of damage locations in deep piles using artificial neural networks with acoustic emission data. Applied Sciences (Switzerland), 11(5), 1–21. https://doi.org/10.3390/app11052314

Journal, A. I., Roberts, J., Wypych, P., Hastie, D., Liao, R., Roberts, J., Wypych, P., & Hastie, D. (2021). Analysis and validation of a CFD-DPM method for simulating dust suppression sprays. Particulate Science and Technology, 0(0), 1–12. https://doi.org/10.1080/02726351.2021.1951907

Kalman, H., Satran, A., Meir, D., & Rabinovich, E. (2005). Pickup (critical) velocity of particles. Powder Technology, 160(2), 103–113. https://doi.org/10.1016/j.powtec.2005.08.009

Karimi, M., Kheiralipour, K., Tabatabaeefar, A., Khoubakht, G. M., Naderi, M., & Heidarbeigi, K. (2009). The effect of moisture content on physical properties of wheat. Pakistan Journal of Nutrition, 8(1), 90–95. https://doi.org/10.3923/pjn.2009.90.95

Kaur, B., Mittal, A., Mallick, S. S., Pan, R., & Jana, S. (2017). Numerical simulation of fluidized dense-phase pneumatic conveying of powders to develop improved model for solids friction factor. Particuology, 35, 42–50. https://doi.org/10.1016/j.partic.2016.11.006

Kaur, B., Mittal, A., Wypych, P., Mallick, S. S., & Jana, S. (2017). On developing improved modelling and scale-up procedures for pneumatic conveying of fine powders. Powder Technology, 305, 270–278. https://doi.org/10.1016/j.powtec.2016.09.080

Khoshtaghaza, M. H., & Mehdizadeh, R. (2006). Aerodynamic Properties of Wheat Kernel and Straw Materials. Agricultural Engineering International: The CIGR Ejournal, VIII(January 2006), 1–10.

Kiliçkan, A., & Güner, M. (2010). The determination of pneumatic conveying characteristics of chickpea. Turkish Journal of Agriculture and Forestry, 34(4), 265–

274. https://doi.org/10.3906/tar-0905-32

Klavins, L., Kviesis, J., Steinberga, I., Klavina, L., & Klavins, M. (2016). Gas chromatography–mass spectrometry study of lipids in northern berries. Agronomy Research, 14 (S2), 1328–1346. https://doi.org/10.15159/AR.16.057

Klinzing, G. E., Rizk, F., Marcus, R., & Leung, L. S. (2011). Pneumatic conveying of solids: A theoretical and practical approach (2nd ed., Vol. 8). Springer Science & Business Media. https://doi.org/10.1007/978-94-011-6328-5

Kong, H. (2022). CFD-DEM simulation of the effect of superficial gas velocity on particle motion in a novel gas-solid non catalytic fluidized bed (NRFB). The Lancent Pschch, 1-35.

Kuang, S., Zhou, M., & Yu, A. (2020). CFD-DEM modelling and simulation of pneumatic conveying: A review. Powder Technology, 365, 186-207. https://doi.org/10.1016/j.powtec.2019.02.011

Lashkarbolooki, M., Vaferi, B., & Mowla, D. (2012). Using Artificial Neural Network to Predict the Pressure Drop in a Rotating Packed Bed. Separation Science and Technology (Philadelphia), 47(16), 2450-2459. https://doi.org/10.1080/01496395.2012.665975

Leema, N., Nehemiah, K. H., Christo, E. V. R., & Kannan, A. (2020). Evaluation of Parameter Settings for Training Neural Networks Using Backpropagation Algorithms: A Study With Clinical Datasets. International Journal of Operations Research and Information Systems, 11(4), 62–85. https://doi.org/10.4018/IJORIS.2020100104

Lenaerts, B., Aertsen, T., Tijskens, E., & De Baerdemaeker, J. (2013). Simulation of grain–straw separation by discrete element modeling with bendable straw particles. Computers and Electronics in Agriculture, 98, 222-235. https://doi.org/10.1016/j.compag.2013.08.011

Li, K., Kou, J., & Zhang, W. (2022). Deep Learning for Multifidelity Aerodynamic Distribution Modeling from Experimental and Simulation Data. AIAA Journal, 60(7), 4413–4427. https://doi.org/10.2514/1.J061330

Li, Z., Nie, Z., & Li, G. (2024). Integrating Crop Modeling and Machine Learning for the Improved Prediction of Dryland Wheat Yield. Agronomy, 14(4). https://doi.org/10.3390/agronomy14040777

Lia, Z., Liu, G., Guo, N., & Liu, F. (2016). Study on the Motion state of Powdery materials in Dense-phase Pneumatic Conveying Pipe. MATEC Web of Conferences, 65, 2–5. https://doi.org/10.1051/matecconf/20166503005

Liu, X., Su, C., Li, Z., Wang, K., Xie, F., Tian, Y., & Qi, J. (2024). Analysis and

Evaluation of Seed-Filling Performance of a Pneumatic Interference Precision Seeder for Small Cabbages. Applied Sciences (Switzerland), 14(7). https://doi.org/10.3390/app14072825

Liu, Y., Zhang, J., Yang, S., Li, J., & Liu, Q. (2024). Prospective on applying machine learning in computational fluid dynamics (CFD) simulation of metallurgical reactors. Ironmaking & Steelmaking: Processes, Products and Applications, 51(9), 1085–1098. https://doi.org/10.1177/03019233241278460

Mezhericher, M., Brosh, T., & Levy, A. (2011). Modeling of particle pneumatic conveying using DEM and DPM methods. Particulate Science and Technology, 29(2), 197–208. https://doi.org/10.1080/02726351003792914

Minten, B., Engida, E., & Tamru, S. (2016). How big are post-harvest losses in Ethiopia? Evidence from teff (ESSP II Working Paper 93). International Food Policy Research Institute & Ethiopian Development Research Institute. https://hdl.handle.net/10568/147758

Mohapatra, D., Saha, K. P., & Bhushana Babu, V. (2019). Disinfestation of Chickpea and Green Gram from Callosobruchus maculatus Adults Through Hot-Air-Assisted Microwave Heating System. Agricultural Research, 8(1), 72–83. https://doi.org/10.1007/s40003-018-0346-2

Molenda, M., & Stasiak, M. (2001). Determination of the elastic constants of cereal grains in a uniaxial compression test. International Agrophysics, 16(1), 61–65.

Montilla, C., Ansart, R., Majji, A., Nadir, R., Cid, E., Simoncini, D., & Negny, S. (2024). On Using CFD and Experimental Data to Train an Artificial Neural Network to Reconstruct ECVT Images: Application for Fluidized Bed Reactors. Processes, 12(2). https://doi.org/10.3390/pr12020386

Negash, W., Menzir, A., & Kassaye, M. (2017). Effect of Row Spacing on Yield and Yield Components of Teff [Eragrostis tef (Zucc.) Trotter] Varieties in Gonji Kolela District, North Western Ethiopia. Journal of Biology, Agriculture and Healthcare, 7(23), 35-43. www.iiste.org

Osman, E. A., Ayoub, M. A., & Aggour, M. A. (2005). Artificial neural network model for predicting bottomhole flowing pressure in vertical multiphase flow. SPE Middle East Oil and Gas Show and Conference, MEOS, Proceedings, 1187-1197. https://doi.org/10.2523/93632-ms

Özlü, R. R., & Güner, M. (2022). Determination of Pneumatic Conveying Characteristics of Canola Seeds. Tarim Bilimleri Dergisi, 28(4), 656-665.

https://doi.org/10.15832/ankutbd.794097

Pan, R., & Wypych, P. W. (1992). Scale-up procedures for pneumatic conveying design. Powder Handling & Processing, 4A survey(2), 167–172.

Paber, C., Tecnocereal, T. T., & Tanase, T. (2016). Energy Efficiency of Vacuum Pneumatic Conveying in Flour Milling – Limit. November, 0-9.

Park, D., & Go, J. S. (2020). Design of cyclone separator critical diameter model based on machine learning and cfd. Processes, 8(11), 1–13. https://doi.org/10.3390/pr8111521

Rajabipour, A., Tabatabaeefar, A., & Farahani, M. (2006). Effect of Moisture on Terminal Velocity of Wheat Varieties. International Journal of Agriculture & Biology, 8(1), 10–13.

Rakhimov, K., Melikuziyev, S., & Sultanov, R. (2023). Coefficient of hydraulic friction of plastic pipes. E3S Web of Conferences, 401, 0-4. https://doi.org/10.1051/e3sconf/202340101042

Reed, G. F., Lynn, F., & Meade, B. D. (2002). Use of coefficient of variation in assessing variability of quantitative assays. Clinical and Diagnostic Laboratory Immunology, 9(6), 1235–1239. https://doi.org/10.1128/CDLI.9.6.1235-1239.2002

Remy, B., Khinast, J. G., & Glasser, B. J. (2009). Discrete element simulation of free flowing grains in a four-bladed mixer. AIChE Journal, 55(8), 2035–2048. https://doi.org/10.1002/aic.11876

Roberts, J., Wypych, P., Hastie, D., & Liao, R. (2022). Analysis and validation of a CFD-DPM method for simulating dust suppression sprays. Particulate Science and Technology, 40(4), 415–426. https://doi.org/10.1080/02726351.2021.1951907

Roseberg, R., Norberg, S., & Charlton, B. (2018). Teff Grass for Forage: Nitrogen and irrigation requirements. June, 1-10. https://catalog.extension.oregonstate.edu/pnw709/html

Sabar, S. S., Swain, S. K., Behera, D., Rayaguru, K., Mohapatra, A. K., & Dash, A. K. (2020). Moisture Dependent Physical and Engineering Properties of Sorghum Grains. International Journal of Current Microbiology and Applied Sciences, 9(8), 2365–2375. https://doi.org/10.20546/ijcmas.2020.908.271

Sadik, J. A., Demelash, B., & Gizaw, M. (2013). Hydration kinetics of teff grain. Journal of Agricultural Engineering and Food Technology, 15(1). http://www.cigrjournal.org

Salim, S. M., & Cheah, S. C. (2009). Wall y+ Strategy for Dealing with Wall-bounded Turbulent Flows. International MultiConference of Engineers and Computer Scientists (IMECS), II(January 2009), 1–6.

Sarkis, A. M., & Energia, D. (2025). Mathematical modeling and numerical simulation of iron ore drying in a pneumatic conveyor Modelagem matemática e simulação numérica da secagem de minério de ferro em transportador pneumático Modelado matemático y simulación numérica del secado de mineral . 1-33. https://doi.org/10.55905/oelv23n1-147

Shadloo, M. S., Rahmat, A., Karimipour, A., & Wongwises, S. (2020). Estimation of pressure drop of two-phase flow in horizontal long pipes using artificial neural networks. Journal of Energy Resources Technology, Transactions of the ASME, 142(11). https://doi.org/10.1115/1.4047593

Shahbazi, F., Valizadeh, S., & Dowlatshah, A. (2014). Aerodynamic properties of Makhobeli, triticale and wheat seeds. International Agrophysics, 28(3), 389-394. https://doi.org/10.2478/intag-2014-0029

Sharma, A., & Mallick, S. S. (2021). An investigation into pressure drop through bends in pneumatic conveying systems. Particulate Science and Technology, 39(2), 180-191. https://doi.org/10.1080/02726351.2019.1676348

Shijo, J. S., & Behera, N. (2021). Performance prediction of pneumatic conveying of powders using artificial neural network method. Powder Technology, 388, 149-157. https://doi.org/10.1016/j.powtec.2021.04.071

Shijo, J. S., & Behera, N. (2023). Pressure Drop Prediction in Fluidized Dense Phase Pneumatic Conveying using Machine Learning Algorithms. Journal of Applied Fluid Mechanics, 16(10), 1951–1961. https://doi.org/10.47176/jafm.16.10.1869

Singh, J., Gill, H. S., & Vasudev, H. (2023). Computational fluid dynamics analysis on role of particulate shape and size in erosion of pipe bends. International Journal on Interactive Design and Manufacturing, 17(5), 2631–2646. https://doi.org/10.1007/s12008-022-01094-7

Sonawane, S., Jagtap, P., & Meena, S. (2022). Investigations on physical properties of maize in context of mechanical shelling and dehusking. The Pharma Innovation Journal, 11(12), 5440–5443. http://www.icar.org.in/files/Vision-2050-ICAR.pdf.

Spedding, P. L., Benard, E., & McNally, G. M. (2004). Fluid flow through 90 degree bends. Developments in Chemical Engineering and Mineral Processing, 12(1-2), 107-128.

Sternberg, R. J., & Sternberg, K. (2016). Literature Research. The Psychologist's Companion, 5(2), 49–64. https://doi.org/10.1017/cbo9781316488935.005

Suppan, T., Neumayer, M., Bretterklieber, T., Wegleiter, H., & Puttinger, S. (2021).

Performance Assessment Framework for Electrical Capacitance Tomography Based Mass Concentration Estimation in Pneumatic Conveying Systems. Conference Record - IEEE Instrumentation and Measurement Technology Conference, 2021-May(May). https://doi.org/10.1109/I2MTC50364.2021.9459986

Tadele, E., & Hibistu, T. (2021). Empirical review on the use dynamics and economics of teff in Ethiopia. In Agriculture and Food Security (Vol. 10, Issue 1). BioMed Central Ltd. https://doi.org/10.1186/s40066-021-00329-2

Tadele, E., & Hibistu, T. (2022). Spatial production distribution, economic viability and value chain features of teff in Ethiopia: Systematic review. Cogent Economics and Finance, 10(1). https://doi.org/10.1080/23322039.2021.2020484

Tadić, S., Krstić, M., Božić, M., Dabić-Miletić, S., & Zečević, S. (2024). Ranking of Technologies for Intralogistic Bulk Material Handling Processes Using Fuzzy Step-Wise Weight Assessment Ratio Analysis and Axial-Distance-Based Aggregated Measurement Methods. Applied Sciences (Switzerland), 14(4). https://doi.org/10.3390/app14041549

Tang, L., Sunden, B., & Wang, Q. (2016). Numerical analysis of heat transfer in complex fluid systems. HT2008-56241, 1–9.

Tavakoli, M., Tavakoli, H., Rajabipour, A., Ahmadi, H., & Gharib-Zahedi, S. M. T. (2009). Moisture-dependent physical properties of barley grains. International Journal of Agricultural and Biological Engineering, 2(4), 84–91. https://doi.org/10.3965/j.issn.1934-6344.2009.04.084-091

Tb, S., Il, P., & Hn, R. (2019). Engineering properties of sorghum. ~ 108 ~ International Journal of Chemical Studies, 7(5), 108–110.

Tiguh, E. E., Delele, M. A., Ali, A. N., Kidanemariam, G., & Fenta, S. W. (2024). Assessment of harvest and postharvest losses of teff (Eragrostistef (Zucc.)) and methods of loss reduction: A review. Heliyon, 10(9), e30398. https://doi.org/10.1016/j.heliyon.2024.e30398

Tsegaye, G. A., & Abera, S. (2020). The study of some engineering properties of teff [Eragrostis teff (Zucc.) Trotter] grain varieties. International Journal of Food Engineering and Technology, 4(1), 9.

Tura, D. C., Belachew, T., Tamiru, D., & Abate, K. H. (2024). Effects of blending ratio variation on macronutrient compositions and sensory acceptability of dabi teff-field pea-based novel composite complementary flours. Food Science and Nutrition, 12(4), 2408–2425. https://doi.org/10.1002/fsn3.3925

Uyeh, D. D., Iyiola, O., Mallipeddi, R., Asem-Hiablie, S., Amaizu, M., Ha, Y., & Park, T. (2022). Grid Search for Lowest Root Mean Squared Error in Predicting Optimal Sensor Location in Protected Cultivation Systems. Frontiers in Plant Science, 13(July), 1–17. https://doi.org/10.3389/fpls.2022.920284

Vasundhara, C., Rajender, G., Teja, R., Mamatha, P., & Sunil, K. (2019). Development and evaluation of terminal velocity apparatus for sorghum grains. Journal of Pharmacognosy and Phytochemistry, 8(3), 2–8.

Verma, V., & Padding, J. T. (2020). A novel approach to MP-PIC: Continuum particle model for dense particle flows in fluidized beds. Chemical Engineering Science: X, 6, 100053. https://doi.org/10.1016/j.cesx.2019.100053

Vinuesa, R., Brunton, S. L., & McKeon, B. J. (2023). The transformative potential of machine learning for experiments in fluid mechanics. Nature Reviews Physics, 5(9), 536–545. https://doi.org/10.1038/s42254-023-00622-y

Wang, C., Li, W., Li, B., Jia, Z., Jiao, S., & Ma, H. (2023). applied sciences Study on the Influence of Different Factors on Pneumatic Conveying in Horizontal Pipe.

Wan, J., Wang, H., Liu, B., Yang, X., Hu, X., Cai, S., He, G., & Liu, Y. (2025). TrajectoryFlowNet: Lagrangian-Eulerian learning of flow field and trajectories. arXiv preprint. Retrieved from https://arxiv.org/abs/2507.09621

Wheeldon, J. M., Baeyens, J., Li, S., & Deng, Y. (2022). A new design approach for the established flow region of vertical, dilute-phase pneumatic conveyors. Particuology, 66, 10–20. https://doi.org/10.1016/j.partic.2021.06.013

Xu, F., & Scholar, G. (2023). Recent Advancement in Pneumatic Conveying for Application in Feed Industry : A Review. https://doi.org/10.20944/preprints202310.1376.v1

Yang, D., Li, G., Wang, Y., Wang, Q., Li, J., Huang, Q., Xia, Y., & Li, Q. (2020). Prediction of Horizontal Pneumatic Conveying of Large Coal Particles Using Discrete Phase Model. Advances in Materials Science and Engineering, 2020. https://doi.org/10.1155/2020/1967052

Yang, H., Li, X., Jin, Q., Jing, D., & Ma, L. (2024). Prediction of sand particle trajectories and erosion distribution in offshore oil and gas pipelines. Computational Particle Mechanics, 11(5), 1923–1936. https://doi.org/10.1007/s40571-024-00718-x

Yehuda, T., & Kalman, H. (2020). Geldart classification for wet particles. Powder Technology, 362, 288–300. https://doi.org/10.1016/j.powtec.2019.11.073

Yigezu Wendimu, G. (2021). The challenges and prospects of Ethiopian agriculture. Cogent Food and Agriculture, 7(1), 1-26. https://doi.org/10.1080/23311932.2021.1923619

Zahedi, P., Parvandeh, S., Asgharpour, A., McLaury, B. S., Shirazi, S. A., & McKinney, B. A. (2018). Random forest regression prediction of solid particle Erosion in elbows. Powder Technology, 338, 983–992. https://doi.org/10.1016/j.powtec.2018.07.055

Zeleke, W. A. (2015). Tef as an industrial crop for food processing. Exploring its latent potential and flour-handling characteristics. 206.

Zewdu, A. D. (2007). Aerodynamic properties of tef grain and straw material. Biosystems Engineering, 98(3), 304–309. https://doi.org/10.1016/j.biosystemseng.2007.08.003

Zewdu, A. D., & Solomon, W. K. (2007). Moisture-Dependent Physical Properties of Tef Seed. Biosystems Engineering, 96(1), 57-63. https://doi.org/10.1016/j.biosystemseng.2006.09.008

Zhao, B., & Su, Y. (2010). Artificial neural network-based modeling of pressure drop coefficient for cyclone separators. Chemical Engineering Research and Design, 88(5–6), 606–613. https://doi.org/10.1016/j.cherd.2009.11.010

Zhao, H., Huang, Y., Liu, Z., Liu, W., & Zheng, Z. (2021). Applications of Discrete Element Method in the Research of Agricultural Machinery : A Review.

Zhao, Z., Guo, Z., Feng, J., & Qian, Z. (2024). Effect of mesh size on particle tracking with correction for submerged jet impingement. Powder Technology, 431(November). https://doi.org/10.1016/j.powtec.2023.119080

Zhou, H., Wang, G., Jia, C., & Li, C. (2019). A novel, coupled CFD-DEM model for the flow characteristics of particles inside a pipe. Water (Switzerland), 11(11). https://doi.org/10.3390/w11112381

Zubrilina, E., Vysochkina, L., Danilov, M., & Maliyev, V. (2017). Design modification of seed distributor of pneumatic seeder for corn sowing. Engineering for Rural Development, 16, 772–778. https://doi.org/10.22616/ERDev2017.16.N158

RESEARCH OUTPUTS FROM THIS DISSERTATION

The following sections of the dissertation have been published and currently under review in peer-reviewed journals.

Published Journal Papers

1. Boset, L. D., Debele, Z. A., & Koroso, A. W. (2024). Pressure drop due to cyclone separator in positive dilute phase pneumatic teff grain conveyor. Journal of Applied Fluid Mechanics, 18(2), 317–331. https://doi.org/10.47176/jafm.18.2.2964

2. Demissie Boset, L. D., Debele, Z. A., & Koroso, A. W. (2025). Experimental investigation of minimum fluidization velocity and pressure drop in fluidized bed of teff grain. Journal of Heat and Mass Transfer Research, 12(2), 323–333. https://doi.org/10.22075/jhmtr.2025.35810.1632

3. Demissie Boset, L., Wako, A., & Zewdie, B. (2023). Determination of terminal velocity of some agricultural grains using Ansys Rocky DEM-CFD coupling simulation. Science Development, 4(2), 28–35. https://doi.org/10.11648/j.scidev.20230402.12

4. Boset, L. D., Debele, Z. A., & Koroso, A. W. (2025). Determination of pressure drop in positive dilute phase pneumatic teff grain conveyor using experimental CFD-DPM simulation and ANN modeling approach. International Journal of Fluid Power, 26(3), 343–380. https://doi.org/10.13052/ijfp1439-9776.2631

5. Lemi Demissie, Zewdu Abdi, Amana Wako “CFD-DPM Analysis of Velocity and Pressure Distribution for Selected Agricultural Cereal Grains for Straight Pipe in Pneumatic Conveyor “ Under Review”

APPENDICES

APPENDIX A. LABORATORY SETUP

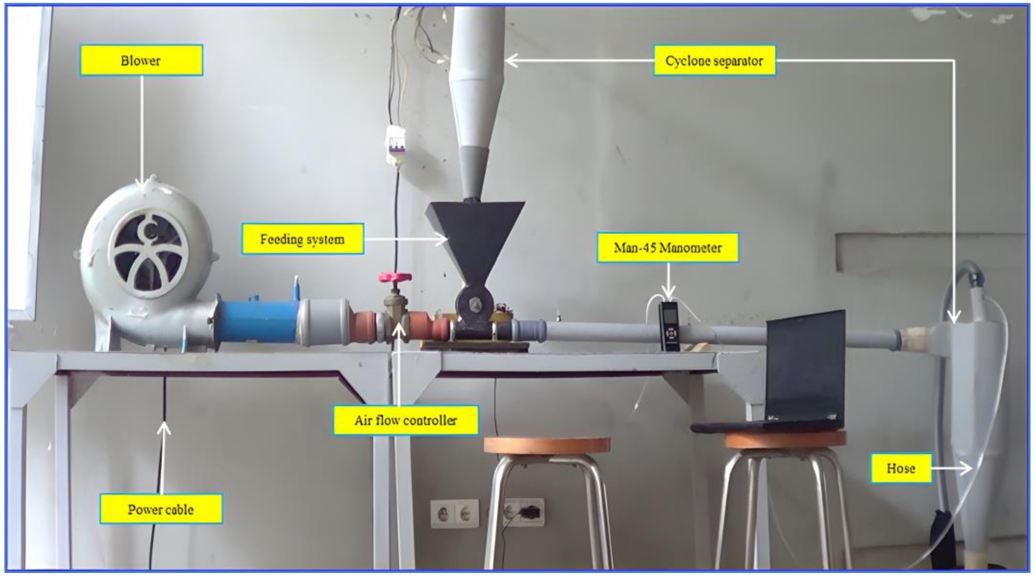

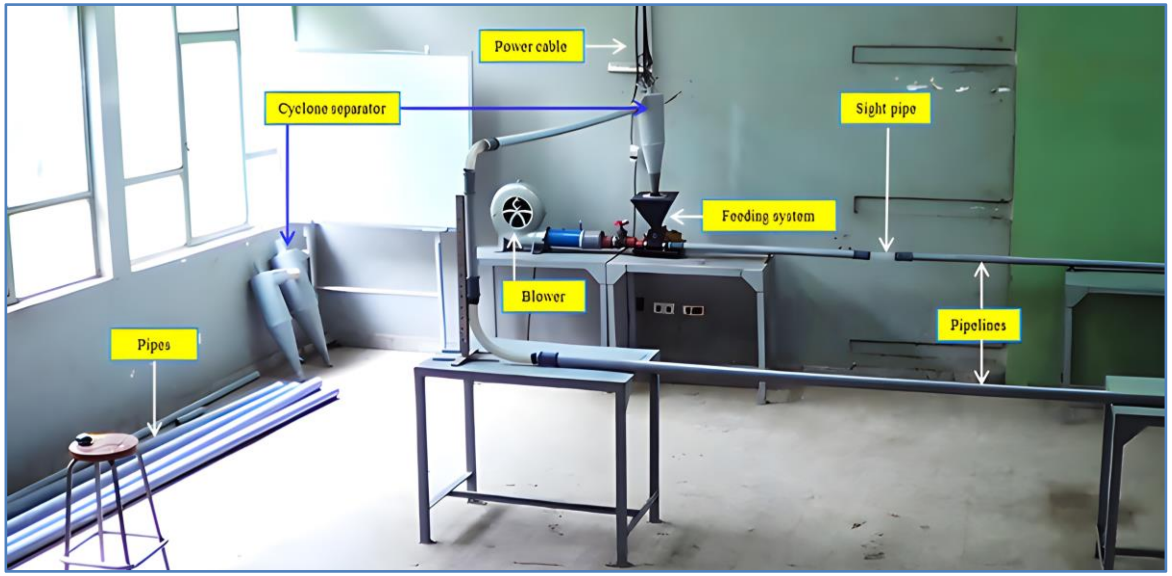

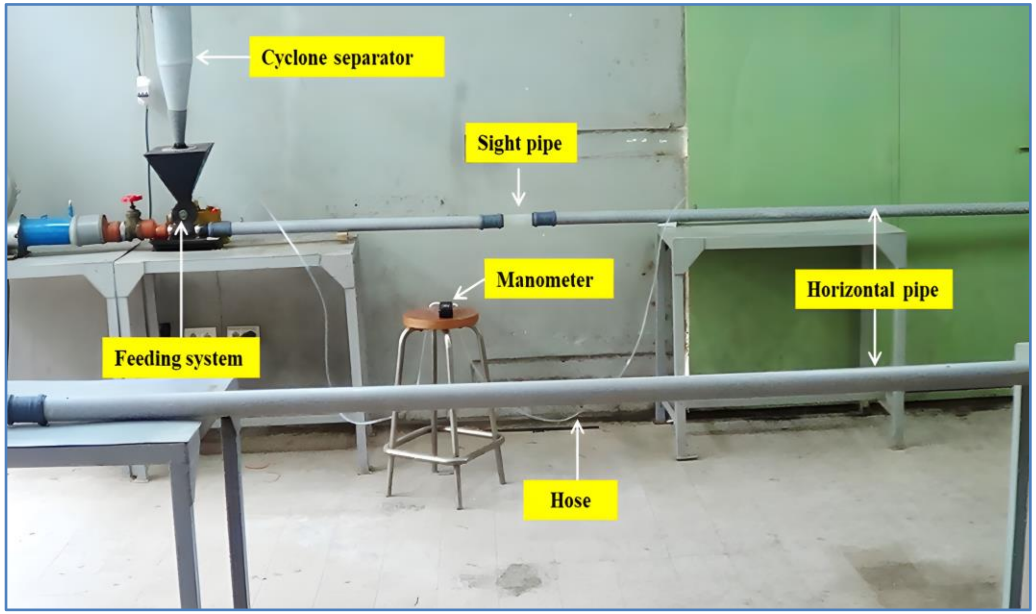

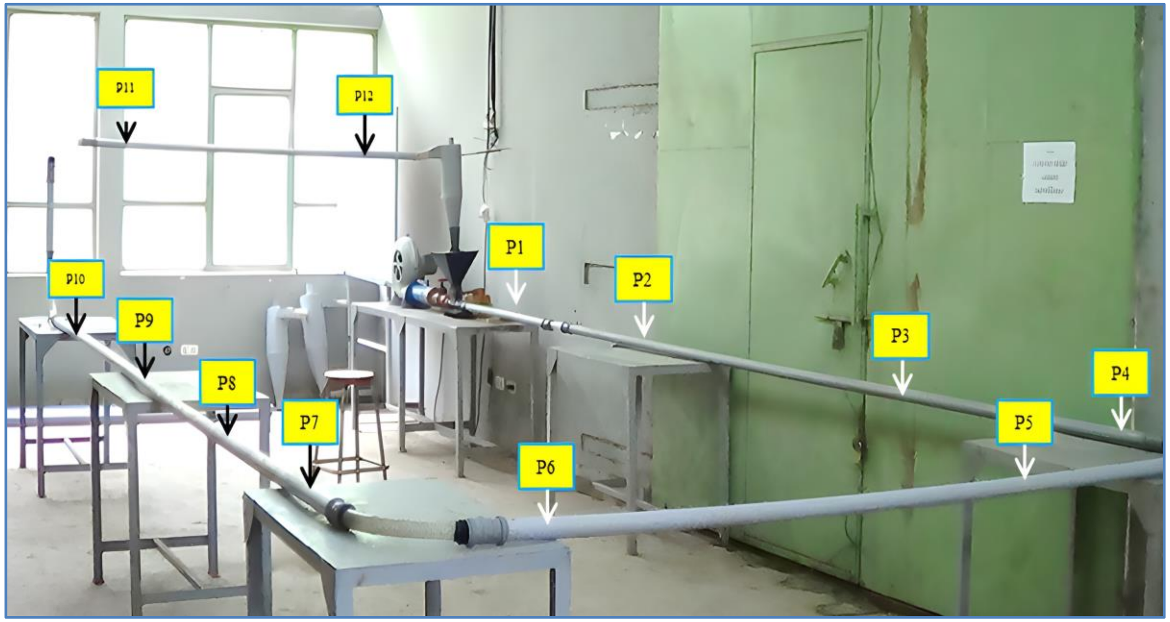

APPENDIX B. CFD-DPM MODEL FOR FULL SYSTEM [v = 22m/s and m_s = 0.13kg/s]

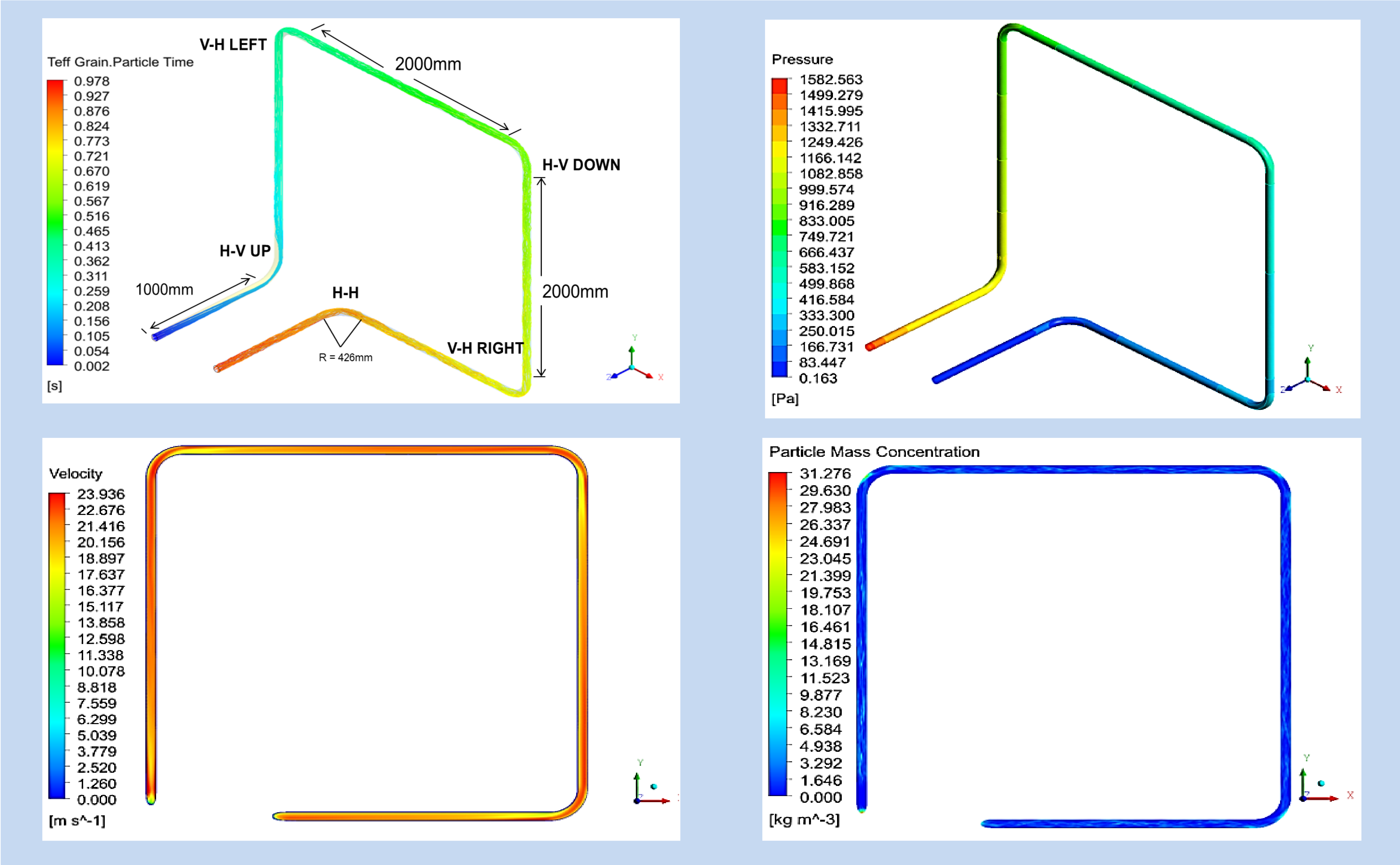

APPENDIX B. CFD-DPM MODEL FOR FULL SYSTEM [v = $22m/s$ and m_s = $0.13kg/s$]

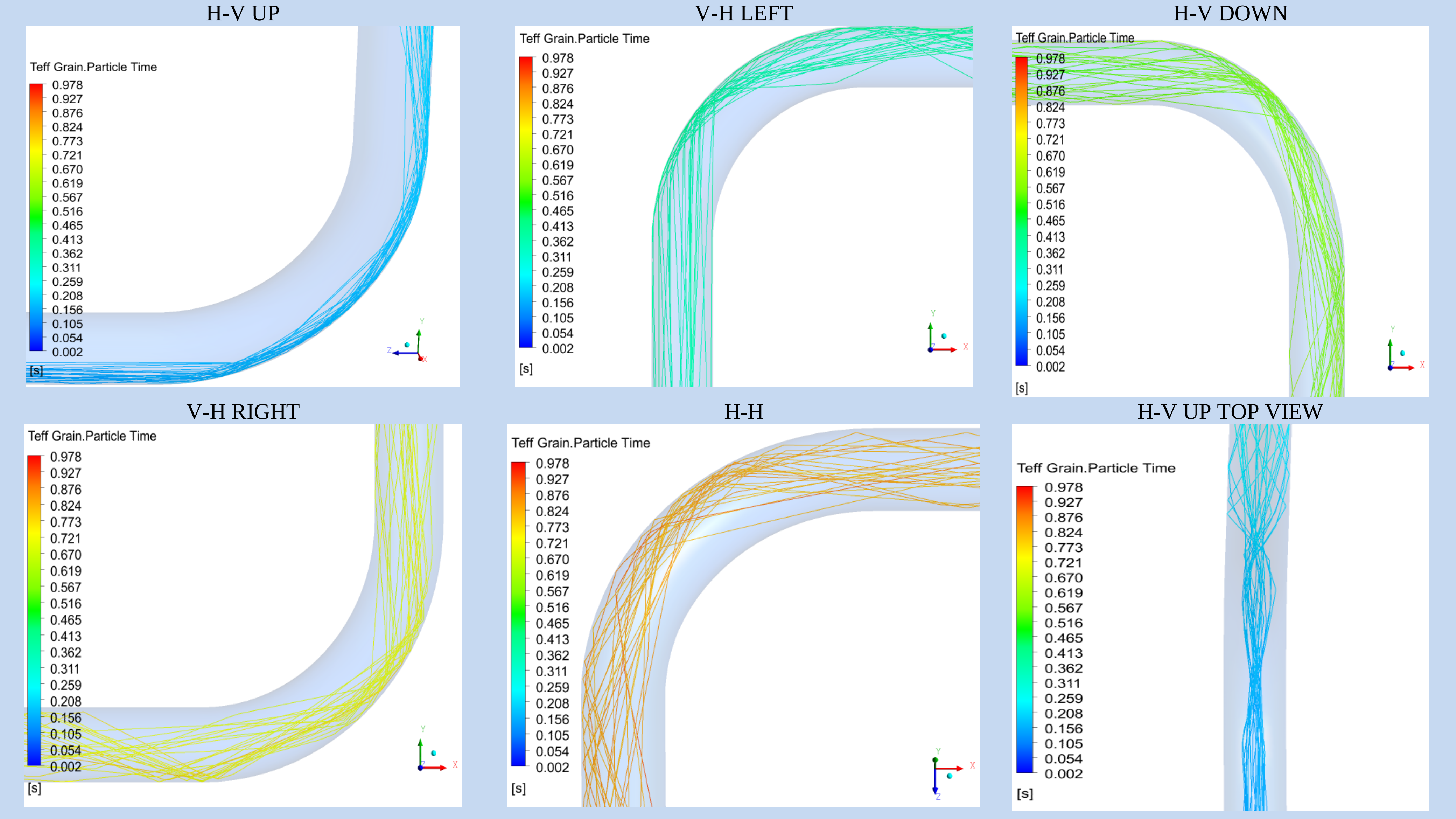

APPENDIX B. CFD-DPM MODEL FOR FULL SYSTEM [$v = 22m/s$ *and* $m_s = 0.13kg/s$]

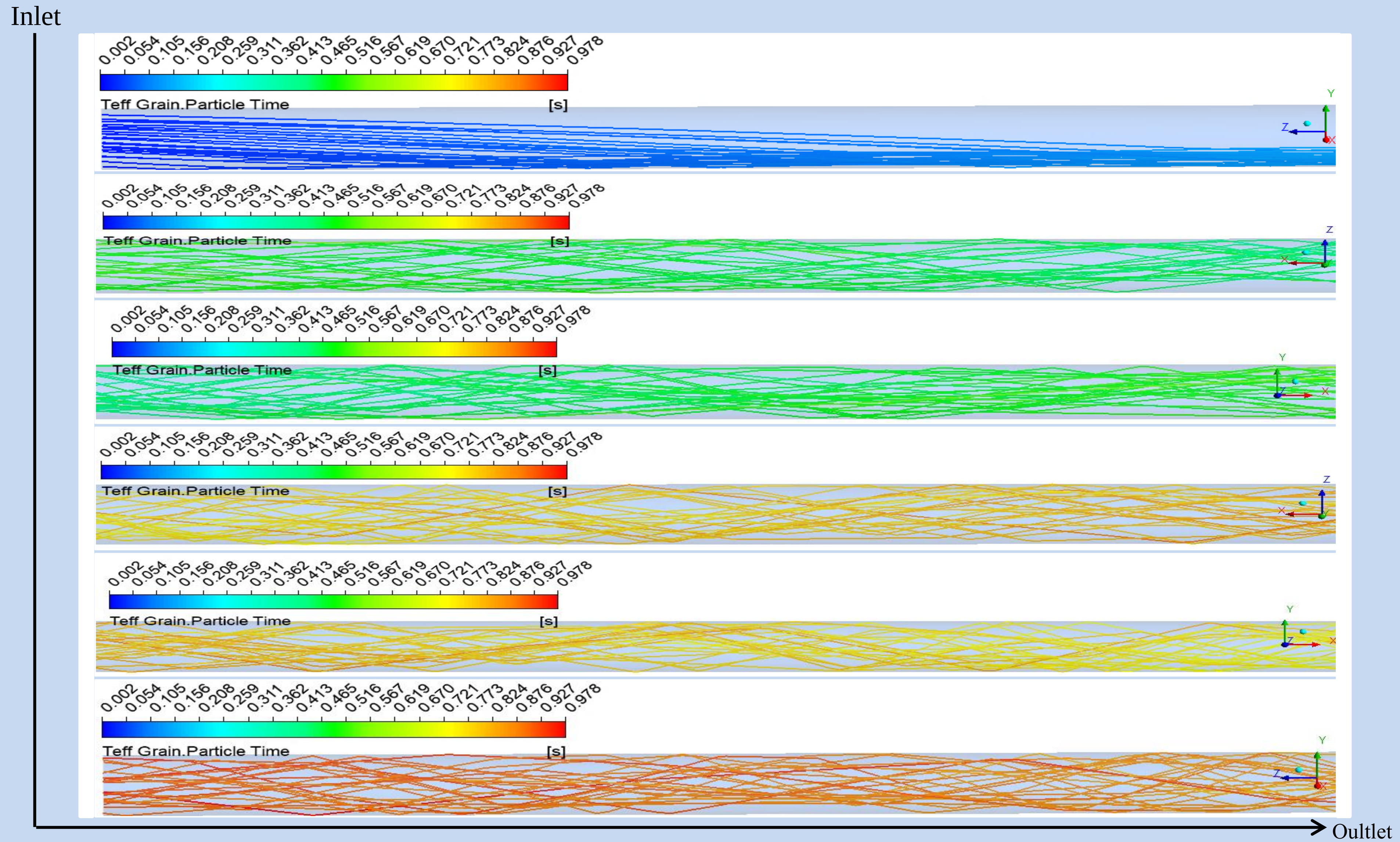

APPENDIX C. ANOVA TABLE FOR SIGNIFICANCE LEVEL FOR AIR VELOCITY, MATERIAL FLOW RATE, PIPE DIAMETER, AND PIPE LENGTH ON FEEDER PRESSURE DROP (Pa)

ANOVA table for feeder pressure drop (Pa)

Source	Sum of Squares (SS)	Degrees of Freedom (df)	Mean Square (MS)	F-Value	p-value	Significance
Air Velocity (v)	3,250,421.2	6	541,736.9	1024.5	< 0.0001	***** (Most Significant)
Material Flow Rate (m_s)	1,890,356.8	8	236,294.6	446.8	< 0.0001	****
Diameter (D)	85,123.4	1	85,123.4	160.9	< 0.0001	**
Interaction Effects	42,567.1	14	3,040.5	5.75	< 0.0001	(Minor)
Error (Residuals)	25,432.1	48	529.8	–	–	–
Total	5,293,900.6	77	–	–	–	–

ANOVA table for horizontal pipe pressure drop (Pa)

Source	Sum of Squares (SS)	Degrees of Freedom (df)	Mean Square (MS)	F-Value	p-value	Significance
Air Velocity (v)	8,750,632.1	6	1,458,438.7	2450.3	< 0.0001	***** (Most Significant)
Material Flow Rate (m_s)	5,220,189.4	8	652,523.7	1096.1	< 0.0001	****
Diameter (D)	1,120,456.2	1	1,120,456.2	1882.4	< 0.0001	***
Interaction Effects	980,321.5	2	490,160.8	823.5	< 0.0001	**
Error (Residuals)	320,567.8	48	6,678.5	11.2	< 0.0001	(Minor)
Total	85,432.1	144	593.3	–	–	–
Air Velocity (v)	16,477,599.1	209	–	–	–	–

(c)ANOVA table for vertical pipe pressure drop (Pa)

Source	Sum of Squares (SS)	Degrees of Freedom (df)	Mean Square (MS)	F-Value	p-value	Significance
Air Velocity (v)	12,450,632.1	6	2,075,105.4	3450.3	< 0.0001	***** (Most Significant)
Material Flow Rate (m_s)	7,220,189.4	8	902,523.7	1500.1	< 0.0001	****
Diameter (D)	2,120,456.2	1	2,120,456.2	3524.4	< 0.0001	***
Interaction Effects	1,480,321.5	2	740,160.8	1230.5	< 0.0001	**
Error (Residuals)	420,567.8	48	8,761.4	14.6	< 0.0001	(Minor)
Total	185,432.1	308	601.4	–	–	–

APPENDIX D. NONLINEAR REGRESSION MODEL

(a) Nonlinear Regression Model

Component	General Form of Model	Coefficients to Fit	Final Model Equation
Feeder	$\Delta P = k \cdot D^a \cdot v^b \cdot m_s{}^c$	*k=0.5, a=−1.2, b=1.8, c=0.9*	$\Delta P = 0.5 \cdot D^{-1.2} \cdot v^{1.8} \cdot m_s{}^{0.9}$
Horizontal pipe	$\Delta P = k \cdot D^a \cdot L^b \cdot v^c \cdot m_s{}^d$	*k=0.12, a=−1.8, b=0.9,c =1.7, d=0.8*	$\Delta P = 0.12 \cdot D^{-1.8} \cdot L^{0.9} \cdot v^{1.7} \cdot m_s{}^{0.8}$
Vertical pipe	$\Delta P = k \cdot D^a \cdot L^b \cdot v^c \cdot m_s{}^d$	*k=0.183,a=−1.92, b=0.9,c=1.85, d=0.82*	$\Delta P = 0.183 \cdot D^{-1.92} \cdot L^{0.95} \cdot v^{1.85} \cdot m_s{}^{0.82}$
90^o Bends	$\Delta P = k \cdot D^a \cdot v^b \cdot m_s{}^c$	*k=0.218, a=−1.88, b=1.82, c=0.79*	$\Delta P = 0.218 \cdot D^{-1.88} \cdot v^{1.82} \cdot m_s{}^{0.79}$
Cyclone separator	$\Delta P = k \cdot D^a \cdot v^b \cdot m_s{}^c$	*k=0.959, a=−0.795, b=2.036, c=0.305*	$\Delta P = 0.959 \cdot D^{-0.795} \cdot v^{2.036} \cdot m_s{}^{0.305}$

(b) Model Evaluation Metrics

Evaluation metrics	Feeder	Horizontal Pipe	Vertical pipe	Bend	Cyclone separator
R-Square (R^2)	0.9123	0.915	0.872	0.784	0.901370
Mean Squared Error (MSE)	28943.9443	100,902.24	1,245,678	2,145,678	6754.7656
Mean Absolute Error (MAE)	134.1469	250.12	842.3	1,142.3	55.7295
Root Mean Square Error (RMSE)	170.0942	317.65	1,116	1,465	82.1874
Mean Absolute Percentage Error (MAPE) (%)	12.2786	25.37	38.7	52.7	8.5241
Relative MAE	7.9159	26.47	44.8	63.9	7.2634
Relative MSE	2.0692	11.31	19.5	24.8	1.1474
Relative RMSE	1.1808	33.63	59.3	81.9	10.7117

APPENDIX E. PRESSURE DROP COEFFICIENT (K)

Predictive model of pressure drop coefficient (K) vs. square of inlet air velocity (v^2_{entry}) for (a) feeder, (b) horizontal pipeline (c) vertical pipeline (d) bends and (e) cyclone separator